Slow-wave coupled lines integrated over silicon in mm-wave band - Applications to couplers, filters and baluns

Jose Lugo Alvarez

UNIVERSITÉ GRENOBLE ALPES

THÈSE

Pour obtenir le grade de

DOCTEUR DE L'UNIVERSITÉ GRENOBLE ALPES

Spécialité : **Optique et Radio-fréquence**

Arrêté ministériel : 7 août 2006

Présentée par

« Jose LUGO ALVAREZ»

Thèse dirigée par **« Philippe FERRARI»** et
Co-encadrée par **« Florence PODEVIN »**

préparée au sein du **Laboratoire IMEP-LAHC**
dans **l'École Doctorale Electronique, Electrotechnique, Automatique et Traitement du Signal**

Lignes couplées à ondes lentes intégrées sur silicium en bande millimétrique – Application aux coupleurs, filtres et baluns

Thèse soutenue publiquement le **« 7 décembre 2015»**,
devant le jury composé de :

M. Sylvain BOURDEL
Professeur des universités, Grenoble, Président
Mme. Odile PICON
Professeur Emérite, Paris-Est Marne-la-Vallée, Rapporteur
M. Jean-Baptiste BEGUERET
Professeur des universités, Bordeaux, Rapporteur
Mme. Anne-Laure, FRANC
Maître de conférences, Toulouse, Membre
M. Didier VINCENT
Professeur des universités, Saint Etienne, Membre
M. Jean-Michel FOURNIER
Professeur Emérite, Grenoble, Membre
M. Philippe FERRARI
Professeur des universités, Grenoble, Directeur de thèse
Mme. Florence PODEVIN
Maître de conférences, Grenoble, Co-encadrant de thèse

Index

Introduction

The need of high-data-rate systems to answer the demand for big data exchanges, the demands of high-resolution radars and imaging systems for medicine and security, push the electronics systems to millimeter-wave (mm-wave) frequency bands. In that context, advanced CMOS-BiCMOS technologies are the preferred technologies to develop the future systems. They offer relative low-cost, as compared to AsGa technologies, and high performance, with transistors f_{max} – f_t higher than 300 GHz. However, while active circuits offer great performance, the development of passive circuits remains an issue. Beyond say 60 to 100 GHz, lumped circuits, like baluns, couplers, power dividers, etc, based on inductances and transformers, suffer from increased design complexity, due to parasitics that can no more be neglected. Hence, distributed circuits become a better option than the traditional lumped approaches, especially for applications as coupling, power division, balun, etc. But their size, even at mm-wave, remains an issue. Considering a given electrical length, the physical length of a transmission line is proportional to the working frequency. However, the guided wavelength for microstrip lines in CMOS-BiCMOS technologies is still around 1.5 mm at 100 GHz, leading to 750 µm long quarter-wave length transmission lines. This is still very big as compared to nanoscale transistors. Moreover, whereas the length of the transmission lines decreases with frequency, this is not the case for their width. A 50-Ω characteristic impedance transmission line has almost the same width at 1 GHz and 100 GHz. And last but not least, the electrical performance of classical microstrip lines, mainly used in CMOS-BiCMOS technologies at mm-waves, are really poor in terms of losses, and tend to deteriorate the performances of the overall system composed of active and passive devices. As a consequence, efforts should be carried out towards the development of high-performance miniaturized passive circuits.

Within this context, a new kind of transmission line called Slow-wave CPW (S-CPW), was proposed in 2003 by John Long[1]. Subsequently, several developments were carried out concerning S-CPWs. The first equivalent electrical model was proposed in 2013 by Anne-Laure Franc[2]. The calculus of the elements of the model was recently developed by Alfredo Bautista in 2015[3], opening the way to much easier implementations of the S-CPWs. Where days were necessary to simulate and optimize S-CPWs by using 3D EM tools, it only takes a few minutes now! S-CPW provides a significant longitudinal miniaturization (a factor of 2 or 3 compared to

1. J. R. Long, “On-chip interconnect for mm-wave aaplications using an all-copper technology and wavelength reduction,,” in *IEEE Int. Solid-State Circuits Conf.*, San Francisco, 2003.
2. Franc, A.; Pistono, E.; Meunier, G.; Gloria, D.; Ferrari, P., "A Lossy Circuit Model Based on Physical Interpretation for Integrated Shielded Slow-Wave CMOS Coplanar Waveguide Structures," IEEE Trans. Microw. Theory Techn., vol .61, no. 2, pp.754-763, Feb. 2013.
3. Bautista, A.; Franc A.-L.; Ferrari, P.; “An Accurate Parametric Electrical Model for Slow-wave CPW,” in *Int. Microw. Symp.,* Phoenix, USA, 2015.

the microstrip lines), it presents a high quality factor (40 at 60 GHz, which is twice the value of a microstrip line) and lastly it is highly compatible with the CMOS back-end-of-line (BEOL) process. The width of S-CPW is twice that of a microstrip line, leading to comparable footprints in practical designs, but their highest electrical performances make these transmission lines very good candidates for the development of the future elite passive circuits for mm-wave integrated systems. A good designer has to deal with both microstrip lines and S-CPWs, in order to build the more performing system.

All the mm-wave systems use passive circuits, the simplest ones being perhaps matching networks for LNAs or PAs. Among the wide family of passive circuits, directional couplers are a key element in many systems, since they are used for sensing or dividing purposes. Directional couplers are four-ports circuits. The energy from input port is flowing to two output ports with equal or unequal power division, and a phase shift between the output signals (90° in the classical case of a quarter-wave length coupler). One output port is called the coupled port. The fourth port is the isolated port. Depending of the energy travelling direction, the coupled and isolated ports are exchanged. This is the main characteristic of directional couplers, i.e. their ability to distinguish the direction of the travelling wave. This characteristic is given by the directivity of the coupler, which represents a metric of “how good is the coupler ?”. This device is therefore very useful for applications such as signal sampling, monitoring, feedback, combining, separating, receiving or beam forming.

Two families of directional couplers are available, the coupled-line and the hybrid coupler. In this thesis, the work was focused on the development of coupled-line couplers.

The technique used today to implement coupled-lines at mm-wave in advanced technologies is the microstrip structure. This structure provides good performances in terms of losses, and microstrip line topology seems thus to be a good solution to implement this type of passive circuit. However, numerous improvements should be done to this structure since it presents also many issues such as the inhomogeneity of the medium, which prevents the circuit to present high directivity or the difficulty to achieve tight coupling due to the limitations in the dimensions generally imposed by the fabrication process (design rules). Broadside coupled-lines were proposed to overcome the tight coupling problem; however it still presents poor directivity characteristic.

In this thesis, an alternative approach for mm-wave coupled-lines is proposed. It overcomes all the microstrip lines couplers limitations, and offers the possibility to design compact coupled-lines with an extra degree of freedom, leading to simpler design process. The concept is based on the novel coupled-slow-wave coplanar waveguide (CS-CPW) proposed in

this thesis. The modification on the floating electromagnetic shielding layer leads to great design flexibility. Cutting some floating ribbons can be used to modify coupling in order to provide equal magnetic and electric coupling coefficients. Similarly, even- and odd-modes characteristic impedances can be modified independently. Based on this characteristic, several passive devices were designed. Besides, the slow-wave behavior leaded to more compact devices as compared to their microstrip counterparts. The BiCMOS 55 nm technology from ST Microelectronics was considered for all the designs carried out in this thesis. However, the developed concepts can be applied to any CMOS-BiCMOS technologies without lack of generality.

In the **first chapter**, a presentation of the theory for directional couplers is made. Then the traditional topologies for planar couplers are presented. One of the topologies is especially interesting because it can be integrated in advanced CMOS technologies and can achieve strong coupling. For this reason, the state-of-art of broadside coupled-line couplers compatible with CMOS is detailed. Finally the main objectives of this thesis are introduced.

The **second chapter** is dedicated to the presentation and fully detailed explanation of the novel structure, the CS-CPW. First the traditional theory of coupled-microstrip line is presented. Next, the CS-CPW concept, electrical model as well as its extraction method from 3D EM simulations is featured. Thanks to 3D EM simulations, charts with the evolution of the electrical parameters are realized and they are compared to the coupled-microstrip solution. Later, the concept of cutting the floating electromagnetic shielding in the CS-CPW is presented and its effect over the (magnetic and electric) coupling is studied. At the end of this chapter, practical issues linked to the layout of CS-CPWs are discussed.

Based on the developments carried out in the second chapter, a method to design directional couplers is developed in the **third chapter**. The general concept where the electric coupling k_C can be controlled without perturbing the magnetic coupling k_L is explained. Thanks to this method, couplers with $k_C = k_L$ can be implemented, leading to high-directivity devices. Directional couplers designed with CS-CPWs are compared to their microstrip counterparts. Two directional couplers are realized in BiCMOS 55 nm technology as a proof-of-concept. One of them was experimentally characterized, and the results as well as its practical issues are presented. The second coupler has yet to be characterized. Finally, as directional couplers are 4-port circuits, a multimode TRL method was also implemented in order to de-embed the measurements.

Next, parallel coupled-lines filters are studied in the **fourth chapter**. A review of this kind of filters is briefly made; this highlights the significance of the characteristic impedances to design resonators and filters. Using the analytical model presented in the second chapter, charts

giving the evolution even- and odd-modes characteristic impedance Z_c^{even} and Z_c^{odd}, are presented. Next, as a proof-of-concept, two CS-CPW-based devices were designed at 80 GHz: a resonator and a filter.

Finally the **fifth chapter** presents very promising prospects for the use of this novel coupled-lines topology in the advanced technologies or for original applications. Three circuits are presented in this chapter. The first study is a reflection-type phase shifter. In this circuit the hybrid coupler is replaced by a CS-CPW-based coupler. The second device developed is an isolator at 77 GHz. The last circuit is a Marchand balun. For each one of the circuits an overview is made as well as a review of the state-of-art. Then the performances of the directional coupler designed for the specific application are presented and at the end the simulation results of the resulting systems using the CS-CPW-based coupler is also shown.

Chapter 1

Directional Couplers in Millimeter-Waves: Presentation

Among distributed passive circuits that are developed at millimeter waves (mm-wave), couplers take an important role. Applications as varied as filters, matched phase-shifters or high directivity couplers for in-situ measurement systems are targeted. In particular, to save place on a die, integrated coupled lines couplers are most interesting as compared to their counterparts, i.e. in phase, out-of-phase or 90° couplers such as power divider, rat-race or hybrid. Integrated coupled lines (CL) couplers are becoming mandatory for the development of future in-situ measurement systems, especially when working at frequencies beyond 100 GHz. In such case load-pull measurements are limited by the insertion loss of the cables that connect the wafer probes with the external tuner [1], thus there is a strong need for high directivity and low coupling couplers. 3-dB CL couplers could also replace hybrid ones used in reflection type phase shifters, leading to more compact circuits. In addition new topologies of transformers could be designed, as proposed in [2].

In this chapter, it is first reminded the general theory of directional, and the conventional theory for coupled lines couplers to later present a brief overview of the existing solutions in terms of couplers as well as some recent applications. Among the solutions for couplers, we will have special interest in the broadside coupled lines because it is the currently used structure in order to provide tight coupling in CMOS advanced technologies. Therefore a state-of-the-art of

this special structure is done in section 1.3 where many topologies are explained and compared. Finally, we address the approach proposed in this thesis: slow-wave effect as an alternative option to implement high performances coupled transmission lines with the possibility to reach any desired coupling.

1.1. Classical directional couplers theory

1.1.1. General definitions for a 4-port symmetrical, reciprocal directional coupler

A directional coupler is a 4-port network as presented in Figure 1-1. This figure is the specific example of coupled lines; however, it can be extended to any horizontally and vertically symmetrical 4-port networks. This leads to the general coupler ports and parameters definition. The considered structure is thus symmetrical in the AA' and BB' planes. Besides, all ports are assumed to be terminated by the same load Z_0.

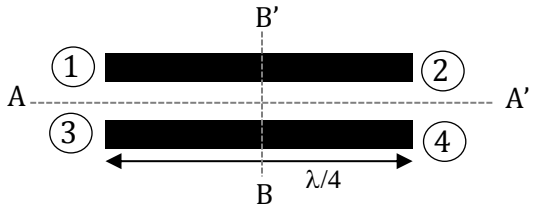

Figure 1-1: Coupled lines directional coupler ports definition.

The scattering matrix of a 4-port network is given by:

$$[S] = \begin{bmatrix} S_{11} & S_{12} & S_{13} & S_{14} \\ S_{21} & S_{22} & S_{23} & S_{24} \\ S_{31} & S_{32} & S_{33} & S_{34} \\ S_{41} & S_{42} & S_{43} & S_{44} \end{bmatrix} \quad (1\text{-}1)$$

Because of the symmetrical and reciprocal nature of the structure, the scattering matrix can be expressed as:

$$[S] = \begin{bmatrix} S_{11} & S_{21} & S_{31} & S_{41} \\ S_{21} & S_{11} & S_{41} & S_{31} \\ S_{31} & S_{41} & S_{11} & S_{21} \\ S_{41} & S_{31} & S_{21} & S_{11} \end{bmatrix} \quad (1\text{-}2)$$

A directional coupler is described by the following factors:

- Return loss.
- Through/Direct (T).
- Coupling (C).
- Isolation (I).

- Directivity (D).

These are expressed from equations (1-3) to (1-6).

$$Through = T = 10\log\frac{P_1}{P_2} = -20\log|S_{21}| \tag{1-3}$$

$$Coupling = C = 10\log\frac{P_1}{P_3} = -20\log|S_{31}| = 10\log k^2 \tag{1-4}$$

$$Isolation = I = 10\log\frac{P_1}{P_4} = -20\log|S_{41}| \tag{1-5}$$

$$Directivity = D = 10\log\frac{P_3}{P_4} = -20\log\frac{|S_{31}|}{|S_{41}|} = I - C \tag{1-6}$$

where P_1 is the input power at port 1. P_2, P_3 and P_4 are the output power at ports 3 and 4, respectively. k is the coupling coefficient. In the ideal case, no output power flows through the isolated port (Port 4); however in practice there is a small power that is flowing out from this port. A very good directional coupler is a 4-port device where a desired amount of power is coupled while keeping a high directivity; which is equivalent to have a very high isolation for a desired coupling.

In this thesis, the directional coupler is studied in its backward-wave configuration for the coupled port with the nomenclature of Figure 1-1. The ideal coupler matched at all ports, with infinite isolation (equivalent to an infinite directivity) presents thus the following matrix:

$$[S] = \begin{bmatrix} 0 & S_{21} & S_{31} & 0 \\ S_{21} & 0 & 0 & S_{31} \\ S_{31} & 0 & 0 & S_{21} \\ 0 & S_{31} & S_{21} & 0 \end{bmatrix} \tag{1-7}$$

As the considered coupler is symmetrical, theoretically, it can be studied with an even-odd-modes approach with the symmetrical and reciprocal even- and odd matrices expressed as:

$$[S]^{even} = \begin{bmatrix} S_{11}^e & S_{21}^e \\ S_{21}^e & S_{11}^e \end{bmatrix} \tag{1-8}$$

$$[S]^{odd} = \begin{bmatrix} S_{11}^o & S_{21}^o \\ S_{21}^o & S_{11}^o \end{bmatrix} \tag{1-9}$$

Consequently, the coupler S-parameters can be defined from the even- and odd-ones.

$$S_{11} = \frac{S_{11}^e + S_{11}^o}{2} \tag{1-10}$$

$$S_{21} = \frac{S_{21}^e + S_{21}^o}{2} \tag{1-11}$$

$$S_{31} = \frac{S_{11}^e - S_{11}^o}{2} \tag{1-12}$$

$$S_{41} = \frac{S_{21}^e - S_{21}^o}{2} \tag{1-13}$$

Having a fully matched, completely isolated coupler thus relies on the two assumptions presented in [3]:

$$S_{11o} = -S_{11e} \tag{1-14}$$

$$S_{21o} = S_{21e} \tag{1-15}$$

1.1.2. Coupled lines directional coupler

A section of coupled lines of length l carefully designed may act as a matched directional coupler. Considering a symmetrical coupled lines structure, its modal reduction is presented in Figure 1-2.

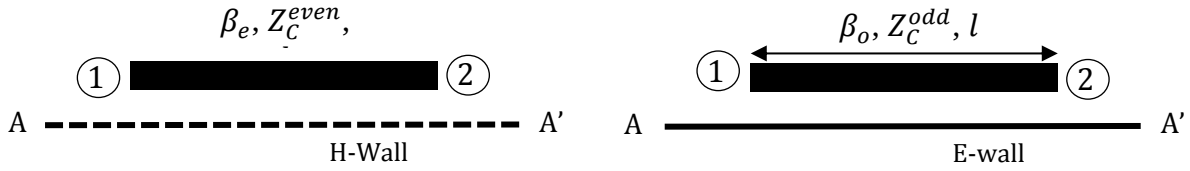

(a) (b)

Figure 1-2: Reduced symmetrical coupled lines structure (a) even-mode and (b) odd-mode.

ABCD matrices are given for even- and odd-modes in eq. (1-16) and (1-17), respectively.

$$\begin{bmatrix} A_e & B_e \\ C_e & D_e \end{bmatrix} = \begin{bmatrix} \cos\beta_e l & jZ_C^{even}\sin\beta_e l \\ \dfrac{j\sin\beta_e l}{Z_C^{even}} & \cos\beta_e l \end{bmatrix} \tag{1-16}$$

$$\begin{bmatrix} A_o & B_o \\ C_o & D_o \end{bmatrix} = \begin{bmatrix} \cos\beta_o l & jZ_C^{odd}\sin\beta_o l \\ \dfrac{j\sin\beta_o l}{Z_C^{odd}} & \cos\beta_o l \end{bmatrix} \tag{1-17}$$

From (1-16)and (1-17), the even- and odd-mode characteristic impedances as well as the propagation constant can be computed:

$$Z_C^{even/odd} = \sqrt{\frac{B_{e/o}}{C_{e/o}}} \tag{1-18}$$

$$\gamma^{even/odd} = \frac{\operatorname{arccosh}(A_{e/o})}{l} \tag{1-19}$$

To be matched and isolated, the coupled lines coupler must satisfy both equations (1-14) and (1-15). These conditions are achieved when:

$$Z_C^{odd} Z_C^{even} = Z_0^2 \tag{1-20}$$

$$\beta_e = \beta_o = \beta \tag{1-21}$$

This is also equivalent to have similar phase velocities for both even- and odd-modes, leading to:

$$S_{21} = \frac{\sqrt{1-k^2}}{\sqrt{1-k^2}\cos\theta + j\sin\theta} \tag{1-22}$$

$$S_{31} = \frac{jk\sin\theta}{\sqrt{1-k^2}\cos\theta + j\sin\theta} \tag{1-23}$$

$\theta = \beta l$ is the electrical length of the coupler and k, as already told, the coupling coefficient defined as:

$$k = \frac{Z_{0e} - Z_{0o}}{Z_{0e} + Z_{0o}} \tag{1-24}$$

From equation (1-22) and (1-23) we can see that transmission and coupling between ports 1 and 3 when $l = \frac{\lambda_g}{4}$ are equal to

$$S_{21} = -j\sqrt{1-k^2} \tag{1-25}$$

$$S_{31} = k \tag{1-26}$$

Equation (1-21) and therefore (1-22) and (1-23) are correct as long as the even- and odd-modes phase velocities are identical. In practice, in an inhomogeneous medium, this is not true. It becomes necessary to consider that the coupling coefficient k depends on the electric coupling coefficient k_C, and the magnetic coupling coefficient k_L. In chapter 2 we will demonstrate this dependency. It will also be discussed that making k_C and k_L identical, is completely equivalent to equalizing even- and odd- modes phase velocities. As aforementioned,

this condition will lead theoretically to an infinite directivity for a quarter-wave length coupled-lines coupler.

We discussed in this part about couplers generalities and the validity of the coupled lines coupler theory which will serve as a basis for this thesis. There exist many other directional couplers. Next part will be addressed to an overview of various solutions for directional couplers in the current market.

1.2. General types of directional couplers and applications

Three kinds of couplers are particularly interesting for RF applications because of their performances and their compatibility with the technologies: the branch-line coupler, the coupled lines coupler and the Lange coupler which is an extension of the coupled lines proficiencies. A review of these three couplers as well as a discussion of their applications is made in this section.

1.2.1. Branch-line coupler

1.2.1.1. Overview

The branch-line coupler, also known as quadrature (90°) hybrid coupler, is a 4-port network as shown in Figure 1-3 [4].

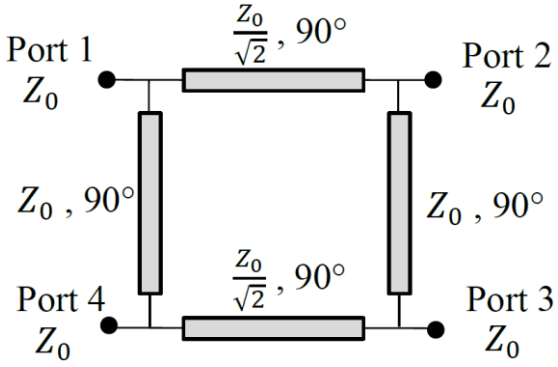

Figure 1-3: Branch-line coupler.

In this structure, Port 1 is the "input" while Port 2 and Port 3 are the "outputs", namely "through" or "direct" and "coupled" ports, respectively. Port 4 is the "isolated" port. The coupler is composed of four transmission lines. Every transmission line is a quarter wavelength section and it has a characteristic impedance of either Z_0 or $Z_0/\sqrt{2}$, as in Figure 1-3. The length of each arm could be reduced in order to save space; however, this will lead to a decrease of the bandwidth.

Any signal entering at input port splits into two quadrature signals on port 2 and port 3 while no power flows to port 4. In the ideal case, the structure does not have any losses and all ports are well matched. The scattering parameters of this structure follow the form:

$$[S] = \frac{-1}{\sqrt{2}}\begin{bmatrix} 0 & j & 1 & 0 \\ j & 0 & 0 & 1 \\ 1 & 0 & 0 & j \\ 0 & 1 & j & 0 \end{bmatrix} \tag{1-27}$$

According to Eq. (1-27), input power is half divided to ports 2 and 3; and the phase difference between those ports is 90°. Branch-line coupler is good for tight-coupling; but it presents narrow bandwidth. This device is a particular case in the set of directional couplers, commonly used for 3-dB coupling factor.

1.2.1.2. Applications

The branch-line coupler can be used for single antenna transmitter/receiver system or I/Q signal splitter/combiner. Branch-line couplers are also commonly related as a part of the reflection-type phase shifter (RTPS) [5] (Figure 1-4 (a)). Moreover it can be included in a down-conversion mixer [5] (Figure 1-4 (b)).

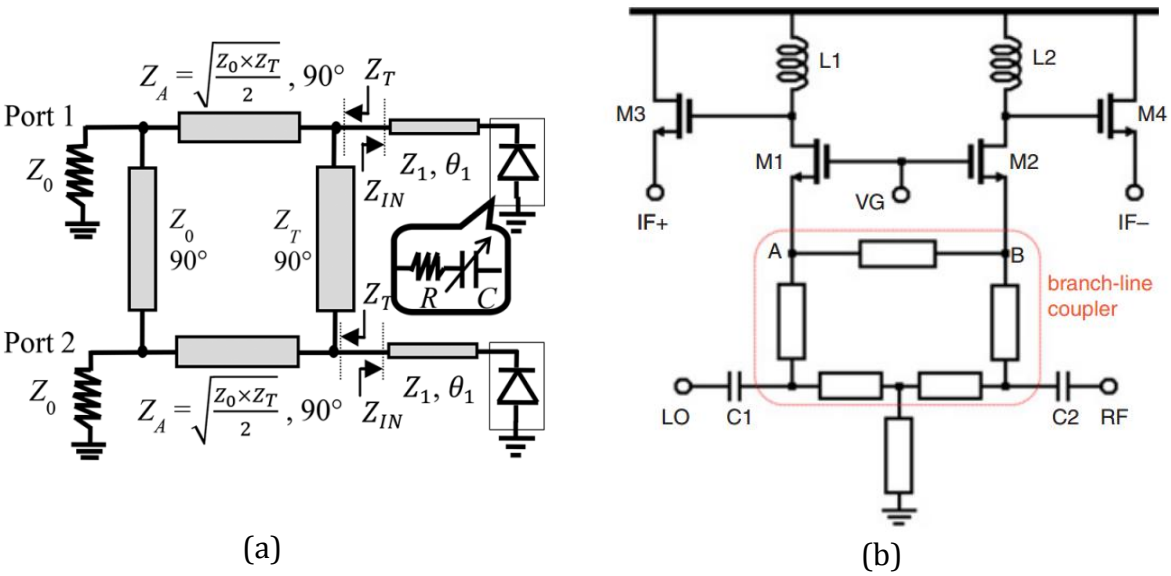

Figure 1-4: Schematic of the (a) RTPS,[5] , and (b) down-conversion mixer, [6], with a branch-line coupler.

The circuit in Figure 1-4 (a) is a RTPS with very high figure-of-merit. 360° of relative phase shift is reached while maintaining good return loss thanks to a 3-dB branch-line coupler and two similar reflective loads, [5]. Circuit in Figure 1-4 (b) presents a 138 GHz down-conversion mixer using a branch-line coupler. The mixer is based on common-gate quadrature-balanced topology [6].

Another kind of applications for branch-line couplers are presented below. In Figure 1-5 a microwave bandpass filter using transversal filtering sections is illustrated. Each section is made up of a classical hybrid with the coupled and direct ports loaded with open stubs in order to generate two input-to-output signal paths. The output port of this circuit is thus the isolated port.

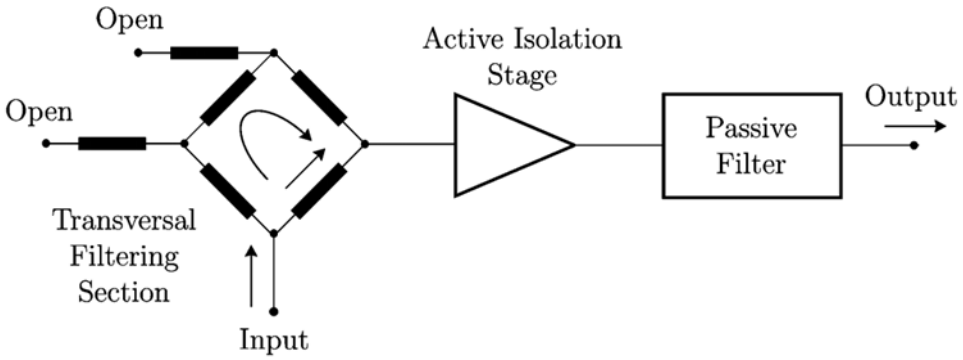

Figure 1-5: Block diagram of the high-selective microwave active bandpass filter [7].

In Figure 1-6 the branch-line coupler is integrated in an optimized design of a Butler matrix. The Butler matrix is a microwave network, employed in beam forming and scanning network. The matrix consists of hybrid couplers, cross couplers and phase shifters. In [8] a reduced size branch-line using two step impedance stubs is developed. Signal entering different input ports in the Butler matrix produce different phase tapers among the output ports [9]. The schematic is shown in Figure 1-6.

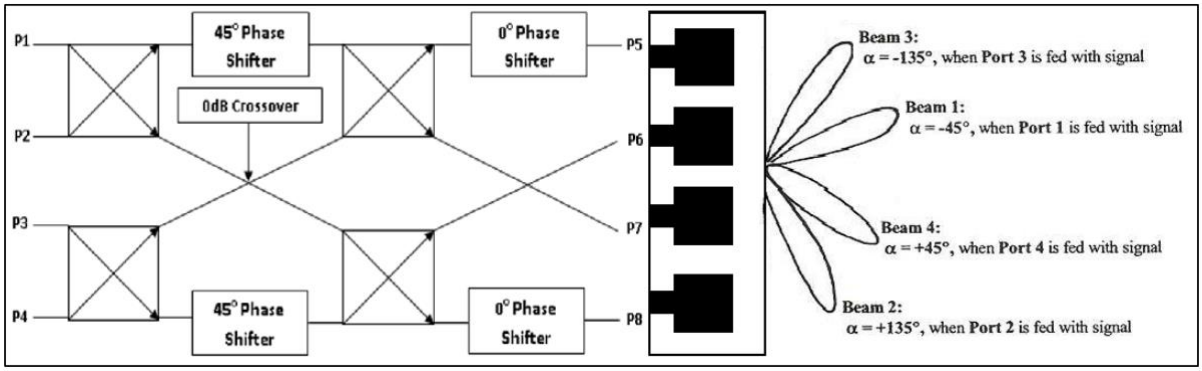

Figure 1-6: Block diagram of a 4x4 Butler matrix [8].

The branch-line coupler has been used during several years for many kinds of applications due to the practical aspects of this device for integration. This coupler has been widely implemented in different systems under 10 GHz. It provides good performances (tight-

coupling) and it is compatible with most of the circuitry technologies at these frequencies. However it remains a cumbersome device. In the next section, the current competitor of the branch-line coupler is presented.

1.2.2. Coupled lines coupler

1.2.2.1. Overview

Two neighboring transmission lines will show coupled power between them due to the interaction between the electromagnetic fields of each line. The proximity of the second line modifies the electromagnetic field of the propagating wave along the first one, transforming thus its characteristic impedance, and reciprocally. This pair of lines is referred to as coupled transmission lines. They can be implemented in different technologies as microstrips (edge or broad-side coupling), CPW, CPS, striplines. We will focus on technologies that could eventually be implemented in an integrated silicon technology, as broadside or edge coupled microstrips). Figure 1-7 shows examples of the implementation of coupled-lines in planar technology [10].

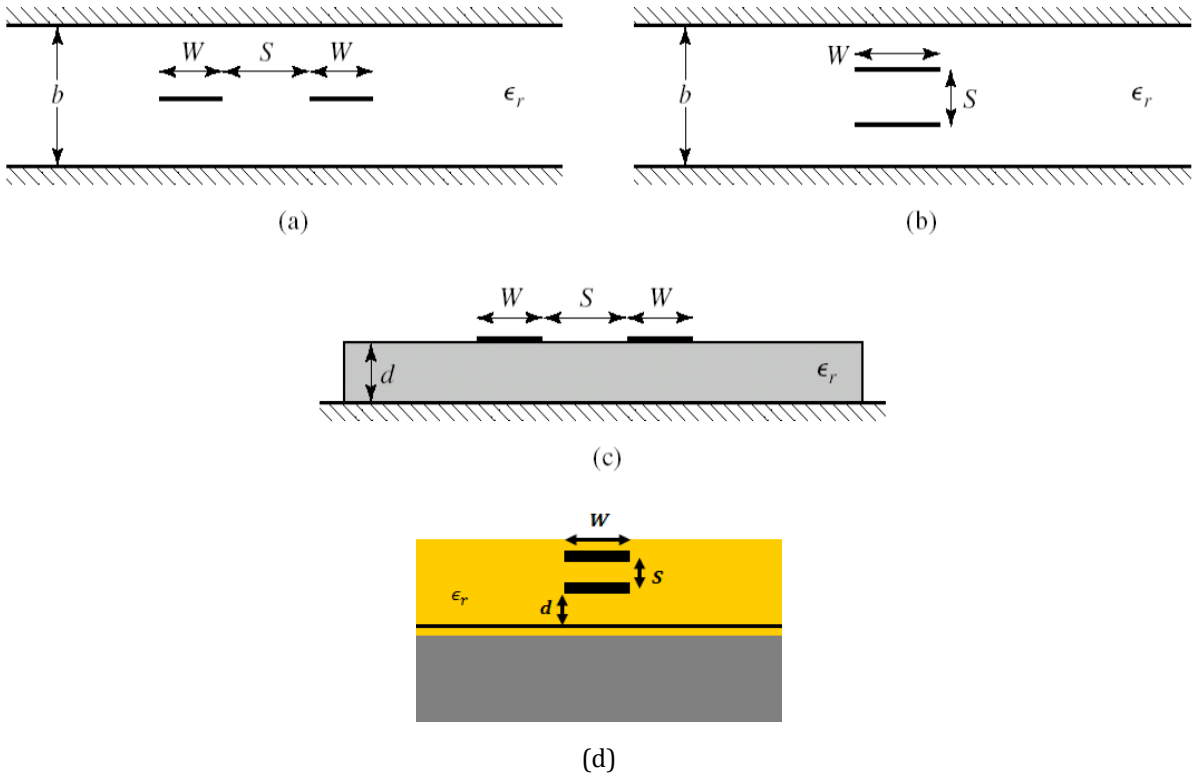

Figure 1-7: Coupled transmission lines geometries. (a) Planar or edge- coupled striplines [10]. (b) Stacked or broad-side-coupled striplines [10]. (c) Planar or edge-coupled microstrip [10]. (d) Stacked or broad-side-coupled microstrip.

Coupled lines topology present many advantages:

- Compatibility with most of the fabrication process
- Reduced surface consumption

- Better bandwidth compared to other solutions such as the branch-line

The stripline topology presents the advantage of being homogeneous in RF. However, this is not the case anymore at mm-wave in a CMOS technology where each metallic and oxide layer differs in thickness and electrical parameters. This results into low directivity because of the signal dispersion. This is also the case for coupled lines in microstrip technology, edge- or broad-side coupling, that have inherently a difference in the even- and odd-modes phase velocity due to the inhomogeneity of the medium. Their design remains simpler to implement than striplines. For this reason, we will focus specifically on microstrip technology for that review, edge- and broad-side.

For edge-side coupled lines couplers, the coupling factor depends on the distance between the two coupled lines. For planar technologies the resolution of the printing process (width of the transmission lines and their proximity) limits the coupling factor. Therefore, tight coupling is very challenging and most of the times 3-dB couplers use a different design in RF as well as in mm-wave. In section 1.3.1, we will see that the broad-side coupled lines coupler has been an appropriated alternative up to now. However, for historical background purpose in terms of application some of the applications for edge-side microstrip coupled lines are presented.

1.2.2.2. Applications

Edge-side coupled lines topology has been widely used during decades because of the straightforwardness of the theory and implementation, besides its bandwidth. In Figure 1-8 the schematic of some applications in the literature are showed.

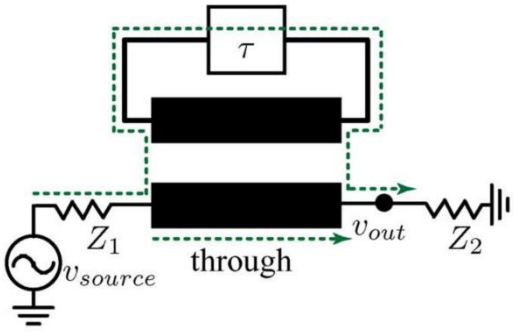

(a)

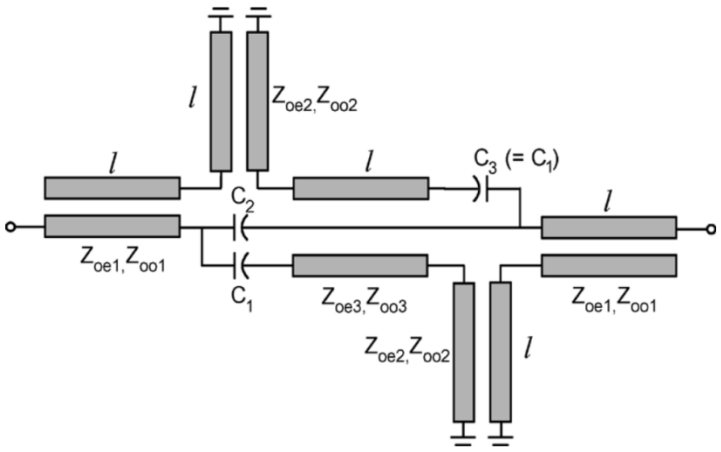

(b)

Figure 1-8: (a) Second-order differentiators, [11], and (b) fourth-order bandpass filter, [12].

In Figure 1-8 (a) a second-order time differentiator composed of a coupled lines coupler and a time delayer is presented, [11]. The time-derivation effect of the coupled lines coupler is demonstrated by applying Kirchhoff's law to infinitesimal electromagnetically coupled transmission lines. And finally in Figure 1-8 (b) the circuit model of a fourth-order coupled lines bandpass filter is shown. The filter is based on $\lambda/8$ coupled-line sections, with multiple capacitive cross-couplings to create four transmission zeros [12].

As we can see, despite the issues for this topology, the coupled lines coupler based on planar edge-side coupling microstrips has been used in a large spectrum of applications. As its drawback essentially concerned tight coupling, an expansion towards interdigitated coupled lines sections was proposed by Lange. Inherently, the Lange coupler principle can be declined in various topologies of coupled lines, as it is the case for the coupled lines coupler itself. For similar reasons, striplines topologies are not presented. Broad-side topology will be focused on in section 1.3.1. Hence, next section highlights the historical background for planar edge-side coupling microstrips in a Lange coupler configuration.

1.2.3. Lange coupler

1.2.3.1. Overview

The interdigitated directional coupler was invented by Lange in [13]. Also called the Lange coupler, it consists of interdigitated parallel, coupled microstrip lines with alternate lines tied together. A single ground plane, a single dielectric, and a single layer of metallization are necessary [13]. Later the structure was unfolded by Waugh in [14] (see Figure 1-9). It is therefore a suited topology for microwave integrated technology. Lange coupler has been reported by different authors [15]-[18]. Thanks to the interdigitated configuration, that stronger coupling will be reached than with the single coupled lines section.

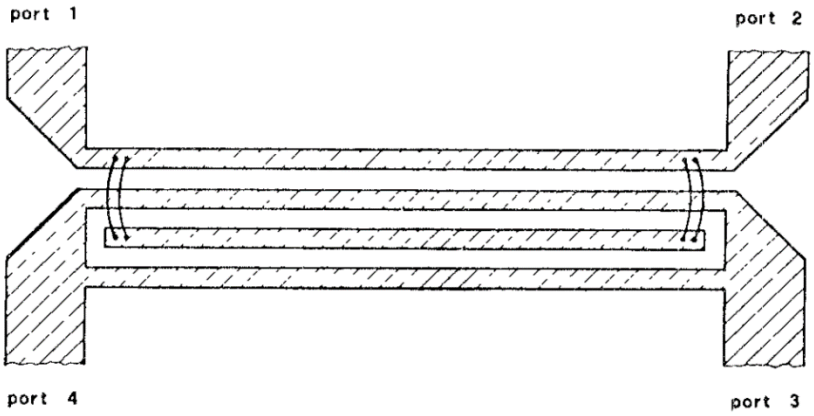

Figure 1-9: Schematic of Lange unfolded interdigitated couplers [14].

Tight coupling is achieved easier than with non-interdigitated edge-coupled lines.

1.2.3.2. Applications

This solution is very effective and popular for the realization of band-tight-coupling devices such as octave-band quadrature hybrids for MIC applications [19]. Lange couplers are used in monolithic integrated circuit (MMIC) because of the high compatibility with the technology. In [20] a Lange coupler is implemented in a GaAs FET technology. In more recent works, Lange couplers are used as a part of different systems as presented in Figure 1-10.

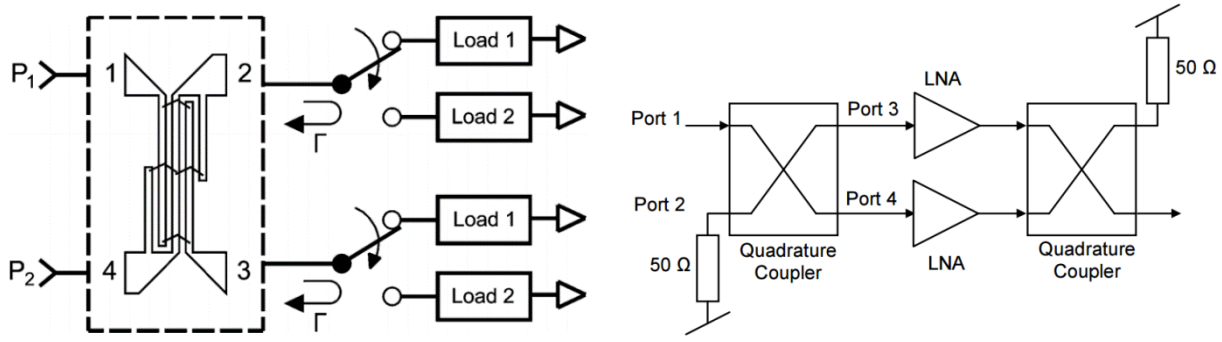

(a) (b)

Figure 1-10: Block diagram of (a) RTPS [21] and (b) balanced amplifier with Lange coupler [22].

In [21] a RTPS of 180° and 90° is implemented using an over-coupled Lange coupler to obtain a multi-octave bandwidth (Figure 1-10 (a)). In [22] a 3-dB Ka-band Lange coupler is integrated in a multilayer thick-film technology in order to realize a balanced amplifier.

1.2.4. Discussion

Coupled lines directional coupler is a very compact for coupling. This technique has been developed for different kinds of topologies (such as microstrip, CPW, CPS, striplines) during the last years, presenting good performances. Striplines topology is homogeneous and presents wide bandwidth but it is not easily implemented in a silicon technology at mm-wave.

As a general rule, microstrip coupled lines and the rest of planar topologies are simple to integrate on silicon and have wide bandwidth. However, they are very limited at mm-wave. Fabrication process limits the achievable levels of coupling and also they present low directivity because of inhomogeneity. Besides, the lack of flexibility in the design does not authorize to compensate for the phase velocity difference due to this inhomogeneity.

The branch-line coupler is a compatible solution for almost all technologies in RF. Nonetheless, it is not a suitable topology in integrated technology because it requires a large surface; therefore it might be a more expensive technique for couplers once integrated in CMOS. In addition, it presents a narrower bandwidth than the coupled lines and it is not good for low-coupling levels.

The Lange coupler is a good technique to overcome the fabrication limitations of coupled lines in edge-side microstrip technology. It enables tight-coupling (more coupling than with simple coupled microstrip lines section) and larger bandwidth than the hybrid. However, due to its microstrip-based topology, it presents the same drawbacks it might present low directivity due to the inhomogeneity of the medium.

To conclude this discussion and historical presentation, there is clearly a strong need in mm-wave integrated technologies, for compact, easy to design, low to strong coupling, high directivity couplers. Because of their advantages in terms of implementation and integration in advanced CMOS/BiCMOS technologies, up to now, broad-side coupled lines appeared to be the most promising approach for mm-wave directional couplers. They were declined in their simple form or as their interdigitated counterpart (Lange coupler). Next section draws up state-of-the-art mm-wave couplers, all based on an integrated broad-side technology. We will make out with their advantages and imperfections.

1.3. State-of-the-art for integrated coupled lines directional couplers

This section will be focused on the review of the current solution to implement 3-dB couplers in CMOS technology for mm-wave applications. As already mentioned, the previous couplers presented in section 1.2 are not always suitable for mm-wave applications because they are not compatible with advanced technologies. Hybrids are bulky, striplines coupled lines are no longer homogeneous, microstrip lines coupled lines are restricted in terms of high coupling due to process rules and Lange couplers are complex to design. Broad-side microstrip coupled lines are the most interesting candidate, as long as the medium inhomogeneity could be compensated for better directivity.

For these reasons, this section is focused on broad-side directional couplers only. The broadside solution is today one of the most implemented structure because of its compatibility with CMOS and BiCMOS process and its possibility to achieve high-coupling.

1.3.1. Broad-side directional coupler

A low-loss and high-directivity broadside coupler is proposed in [23]. It employs an array of air-bridges to enhance directivity via its phase-equalization effect on the c-mode and π-modes.

The structure of the proposed broadside coupler is shown in Figure 1-11 (a). It is composed of two broadside-coupled microstrip lines with an array of air-bridges deployed along both edges of the upper microstrip line. The set of air-bridge array results in better than 22 dB isolation from 27 GHz to 40 GHz on simulation. This isolation can be further extended down to 20 GHz by adding interdigital-capacitors at both ends of the upper and lower microstrip lines as shown in Figure 1-11 (b). Those capacitors are here to compensate the phase velocity.

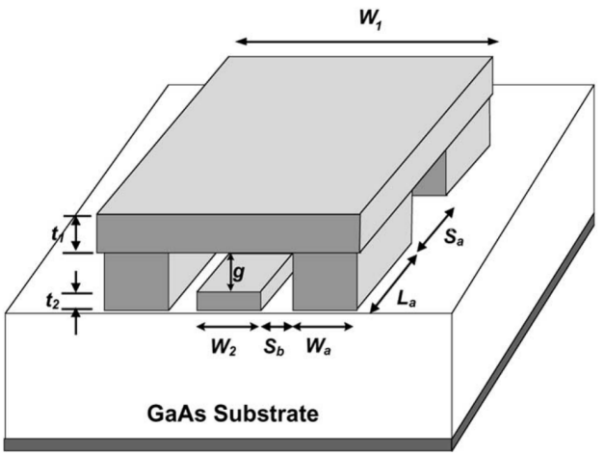

(a)

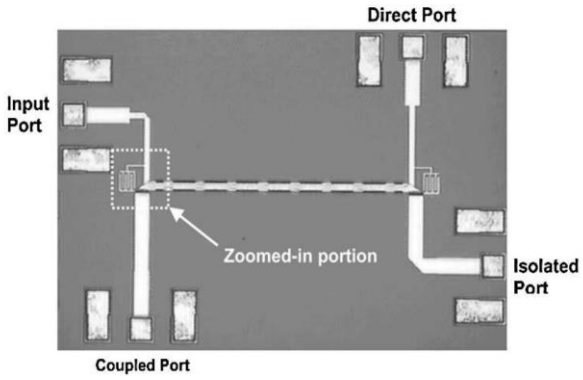

(b)

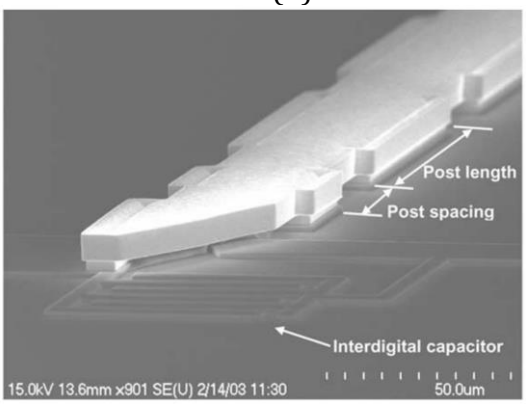

(c)

Figure 1-11: (a) Cross section of the proposed coupler with an array of air-bridges and (b) Microphotography of the coupler[23].

The 3-dB quadrature MMIC coupler in [23], fabricated on a 75-µm GaAs substrate, demonstrates in measurements isolation greater than 18 dB, ±0.7 dB in amplitude imbalance, and 6° in phase deviation from quadrature in the frequency range of 20 to 40 GHz. The advantage of this coupler is that it does not require modification of a standard foundry process and is insensitive to the conductor alignment process.

It is presented in [24] the design, fabrication and characterization of a 3-dB broadside K-band coupler integrated with a specifically developed low loss multi-layer Above-IC technology. The performances are attributed to the specifically developed technology and the optimization of the design methodology. The multilayer technology presented in [24] has been used to implement a multilayer broadside coupler, which cross section is presented in Figure 1-12 (a).

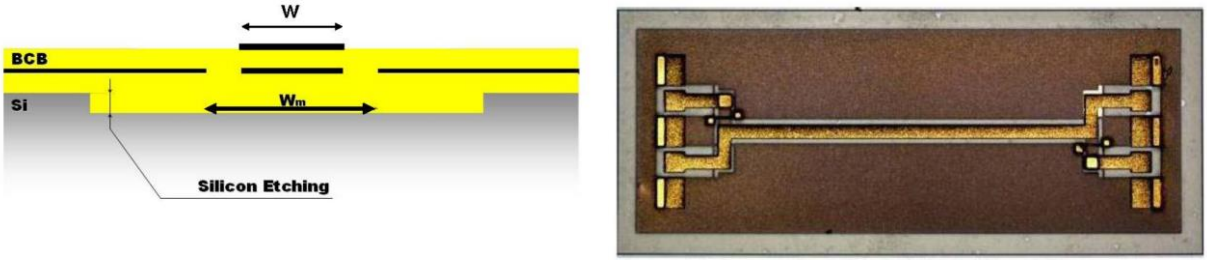

(a) (b)

Figure 1-12: (a) Cross section of the multilayer Above IC broadside coupler and (b) photography of the fabricated broadside coupler [24].

The photography of the fabricated design is presented in Figure 1-12 (a). This coupler occupies a surface of less than 1mm^2. The measurement of this coupler showed 2.7 dB through and 3.9 dB coupling at 20 GHz, which is equivalent to an amplitude mismatch of 1.2 dB and insertion losses of only 0.25 dB. The low losses are due to the developed technology with BCB.

As part of a I/Q mixer, a broadside coupler that has a top view similar to single Q-CPW is incorporated in [25]. This allows to simplify the mixer configuration. The cross-sectional view of the coupler is shown in Figure 1-13 (a).

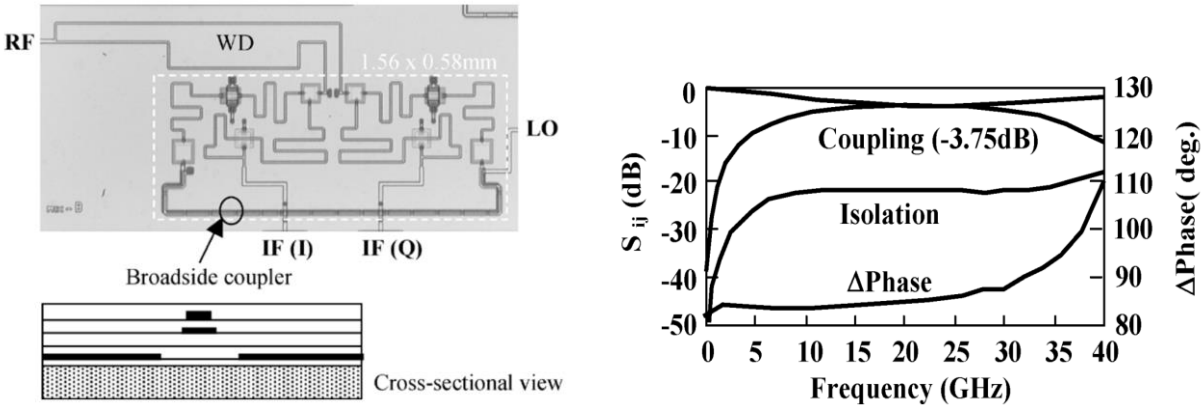

(a) (b)

Figure 1-13: (a) Microphotograph of a 3-D MMIC I/Q Mixer. The area closed by white dotted lines includes a pair of resistive mixers and a broadside coupler. The cross-sectional view of broadside coupler is also shown. (b) Measured performances of a broadside coupler with slit [25].

The coupler in Figure 1-13 (a) consists of a pair of conductor strips on the second and third metal layer respectively. Measured performances of the coupler are shown in Figure 1-13 (b). Both coupling and through paths exhibited a -3.75 dB transmission, that is, merely 0.75 dB of insertion loss. The return losses are better than 15 dB. Finally isolation was greater than 20 dB, and phase difference not optimized for this design was nearly 86° from 18 to 28 GHz.

In [26] five different couplers are presented and compared. Among the couplers, a broadside coupler is designed and measured. The layer and the layout of the coupler are presented in Figure 1-14 (a).

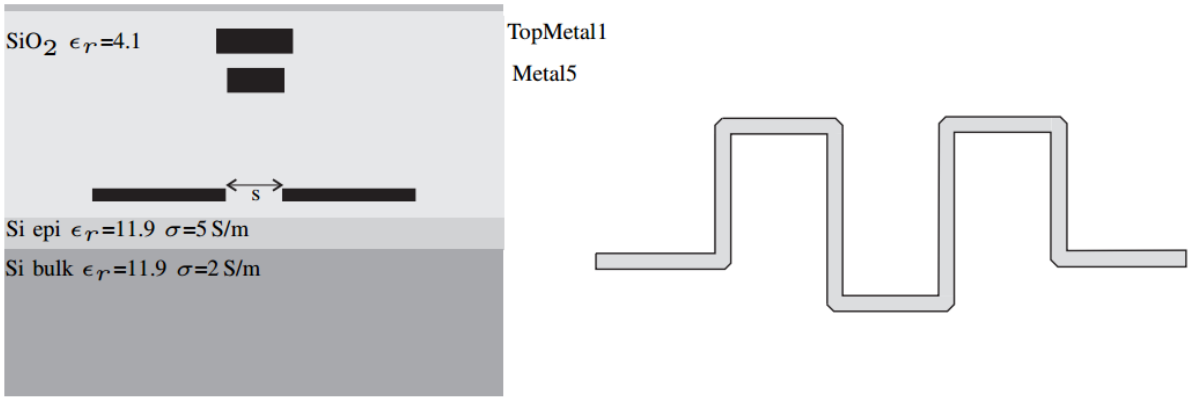

(a)

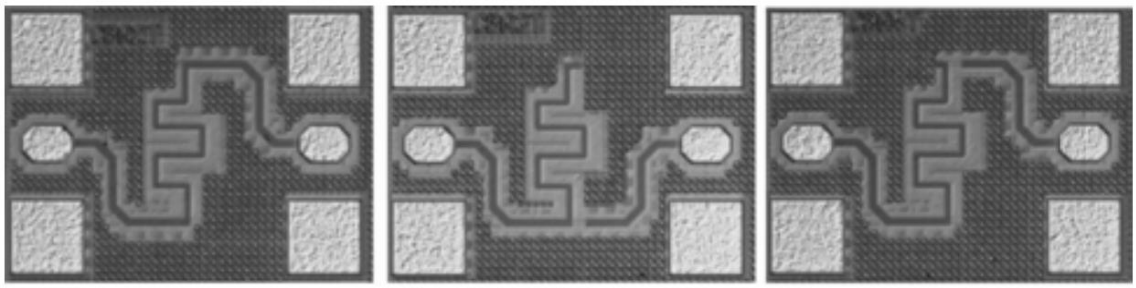

(b)

Figure 1-14: (a) Layer stack (left), layout (right) and (b) Chip micrograph of broadside coupled directional coupler [26].

In Figure 1-14 (a), the lower metal layer is directly below the upper conductor and is not seen in the layout. The slit in the ground plane increases the coupling of the structure. The coupler has been placed three times to measure 4-port S-parameters with a 2-port VNA (Figure 1-14 (b)). The transmission coefficients at 110 GHz are 4.15 dB in measurements. The couplers have a 3-dB bandwidth of 156 GHz with corner frequencies at 32 GHz (measured) and 188 GHz (simulated). The measured isolation is above 12 dB. The phase difference between direct and coupled port is between 81° and 90° for the measured band from 20 GHz to 140 GHz. These results are interesting for mm-wave applications; however, the isolation of 12 dB is not so high. This is due to the lack of compensation of the inhomogeneity of the medium.

An alternative approach for the implementation of a Lange coupler is done in [27]. It exploits the tightly stacked CMOS metal layers. It implements the unfolded Lange coupler in a broadside coupled lines structure to reduce the size through simple meandering, while enhancing the performances thanks to tight broadside coupling. The die photograph of the fabricated structure is shown in Figure 1-15 (a) and its measured performances in Figure 1-15 (b).

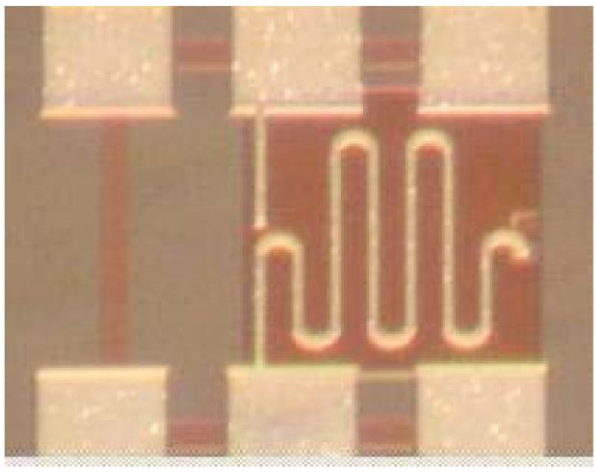

(a)

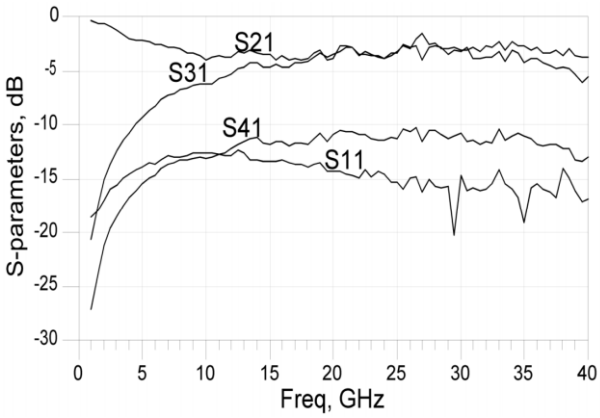

(b)

Figure 1-15: (a) CMOS broadside coupled lines Lange coupler and (b) measured S-parameters [27].

The measurement results (Figure 1-15 (b)) show a broadband performance. They exhibit 3.3 to 3.5 dB through, 3.3 to 3.7 dB coupling, and more than 12 dB isolation and 15 dB return loss across 25-35 GHz. Significant size reduction for the Lange coupler is achieved by implementing this technique.

A broadside coupled lines coupler is used to generate the quadrature signals from the VCO's fundamental output frequency in [28]. The coupler is composed of two metal lines realized in the two topmost metal layers, which are used for the signal paths, while the ground path is realized in the lowest metal layer. A slot in the ground layer is formed beneath the signal lines to enhance the coupling of the structure. The layer stack used to realize the coupler and its 3-D micrograph are shown in Figure 1-16 (a) and (b).

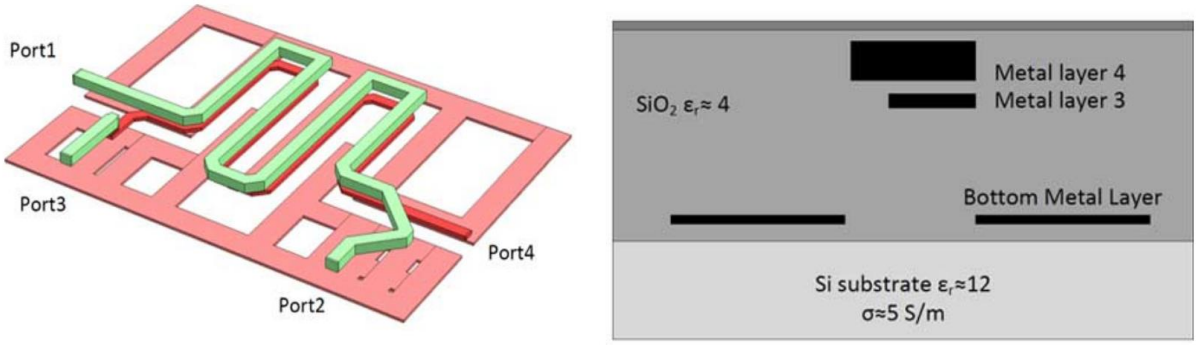

(a) (b)

Figure 1-16: (a) 3-D image of the coupler. (b) Cross section of the coupler metal layer stack [28].

The coupler in [28] has a measured amplitude imbalance less than 1 dB and a phase imbalance less than 2.3° from 65 to 89 GHz. The coupler insertion loss is lower than 5 dB. This coupler topology is selected because of its wideband performance.

A quadrature hybrid at 24 GHz with 3 dB coupling is designed in a 0.18-µm CMOS process in [29]. The diagram is illustrated in Figure 1-8 (a) and a top view of the layout is presented in Figure 1-8 (b). Upper lines are in Metal 6 and lower lines are stacked from Metal 4 to Metal 5. These lines are stacked vertically to achieve high coupling.

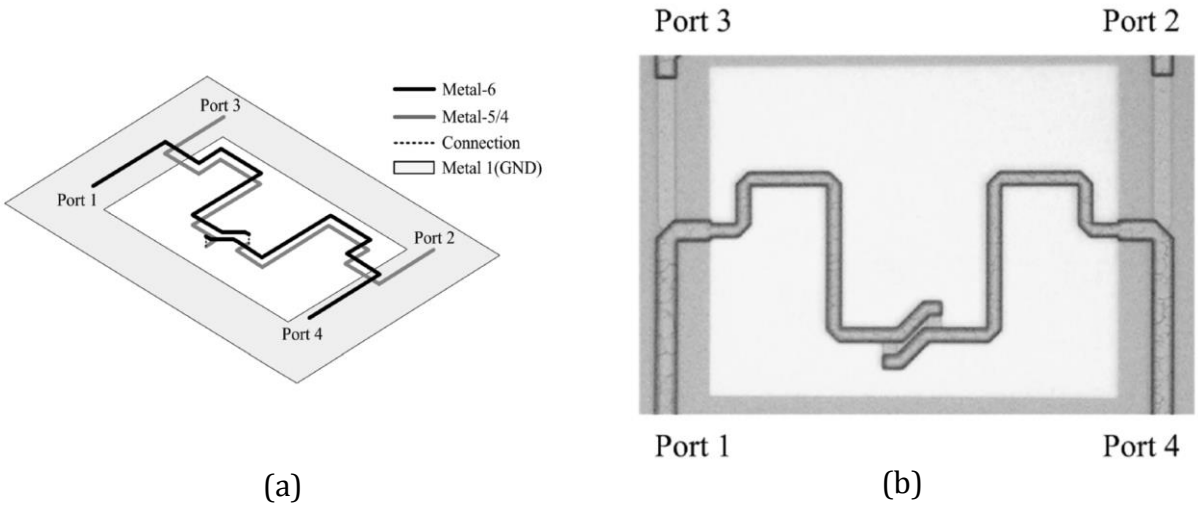

Figure 1-17: (a) Layout and (b) photograph of 24 GHz CMOS quadrature hybrid [29].

The measured phase imbalance of the coupler in [29] is less than $\pm 1°$ and amplitude imbalance is less than 1.4 dB from 21.5 to 26.5 GHz. The return loss and isolation are both better than 20 dB. The interest of this approach is the transformer over-coupling technique, which compensates for the phase degradation. This can be seen as a way to offset the phase velocities.

In [30] a phase shifter is implemented with a broadside coupler. It consists of five stages of reflection-type phase shifter (RTPS), where each stage contains an over-coupling broadside coupler loaded with accumulation-mode MOSTEF varactors, as presented in Figure 1-18.

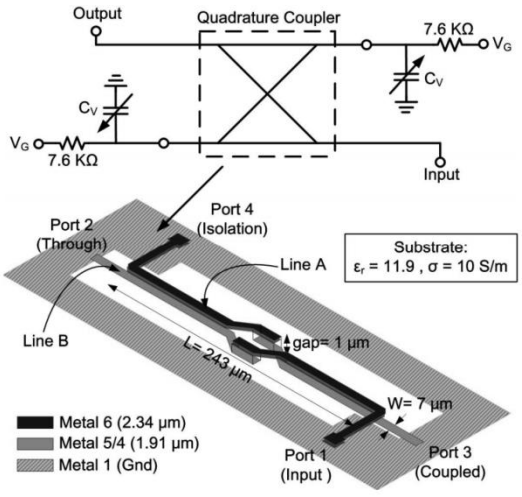

Figure 1-18: Schematic of a single stage of RTPS of the proposed CMOS phase shifter MMIC [30].

The coupler presents in simulation the magnitudes of S_{21} and S_{31} of 3.7 ± 1.7 dB and 3.7 ± 1.5 dB, respectively, and the phase difference between Port 2 and Port 3 is $90.6\pm0.9°$ from 40 to 100 GHz. Finally both return loss and isolation are better than 20 dB. These results indicate an excellent wideband phase balance performance. The over-coupling broadside coupler and single MOS varactor load reduce the size and also achieve low-loss variation.

In references [31], [32] and [34] a broadside coupler is implemented as part of a system. Reference [31] typically describes a wideband RTPS employing a broadside coupler in the multilayer metal structure of a CMOS technology. In [32] a 3-bit RTPS with shunt switches using MEMS technology is implemented; it employs a quadrature hybrid broadside coupler with two reflective loads. Finally in [35] a balanced amplifier is implemented where a meandered broadside coupler with shield is used to reduce the signal loss and dimensions. Unfortunately, the coupler is not measured on standalone in any of these references; measurement results are only for the entire system.

A summary of the main characteristics of broadside couplers in the literature is made in Table 1-1.

TABLE 1-1 STATE-OF-ART BROADSIDE COUPLERS IN CMOS

Ref/Technology	f_0 (GHz)	Size (mm^2)	Coupling** (dB)	Isolation (dB)	Return Loss (dB)	Phase Imbalance (°)	Magnitude Imbalance (dB)
[23]/GaAs 75µm MMIC	20-40	0.55	3.6	18	17	6	0.7
[24]/Aboce-IC Tech.	20	1	3.9	14	20	4	1.2
[25]/3-D MMIC	18-28	0.9	3.75	20	15	4	NA
[26] /IHP 130nm BiCMOS	110	0.02	3.8	13	20	9	NA
[27]/TSMC 0.25µm CMOS	25-35	0.04	3.3-3.7	12	15	4	0.35
[28]/SiGe 0.35µm CMOS	65-89	0.2	<5	17*	17	2.3	1
[29]/0.18µm CMOS	24	0.05	3.7	20	22	0.6	NA
[30]*/TSMC 0.18µm CMOS	40-100	NA	5.4	20	20	1.5	3.2
[31]*/90nm CMOS	60	NA	4	16	16	0	0
[32]*/MEMS	60	NA	3.5	17	18	0	0
[35] */130nm CMOS	19-26	0.036	3.5	NA	20	5	NA

*Only simulation
**Coupling includes insertion loss

The performances presented in Table 1-1 are the results of the couplers used today. Interesting results and techniques are proposed in the references in Table 1-1. As we can see in this table, it is feasible to implement directional coupler at high frequency with CMOS technologies. However, in most of the cases they stay below 60 GHz. At frequencies beyond 60 GHz, many losses are observed. For example, 5 dB are measured instead of 3 dB coupling in [28] or 5.4 dB instead of 3 dB in [30]. Besides, in general terms this structure presents low isolation results for being a 3-dB coupler which means it has a very low directivity. The broadside coupler is a good provisional solution to realize tight coupling in mm-wave but many improvements should be done in terms of performances, especially the directivity.

This thesis is thus focused in the research of an alternative approach for coupled lines compatible with silicon technologies, enabling low to high coupling, up to 3-dB as well as high directivity by compensating the inhomogeneity of the medium. This will be done by considering the available integrated technologies at mm-wave and the transmission lines topologies as slow-wave CPWs.

1.3.2. Integrated technologies available at mm-wave: Discussion

The simulated and fabricated components in this thesis involve the Back End of Lines (BEOL) proposed by STMicroelectronics (STM) industry in the 55 nm BiCMOS technology (also called B55). The B55 BEOL is specially addressed to mm-wave applications. A BEOL is adapted to mm-wave when it shows the minimum losses for 50Ω transmission lines [33]. Figure 1-19 (a) compares different BEOL and Figure 1-19 (b) is a SEM (scanning electron microscopy) picture of the 65 nm CMOS technology BEOL by STM.

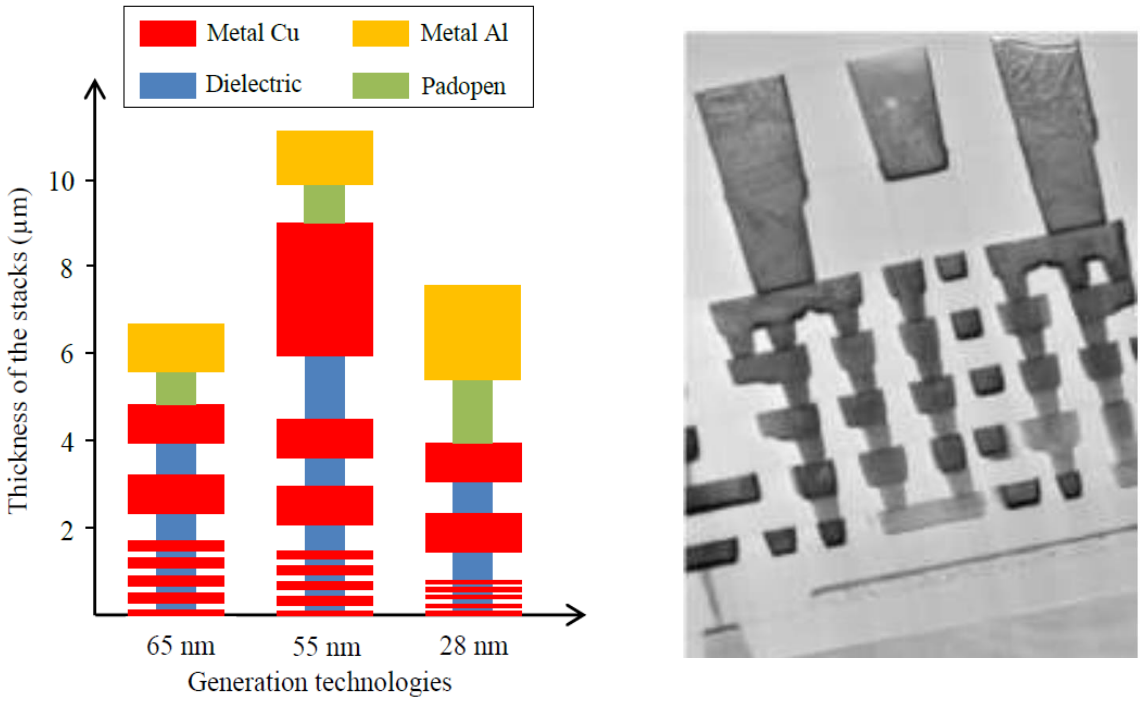

(a) (b)

Figure 1-19: (a) Comparison of different STM BEOL stacks. (b) SEM picture of the 65 nm CMOS technology BEOL from STM [34] .

The BEOLs in Figure 1-19 (a) present at least three thick metal layers (M6, M7 and Alucap) in the upper levels. In the B55 technology, an eighth level (M8) of very thick metal is added before the aluminum cap. The thick layers in B55 (M6, M7 and M8) have the objective to reduce the resistive losses in the interconnections, which allows to realize low-loss passive structures. On the other hand, the dimensions of the lower layers (from M1 to M5) significantly decrease in terms of thickness and authorized small widths for metallic paths. This reduction of

metal layer thickness also leads to a smaller dielectric thickness. Both lead to a decrease in the quality factor of the passive components built in these layers.

Technological limitations are important and must be taken into account. Remarkably, BEOL metal layers density rules must be respected in order to guarantee flatness over the wafer when the mechanical operations are done as CMP (Chemical Mechanical Planarization). Besides, the evolution of the technologies is leading to a reduction of the maximal allowed widths for metallic layers. The broadside coupled lines solution is not the fittest option for implementing directional couplers. For this reason, at IMEP-LAHC an alternative topology is being studied for the last few years: the slow-wave coplanar waveguide is studied in its coupled version.

1.4. Solution: coupled lines based on slow-wave effect

Slow-wave effect is explained in this section in order to show the performances in terms of high quality factor, miniaturization and also, its potential as a structure to reach any level of coupling. First, a review of the transmission lines characteristic parameters is briefly done. Next, the slow-wave coplanar waveguide is introduced as well as the slow-wave effect and its advantages.

1.4.1. Characteristic parameters of the transmission lines

The performances of the transmission lines can be characterized and compared thanks to their self-parameters. The behavior of transmission lines presenting transverse electromagnetic (TEM) wave propagation is usually modeled with the telegrapher model in Figure 1-20. The series parameters denote the effects of conductors: the linear resistance R_l (Ω/m) represents the losses in the resistive conductors and the linear inductance L_l (H/m) represents the reaction of the conductor to the current variation. The parallel parameters denote the effect of the substrate: the linear capacitance C_l (F/m) represents the coupling between the conductors through the substrate and finally the linear conductance G_l (S/m) represents the losses due to the leaks, still through the substrate.

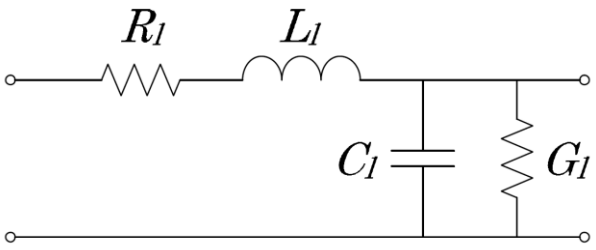

Figure 1-20: Telegrapher model (or RLCG model).

It is also possible to define the behavior of a transmission line with its characteristic impedance Z_c and propagation constant γ. These parameters are linked to the linear parameters with equations (1-28) and (1-29).

$$Z_c = \sqrt{\frac{R_l + jL_l\omega}{G_l + jC_l\omega}} \approx \sqrt{\frac{L_l}{C_l}} \tag{1-28}$$

$$\gamma = \sqrt{(R_l + jL_l\omega)(G_l + jC_l\omega)} = \alpha + j\beta \tag{1-29}$$

It is important to notice that R_l and G_l can be neglected, see (1-28). This is possible to do when transmission lines present very low losses. The characteristic impedance is thus the square root of the ratio between L_l and C_l. The propagation constant can be decomposed into real and imaginary part where α is the attenuation constant which is generally expressed in dB/m and β is the phase constant which is expressed in rad/m.

An approximation of the propagation constant is done in order to present an expression for α and β, see (1-30) and (1-31).

$$\alpha = \frac{1}{2}\left(\frac{R_l}{Z_c} + G_l Z_c\right) \tag{1-30}$$

$$\beta = \frac{\omega}{v_\varphi} = \frac{\omega\sqrt{\varepsilon_{reff}}}{c_0} = \omega\sqrt{L_l C_l} \tag{1-31}$$

where ω is the angular frequency (rad/s), v_φ is the phase velocity (m/s) and c_0 is the velocity in the vacuum which is 3,0e^8 m/s.

The attenuation constant is very useful for interconnections. It allows comparing the performances between two transmission lines: a high attenuation represents a low performance transmission line as a connecting path.

However, when dealing with an electrically fixed length, as 90° phase shift or quarter wavelength, the quality factor Q of a transmission line, defined by [36], is best suited as it represents the phase shift divided by the insertion loss. The higher the quality factor, the most efficient the transmission lines for a given phase shift. According to [37], this definition is true for high quality factors, over 5, which is the case for all the studied transmission lines.

$$Q = \frac{\beta}{2\alpha} \tag{1-32}$$

1.4.2. Slow-wave coplanar waveguide S-CPW

1.4.2.1. Presentation

According to equation (1-32), the improvement of the quality factor can be made either by the reduction of the losses or the increase of the phase constant, and therefore the dielectric constant. [38] showed that the reduction of the wave velocity, obtained by periodically loading a CPW line with floating ribbons, allows increasing the phase constant while the attenuation remains the same. This solution consequently improves the quality factor without modifying the fabrication process.

The slow-wave coplanar waveguide, or S-CPW, consists of a traditional CPW with a floating electromagnetic shielding underneath. The shielding is composed of floating metallic ribbons. The floating ribbons are placed perpendicularly to the direction of propagation at a distance *h* from the CPW, as in Figure 1-21.

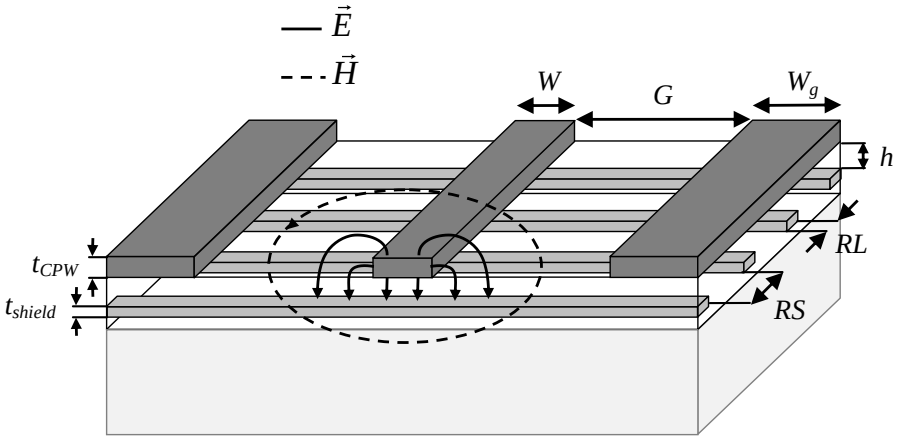

Figure 1-21: Slow-wave coplanar waveguide and the associated electromagnetic field lines.

The floating shielding confines the electric field which does not penetrate through the low-resistivity silicon (for bulk technologies), hence increasing the capacitance while removing the silicon losses. In the same time, the magnetic field remains unchanged and so is the inductance [39]. Finally, the general capacitance *C* increases as compared to a conventional CPW whilst the inductance *L* remains almost the same, hence from a circuit point-of-view, equation (1-33) shows that a slow-wave mode propagates in the S-CPW structure. In other words, electric and magnetic fields are spatially dissociated below the shielding, which means that from now electric or magnetic field can be modified independently without disturbing the other one. Besides, the floating shielding increases the electric coupling which increases the general level of coupling of the structure.

The phase velocity v_φ given by equation (1-33) is therefore reduced in the S-CPW compared to the traditional CPW, hence the name "slow-wave". Consequently, a high relative effective permittivity ε_{reff} is obtained (see (1-34)) leading to a high quality factor Q, since it is proportional to ε_{reff} (cf. equation (1-31)and (1-32)).

$$v_\varphi = \frac{1}{\sqrt{L_l C_l}} \tag{1-33}$$

$$\varepsilon_{reff} = c_0 (L_l C_l)^2 \tag{1-34}$$

In practical terms, the slow-wave structure allows to obtain quality factors Q twice or thrice better than those of traditional transmission lines in the same fabrication technology. Besides, the increase of ε_{reff} leads to an increase also of the propagation constant β (see (1-31)), which leads to a reduction of the physical length of the lines l for a fixed electrical length θ (see (1-35)).

$$\theta = \beta l \tag{1-35}$$

The phase constant β is increased with the slow-wave effect. The attenuation constant is not deteriorated as compared to classical transmission lines, the slow-wave propagation combines therefore both efficient miniaturization and high quality factor. In addition, S-CPW topology allows maintaining a reasonably high value for characteristic impedance in comparison to microstrip or grounded-CPW, even if the high characteristic impedance that could be reached with CPW is no more attainable. A more detailed study of the S-CPWs performances is made in [40], [41] and specially developed in [39]. It is explained how the better stack configuration is chosen.

1.4.2.2. Electrical model

The classical *RLCG* electrical model does not fit well with the physical behavior of the S-CPW, especially when losses have to be considered. Therefore it is necessary to develop a new electrical model based on a fine study of the physical behavior of the S-CPW. However, for the phase velocity calculation, except at very high frequencies as discussed at the end of this section, the series L_l and the parallel C_l are still accurate. As the magnetic field has the same spatial distribution in a S-CPW as in a classical CPW, the modeled inductance L_{CPW} is almost equal for both topologies having the same geometrical dimensions. Similarly, the capacitance C_{CPWG} is almost the same for the S-CPW and the grounded CPW because the electric field is concentrated between the two metal layers in both transmission lines.

Losses do not only come from conductive losses in the CPW strips and substrate losses in the silicon. Conductive and eddy current losses also appear in the patterned metallic shield. This is why the full electrical model is the one proposed in Figure 1-22.

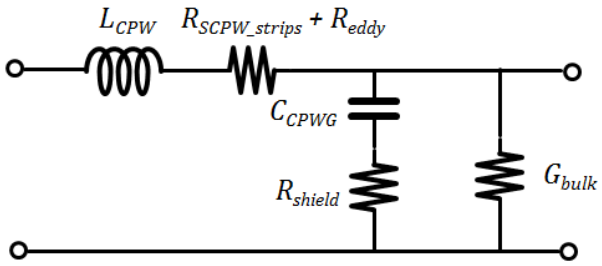

Figure 1-22: Proposed equivalent model.

The resistance $R_{CPW\text{-}strips}$+R_{eddy} includes conductive losses in the CPW strips and eddy currents losses introduced by the patterned shield. Due to the capacitance between the CPW strips and the shield, a current propagates in the floating shield ribbons, leading to conductive losses in the shield modeled as a resistance R_{shield}. In addition, the conductance G_{bulk} expresses the losses in the bulk silicon. In [41], an additional study pointing out the effect of the floating strips length on the loss distribution for both standard Bulk and HR-SOI substrates demonstrated that eddy currents losses induced by the magnetic field into the substrate are negligible for these transmission lines for current gap width *G* (i.e. to about 100 µm). Above 100-150 µm, eddy current losses occur in the low-resistivity silicon substrate. Hence, in practice, if the shield is efficient enough to ensure that no electrical field propagates through the substrate, this term can be neglected. The four last parameters can be extracted thanks to a quasi-static tool. More details about the S-CPW model is explained in [42] and [43]. It is important to state that the *LRCR* model in Figure 1-22 is similar to the *RCLG* model when losses in the shielding are not considered.

1.4.3. Discussion

S-CPWs topology not only present compactness and high quality factor but also could provide tight coupling thanks to high capacitances between signal and grounds via the shielding. Also the shielding might afford new possibilities for coupling design. Hence coupled slow-wave transmissions lines are an interesting solution to address high directivity, low to high coupling and easy and compatible design.

1.5. Conclusion

Broadside coupled lines are the current structure to implement directional coupler at high frequency. An extensive review of the state-of-art for broadside couplers is presented in this chapter. Broadside couplers present good advantages in terms of compatibility with CMOS

technologies as well as reduction of the space occupied by the circuit; besides it is possible to achieve tight coupling with this structure. However improvements should be realized in terms of performances with this structure, especially the directivity and the control of the coupling level.

Transmission lines based on slow-wave effect are therefore introduced as an alternative and effective solution to fabricate high performances circuits in mm-wave. It presents a better quality factor than any other topology of transmission line compatible with CMOS technologies. S-CPWs are a planar structure, which means it is easy to implement in most of the stacks for CMOS or BiCMOS technologies.

Furthermore, slow-wave coplanar waveguide can be used also to reach any coupling at high frequency. The presence of the floating shielding eases the coupling between the conductors and therefore it achieves very tight coupling. In this thesis the detailed development of the theory for coupled-slow-wave-line is presented.

1.6.References

[1] A. Pottrain , “State of the art 200 GHz power measurements on SiGe:C HBT using an innovative load pull measurement setup”, in *Int. Microw. Symp. Dig.*, Montreal, Canada, 2012.

[2] H. T. Nguyen, “Design of Coupled Three-Line Impedance Transformers”, *IEEE Microw. Compon. Lett.,* vol. 24, no. 2, pp. 84-86, Feb. 2014.

[3] D. M. Pozar, “Power dividers and Directional Couplers,” in *Microwave Engineering*, 4th ed., USA: Wiley, 1998, ch. 7, sec. 6, pp. 337-349.

[4] D. M. Pozar, “Power dividers and Directional Couplers,” in *Microwave Engineering*, 4th ed., USA: Wiley, 1998, ch. 7, sec. 5, pp. 333-337.

[5] F. Burdin, Z. Iskandar, F. Podevin, P. Ferrari, "Design of Compact Reflection-Type Phase Shifters With High Figure-of-Merit," *IEEE Trans. Microw. Theory Techn*., vol. 63, no. 6, pp. 1883-1893, Jun. 2015.

[6] D.-H. Kim and J.-S. Rieh, “CMOS 138 GHz low-power active mixer with branch-line coupler,” *IEEE Electron. Lett.*, vol. 48, no. 10, pp. 554-555, May 2012.

[7] Gomez-Garcia, R.; Alonso, J.I.; Amor-Martin, D., "Using the branch-line directional coupler in the design of microwave bandpass filters," ," *IEEE Trans. Microw. Theory Techn*., vol. 53, no. 10, pp. 3221-3229, Oct. 2005.

[8] Rahim, S.K.A.; Muhammad, N.A.; Rahman, T.A., "Beamforming networks using reduced size and Cascaded Butler Matrices," in *European Conf. on Antennas and Propagation (EuCAP)*, Barcelona, Spain, 2010.

[9] J. Butler and R. Lowe, “Beam-forming matrix simplifies design ofelectronically scanned antennas,” *IEEE Electron. Devices*, Apr. 1961.

[10] D. M. Pozar, “Coupled Line Directional Couplers,” in *Microwave Engineering*, 4th ed., USA: Wiley, 1998, ch. 7, sec. 6, pp. 337-349.

[11] H.V. Nguyen, C. Caloz, "First- and Second-Order Differentiators Based on Coupled-Line Directional Couplers," *IEEE Microw. Compon. Lett.*, vol. 18, no. 12, pp. 791-793, Dec. 2008.

[12] W. Chao-Huang, L. Yo-Shen, W. Chi-Hsueh, Chun Hsiung Chen, "Compact microstrip coupled-line bandpass filter with four transmission zeros," *IEEE Microw. Compon. Lett.*, vol. 15, no. 9, pp. 579-581, Sept. 2005.

[13] J. Lange, "Interdigitated Stripline Quadrature Hybrid (Correspondence)," *IEEE Trans. Microw. Theory Techn*., vol. 17, no. 12, pp. 1150-1151, Dec. 1969.

[14] R. Waugh, D. Lacombe , "Unfolding the Lange Coupler (Short Papers)," *IEEE Trans. Microw. Theory Techn*., vol. 20, no. 11, pp. 777-779, Nov. 1972.

[15] W.P. Ou, 'Design equations for an interdigitated directional coupler' *IEEE Trans. Microw. Theory Techn*., vol. 23, no. 2, pp. 253-255, Feb. 1975.

[16] D. Kajfez, Z. Paunovic, S. Pavlin, "Simplified Design of Lange Coupler," *IEEE Trans. Microw. Theory Techn*., vol. 26, no. 10, pp. 806-808, Oct. 1978.

[17] R. Horton, "Variation of lange-coupler geometry with dielectric constant," *IEEE Electron. Lett.*, vol. 15, no. 20, pp. 643-644, Sept. 1979.

[18] R.M. Osmani, "Synthesis of Lange Couplers," *IEEE Trans. Microw. Theory Techn*., vol. 29, no. 2, pp. 168-170, Feb. 1981.

[19] V. Rizzoli, A. Lipparini, "The Design of Interdigitated Couplers for MIC Applications," *IEEE Trans. Microw. Theory Techn*., vol. 26, no. 1, pp. 7-15, Jan. 1978.

[20] R.C. Jr. Waterman *et al.*, "GaAs monolithic Lange and Wilkinson couplers," *IEEE Trans. Electron Devices*, vol. 28, no. 2, pp. 212-216, Feb. 1981.

[21] H.R. Fang, T. Xinyi, K. Mouthaan and R. Guinvarc'h, "180° and 90° Reflection-Type Phase Shifters Using Over-Coupled Lange Couplers," *IEEE Trans. Microw. Theory Techn*., vol. 60, no. 11, pp. 3440-3448, Nov. 2012.

[22] A. Bikiny *et al*., "Ka-band Lange coupler in multilayer thick-film technology," in *Int. Microw. Symp. Dig.*, Boston, USA, 2009.

[23] Sheng-Fuh Chang, "A new MMIC broadside coupler using an array of air-bridges for directivity enhancement," *IEEE Microw. Compon. Lett.*, vol.14, no. 6, pp. 304-306, Jun. 2004.

[24] M.N Do, "Low Insertion Losses Broadside Coupler in a Multilayer Above IC Technology for K-band Applications," in *Int. Microw. Symp.*, Honolulu, USA, Jun. 2007.

[25] T. Tokumitsu, "K-band 3-D MMIC low noise amplifier and mixer using TFMS lines with ground slit," *IEEE Microw. Compon. Lett.*, vol. 15, no. 5, pp. 318-320, May 2005.

[26] B. Laemmle, K. Schmalz, C. Scheytt, A. Koelpin, R. Weigel, "Directional couplers from 30 to 140GHz in silicon," in *Asia-Pacific Microw. Conf. Proceedings*, Yokohama, Japan, Dec. 2010.

[27] M.K. Chirala, Cam Nguyen, "Multilayer Design Techniques for Extremely Miniaturized CMOS Microwave and Millimeter-Wave Distributed Passive Circuits," *IEEE Trans. Microw. Theory Techn*., vol. 54, no. 12, pp. 4218-4224, Dec. 2006.

[28] I. Nasr *et al.*, "A 50-100-GHz Highly Integrated Octave-Bandwidth Transmitter and Receiver Chipset 0.35-µm SiGe Technology," *IEEE Trans. Microw. Theory Techn*., vol. 62, no. 9, pp. 2118-2131, Sept. 2014.

[29] Ting-Yueh Chin *et al.*, "Compact S -/ Ka -Band CMOS Quadrature Hybrids With High Phase Balance Based on Multilayer Transformer Over-Coupling Technique," *IEEE Trans. Microw. Theory Techn*., vol. 57, no. 3, pp. 708-715, Mar. 2009.

[30] Yu-Sheng Su *et al.*, "A V-/W-band 0.18-µm CMOS phase shifter MMIC with 180°-300° phase tuning range," in in *Asia-Pacific Microw. Conf. Proceedings*, Kaohsiung, Dec. 2012.

[31] B. Biglarbegian, *et al.*, "A Wideband 90° continuous phase shifter for 60GHz phased array transceiver in 90nm CMOS technology," in *European Microw. Integrated Circuits Conf.*, Rome, Italy, 2009.

[32] B. Biglarbegian, *et al.*, "MEMS-based reflective-type phase-shifter for emerging millimeter-wave communication systems," in *European Microw. Conf.*, Sept. 2010.

[33] P. Chevalier, *et al.*, "High-speed SiGe BiCMOS Technologies: 120-nm status and End-of-Roadmap Challenges," *topical meeting ion Silicon Monolithic Integrated Circuits in RF systems*, 2007.

[34] N. Seller, "Contribution à l'étude, au développement et à la réalisation d'oscillateurs à contrôle numérique en technologie silicium avancée," Ph.D. dissertation , Université de Bordeaux, Dec. 2008.

[35] H. Shan, C. Saavedra, "A 19–26 GHz balanced amplifier in 130 nm CMOS technology," in *Sarnoff Symp.*, May 2011.

[36] H.P. Hsu, "On the general relation between /α/ and Q (Correspondence)," *IEEE Trans. Microw. Theory Techn*., vol 11, pp. 258-258, 1963.

[37] H. Golde and C. Yeh, « On a relation between α and Q," *Proceedings of the IEEE,*vol. 51, pp. 484-484, 1963

[38] T. Xiao-Lan, A-L. Franc, E. Pistono, A. Siligaris, P. Vincent, P. Ferrari, and J. Fournier, "Performance improvement versus CPW and loss distribution analysis of

Slow-wave CPW in 65 nm HR-SOI CMOS technology," *IEEE Electron. Devices*, vol. 59, pp. 1279-1285.

[39] A-L. Franc, "Lignes de propagation intégrées à fort facteur de qualité en technologie CMOS – Application à la synthèse de circuits passifs millimétriques," Ph.D. dissertation, Université de Grenoble-Alpes, 6 Jul., 2011.

[40] F. Burdin, "Nouvelles topologies de diviseurs de puissance, baluns et déphaseurs en bandes RF et millimétriques, apport des lignes à ondes lentes," Ph.D. dissertation, Université de Grenoble-Alpes, 16 July, 2013.

[41] X. Tang, "Apport des lignes à ondes lentes S-CPW aux performances d'un front-end millimétrique en technologie CMOS avancée," Ph.D. dissertation, Université de Grenoble-Alpes, 8 Oct. , 2012.

[42] Franc, A.; Pistono, E.; Meunier, G.; Gloria, D.; Ferrari, P., "A Lossy Circuit Model Based on Physical Interpretation for Integrated Shielded Slow-Wave CMOS Coplanar Waveguide Structures," *IEEE Trans. Microw. Theory Techn*., vol .61, no. 2, pp.754-763, Feb. 2013.

[43] Bautista, A.; Franc A.-L.; Ferrari, P.; "An Accurate Parametric Electrical Model for Slow-wave CPW," in *Int. Microw. Symp.,* Phoenix, USA, 2015.

Chapter 2

Coupled Slow-wave CoPlanar Waveguide (CS-CPW)

Now that the historical background for slow-wave transmission lines, their interest in integrated CMOS/BiCMOS technologies, and their way of characterization has been described in Chapter 1, it is time to focus on a variant for slow-wave transmission lines, very useful for compactness of circuits: the **coupled slow-wave transmission lines**.

2.1. Introduction

The principle of coupled lines has been widely used in many essential applications in microwave circuits such as filters, DC blocks, phase shifters, baluns [1], balanced amplifiers and directional couplers, [2]-[3]. Such applications may be directly translated towards millimeter waves (mm-wave). At mm-wave, coupled lines are also a crucial component for the on-wafer characterization issues [4]-[6] demanding the implementation of high directivity couplers [7]-[9] . This point will be detailed further in chapter 3.

Solutions have been proposed based on integrated coupled microstrip lines [8]-[10]. The main problem with coupled lines comes with the intrinsic relationship between the electric and magnetic field. Also the inhomogeneity due to the advanced technologies prevents the lines to have the same phase velocity and therefore high directivity. Besides coupled microstrip lines

have limited coupling because of design rules. This is why in this thesis a new solution based on integrated slow-wave coupled lines, namely coupled S-CPW (CS-CPW) is proposed.

Conventional coupled microstrip lines are described in several microwave books, [1]-[3]. However, a brief remainder is made here to give a theoretical background. Besides the coupled microstrip lines limitations at mm-wave are emphasized. Then coupled slow-wave coplanar waveguide are studied in details. The latter offers new possibilities for developing integrated circuits based on coupled lines [11].

For this purpose, after a brief presentation on the coupled microstrip lines theory including their limitations, a rigorous study of CS-CPWs is carried out. The simulation methods as well as the electrical parameters extraction are carefully described. Then, millimeter-waves coupled microstrip lines and CS-CPWs performances are compared. Next, the effect of cutting the shielding in CS-CPW is analyzed. The last part of the chapter will be addressed to some implementation issues.

2.2. Classical coupled microstrip line

The symmetrical coupled microstrip lines consist of a two signal strips integrated on a substrate with a backside ground plane, as shown in Figure 2-1 (a). Being a three-conductor device, two modes will propagate in such structure. The symmetry in the configuration allows us to use the even- and odd-mode approach; which consist in divide the structure into two independent cases (even and odd) and at the end superpose the results of each one of them [12].

The even-mode, plotted in Figure 2-1 (b), is excited when a voltage of the same magnitude and phase is applied to each one of the signal strips. While the odd-mode plotted in Figure 2-1 (c), is excited when a voltage of the same magnitude and opposite phase is applied to each one of the signal strips.

The section of coupled lines can behave as a 4-port coupler which its design has to be optimized in order to get the desired coupling, matching, and isolation. The couplers' design is specified in chapter 3. To begin with, it is necessary to detail the equivalent lumped circuit model from which the coupling coefficients can be calculated.

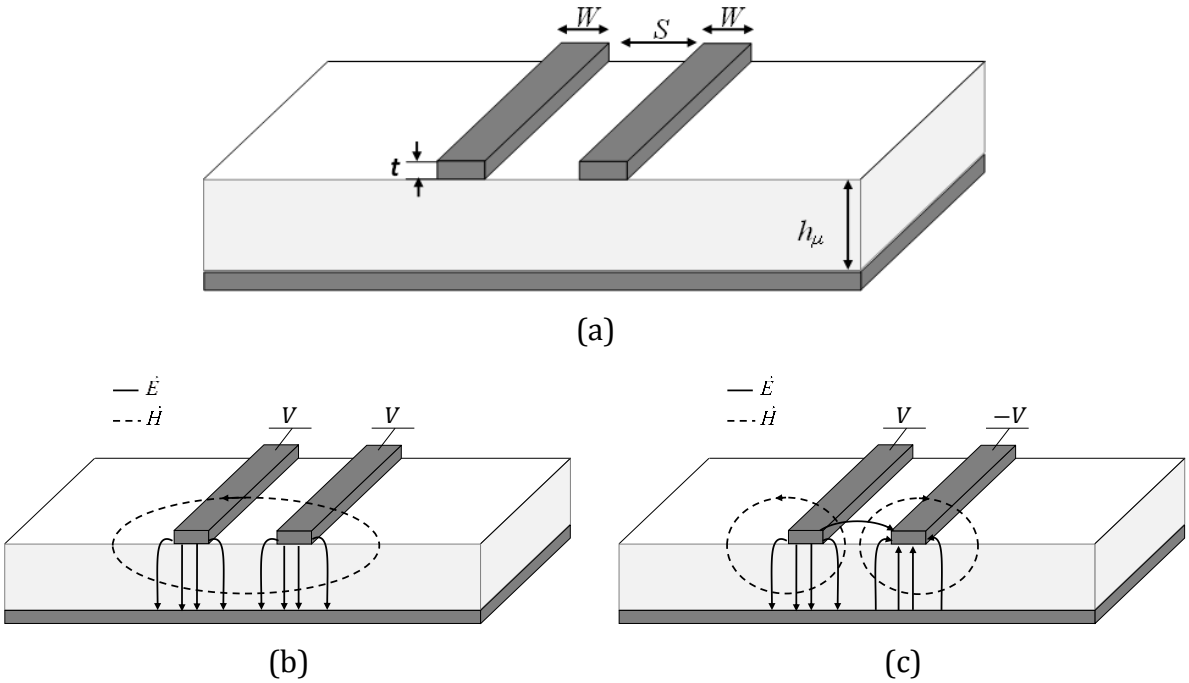

Figure 2-1: Coupled microstrip lines, (a) general configuration and their electromagnetic field: (b) even-mode and (c) odd-mode.

The equivalent circuit is derived from the electrical model given in Figure 2-2 (a), composed of a self and a mutual inductance $L_{0-\mu}$ and $L_{m-\mu}$, along with a self and a mutual capacitance, $C_{0-\mu}$ and $C_{m-\mu}$. The μ subscript stands for microstrip, the subscript m for mutual and 0 for self. As losses are not taken into account, the resistances and conductances will not appear in the presented model. An even- and odd-mode analysis (Figure 2-2 (b) and (c)) is made to derive the coupling coefficients: magnetic coupling $k_{L-\mu}$ and electric coupling $k_{C-\mu}$.

For the even-mode, there is an even symmetry about the center of the structure which means that no current flows between the two strips; thus the symmetry plane acts as a magnetic-wall (open circuit). In Figure 2-2 (b), the equivalent capacitance is determined by the capacitance of either line with the magnetic wall (H-plane). L_{μ}^{even} and C_{μ}^{even} are the even-mode effective inductance and capacitance respectively, they are expressed in equations (2-1) and (2-2).

$$L_{\mu}^{even} = L_{0-\mu} + L_{m-\mu} \tag{2-1}$$

$$C_{\mu}^{even} = C_{0-\mu} \tag{2-2}$$

Similarly for the odd-mode, there is an odd symmetry about the center of the structure which means that a voltage between the two strips is null, thus the symmetry plane acts as an electric-wall (short circuit). In this case Figure 2-2 (c), the equivalent capacitance is determined

by the capacitance of either line with the electric-wall (E-plane). L_{μ}^{odd} and C_{μ}^{odd} are the even-mode inductance and capacitance respectively, they are expressed in equations (2-3) and (2-4).

$$L_{\mu}^{odd} = L_{0-\mu} - L_{m-\mu} \tag{2-3}$$

$$C_{\mu}^{odd} = C_{0-\mu} + 2C_{m-\mu} \tag{2-4}$$

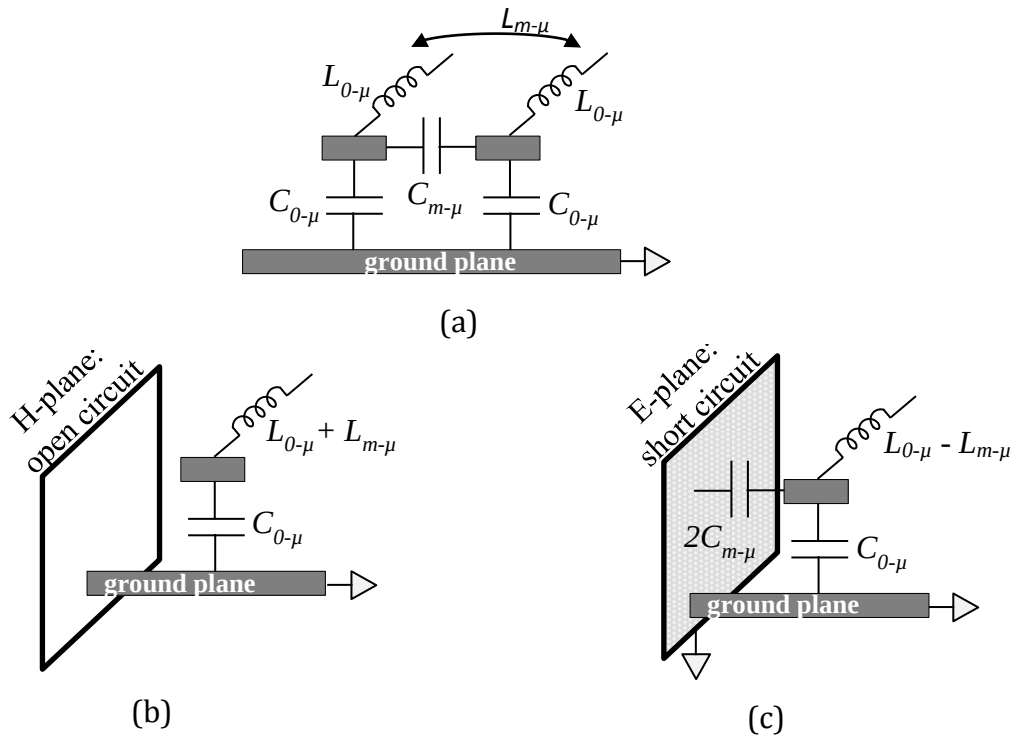

Figure 2-2: Coupled microstrip lines (a) Equivalent electrical circuit, (b) even-mode and (c) odd-mode.

$L_{0-\mu}$, $L_{m-\mu}$, $C_{0-\mu}$ and $C_{m-\mu}$ are imposed by the permittivity of the dielectric substrate and the dimensional parameters, i.e. the separation S between the coupled strips, the height h_{μ} between strips and ground plane, and the strips widths W. The variation of the electrical parameters versus the dimensions are presented in [1],[3], and [13].

The coupling coefficients are then derived as:

$$k_{L-\mu} = \frac{L_{\mu}^{even} - L_{\mu}^{odd}}{L_{\mu}^{even} + L_{\mu}^{odd}} = \frac{L_{m-\mu}}{L_{0-\mu}} \tag{2-5}$$

$$k_{C-\mu} = \left| \frac{C_{\mu}^{even} - C_{\mu}^{odd}}{C_{\mu}^{even} + C_{\mu}^{odd}} \right| = \frac{C_{m-\mu}}{C_{m-\mu} + C_{0-\mu}} \tag{2-6}$$

The general coupling level of a transmission line can be calculated with (2-7).

$$k = \frac{\sqrt{\left(\frac{1+k_L}{1-k_L}\right)\left(\frac{1-k_C}{1+k_C}\right)} - 1}{\sqrt{\left(\frac{1+k_L}{1-k_L}\right)\left(\frac{1-k_C}{1+k_C}\right)} + 1} \quad (2\text{-}7)$$

This expression is valid for coupled microstrip case as well as for any type of structure where k_L is the corresponding magnetic coupling, k_C is the electrical coupling and k the total coupling level.

It can be shown that infinite directivity of a coupled line structure is reached if phase velocities are identical. See condition (2-8):

$$v_\phi^{even} = v_\phi^{odd} \quad (2\text{-}8)$$

It is important to notice that condition (2-8) is equivalent to have:

$$k = |k_L| = |k_C| \quad (2\text{-}9)$$

Equation (2-9) presents the ideal case to provide theoretically infinite directivity. This condition is most of the time not achieved because of the inhomogeneity presented in several technologies. For this reason, in this thesis an approach to achieve (2-9) with any kind of integrated technology is proposed. This approach is not only compatible with any CMOS/BiCMOS technology but also it is straightforward to implement because of its simplicity. In this way, high-performances couplers at mm-wave could be now designed.

2.3.New Coupled Slow-wave CoPlanar Waveguide (CS-CPW) concept

The topology of the CS-CPW is presented in Figure 2-3. The structure is composed of two central signal strips, with coplanar lateral ground strips. Thin floating ribbons (also called floating shielding) of width SL, separated by a gap SS, are placed below as for classical S-CPWs, in order to create the CS-CPW structure. As explained in Chapter 1, S-CPW lead to high miniaturization and high quality factor Q, compared to microstrip or CPW transmission lines implemented in silicon technologies, thanks to their slow-wave behavior [14].

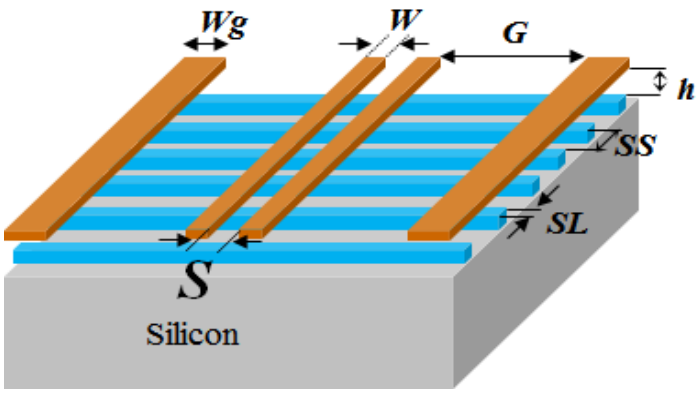

Figure 2-3: Coupled Slow-wave Coplanar Waveguide (CS-CPW).

In this structure, as for S-CPWs, the electric field will be confined between the main strips and the floating shielding; therefore specific capacitances, not present in microstrip or CPW models, will appear in the model. Meanwhile, the magnetic field will be almost not undisturbed by the floating ribbons due to their extremely thin thickness and length, hence the model will present the same inductance as in a classical CPW. This brings a separation of the magnetic and electric fields, which brings the slow-wave effect. This particularity offers a new degree of freedom in couplers' design by letting the magnetic and electric coupling coefficients vary independently. Consequently, magnetic and electric couplings can be controlled separately, depending on the floating shield design.

Based on this statement, the interesting idea developed in the next sections consists in modifying the coupling coefficients k_C and k_L, by cutting the shielding ribbons, either between the two coupled strips (cut in the center, CC-ribbons), or between the coupled strips and the ground strips (cut on the sides, CS-ribbons) [11]. This will be explained in details in sections 2.6 and 2.7.

2.4. Electrical equivalent model for CS-CPW

2.4.1. Equivalent electrical model

For coupled microstrip lines, the electrical model has been used. The developed model for CS-CPW differs due to the presence of the floating shield ribbons. The resulting model can take three forms according to the configuration of the floating shield: uncut, center cut, or side cut. The first one will be detailed below and the last two will be explained in sections 2.6.2 and 2.6.3.

For better understanding, Figure 2-4 presents the steps for the development of the CS-CPW model. The model can be considered as "electrical" since it is based on the electromagnetic behavior. Conductive losses are not considered. First, according to the electric field distribution

in Figure 2-4 (a), the equivalent capacitances are shown in Figure 2-4 (b). Instead of going directly from the central strips to the ground (as in CPW), the electric field is taking a shortcut through the floating ribbons, which adds new capacitances in the model (C_s and C_g). Then in Figure 2-4 (c) the magnetic flux of each conductor in the structure is presented, and its equivalent parameter L_0 is drawn in Figure 2-4 (d). The last interaction to review is the one of the magnetic field between the conductors (Figure 2-4 (e)), represented by a mutual inductance L_m in Figure 2-4 (f). As mentioned before, the magnetic field is almost not disturbed by the presence of the floating shield underneath the coupled CPW, therefore the self and mutual inductances, L_0 and L_m, are almost similar to the ones of a coupled CPW.

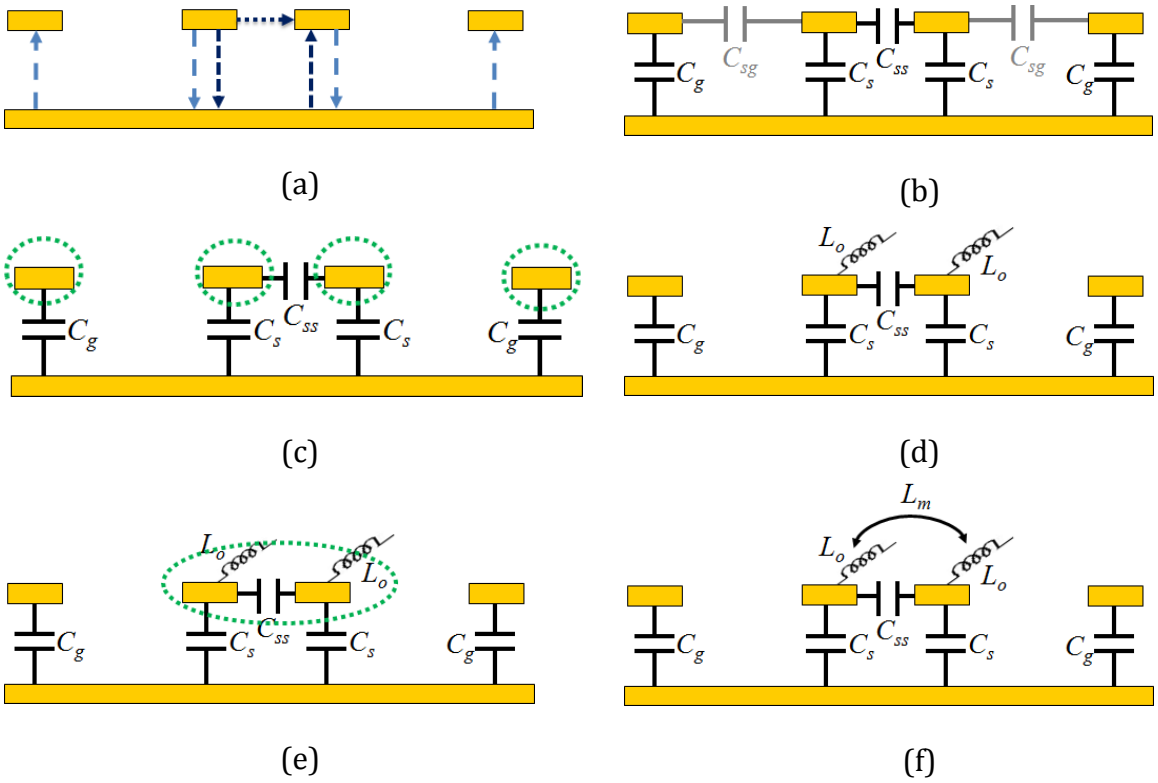

Figure 2-4: Evolution process to propose a new the model for CS-CPW (a) Distribution of the electric field and its (b) equivalent capacitances. (c) Distribution of the magnetic field around each conductor and its (d) equivalent representative inductances and finally the (e) distribution of the magnetic flux between the two central conductors and its respective (f) equivalent mutual inductance.

The final equivalent electrical circuit is given in Figure 2-5. Inductances of the floating ribbons have been added. Depending on design considerations, some elements of the model can be neglected. For example, the capacitance between signal and ground strips, C_{sg} (Figure 2-4 (b)), is often negligible in comparison to C_g and C_s, which are the capacitances between the floating shield and ground or signal strips, respectively. This is valid as long as the gap width G (see Figure 2-3) is much greater than h. Consequently, in this chapter, C_{sg} will not be considered anymore. It is worth noticing that it should be considered for small gaps G reaching twice or

three times the thickness h. This will be the case in the chapter dedicated to filters. Finally, the floating shielding ribbons bring inductances, L_G and $2L_s$, their effect should be considered at very high frequency (from 150 GHz and above) but often neglected in our study, especially in this chapter dedicated to simple analytical models for different topologies.

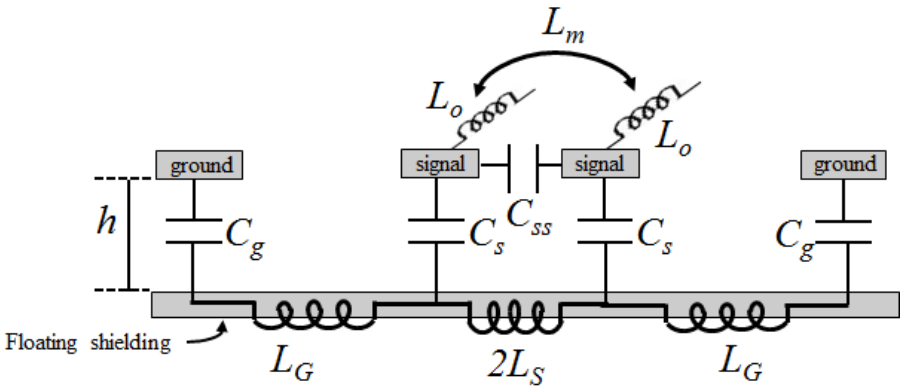

Figure 2-5: Lumped element equivalent circuit model for the CS-CPW.

In practical cases, C_s is greater than C_{ss}, because the gap S is equal to a few micrometers compared to $h \simeq 2\ \mu m$ at a maximum. The reason is purely technological: in CMOS or BiCMOS technologies having a thick top metal layer, the minimum spacing allowed by the design rules for parallel strips patterned on the top metal layer is equal to a few micrometers (~ 5 µm).

2.4.2. Even- and odd-mode Analysis

CS-CPW considered in this thesis are symmetric structures and as explained before, symmetry allows studying the device as two separate circuits (even- and odd-mode approach), as for coupled microstrip lines. Figure 2-6 (a) and (b) represent the electromagnetic fields for the even-mode and odd-mode, respectively. It is expected that the even-mode prioritize the magnetic coupling whilst electric coupling is strengthened in the odd-mode. Figure 2-7 (a) and (b) draw the even- and odd-mode circuits.

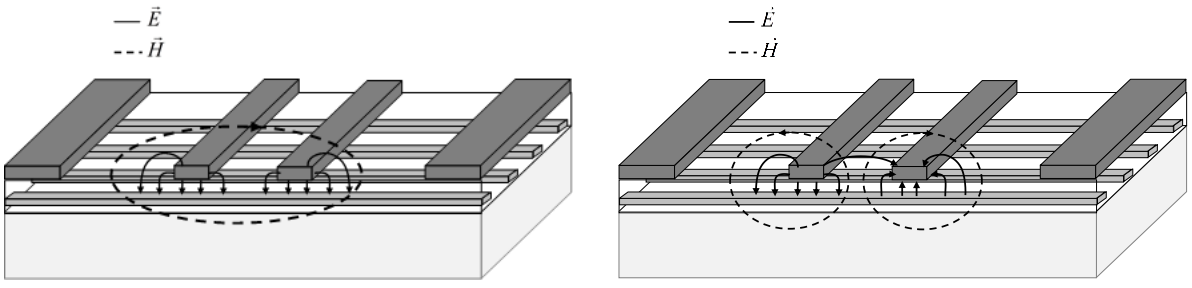

(a) (b)

Figure 2-6: Coupled Slow-wave CoPlanar Waveguide and the associated electromagnetic field, when floating shield ribbons are uncut. (a) Even-mode electromagnetic field lines and (b) odd-mode electromagnetic field lines.

L_0 and L_m inductances being almost not disturbed by the presence of the floating ribbons, as for coupled microstrip lines, L_0 and L_m vary with the distance between coupled strips S; the signal strip width W, and the distance between signal and ground strips G. Equations (2-10) and (2-11) give the relationship between self, mutual, and even- and odd-mode inductances.

$$L_0 = \frac{L^{even} + L^{odd}}{2} \tag{2-10}$$

$$L_m = \frac{L^{even} - L^{odd}}{2} \tag{2-11}$$

On the other hand, even- and odd-capacitances of CS-CPW, C^{even} and C^{odd}, differ from the microstrip case. They are calculated according to the schematic in Figure 2-7, and are given by equations (2-12) and (2-13), respectively.

$$C^{even} = \frac{C_g C_s}{C_g + C_s} \tag{2-12}$$

$$C^{odd} = 2C_{ss} + C_s \tag{2-13}$$

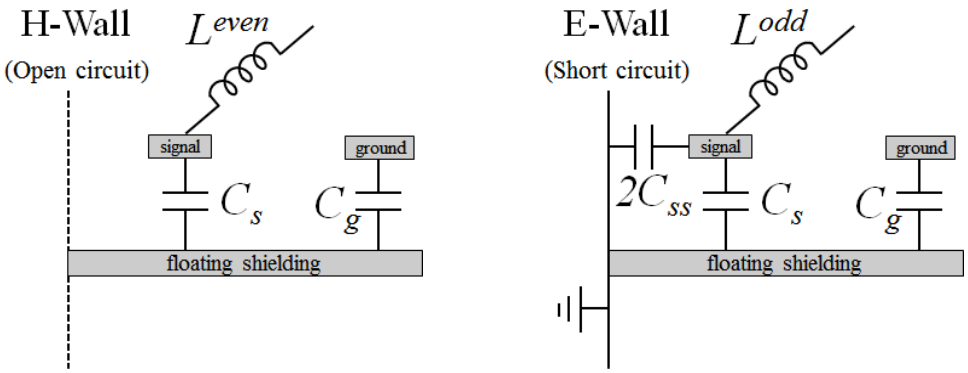

Figure 2-7: Equivalent electrical circuit for CS-CPW with uncut floating shield ribbons. (a) Even-mode and (b) odd-mode.

The coupling coefficients are finally defined by:

$$k_L = \frac{L^{even} - L^{odd}}{L^{even} + L^{odd}} = \frac{L_m}{L_0} \tag{2-14}$$

$$k_C = \left|\frac{C^{even} - C^{odd}}{C^{even} + C^{odd}}\right| = \frac{C_m}{C_m + C_0} \tag{2-15}$$

$$k_C = \frac{C_s^2 + 2C_{ss}\left(C_s + C_g\right)}{C_s^2 + 2\left(C_sC_{ss} + C_{ss}C_g + C_sC_g\right)} \tag{2-16}$$

In the estimation of the electric coupling, the inductance of the shielding ribbons (L_G and $2L_s$ in Figure 2-5) is neglected.

Figure 2-7 and equation (2-16) show that the electric coupling is imposed by C_{ss}, C_s and C_g, thanks to the presence of the floating shielding. This is the degree of freedom brought by the CS-CPW solution, not available while using the coupled microstrip line. Despite this new degree of freedom; there are still some limitations in the control of coupling. Cutting the floating shielding will allow easy control of the electric coupling coefficient without affecting the magnetic one.

2.5.New method to simulate a coupled slow-wave coplanar waveguide and extract its electrical parameters

As previously explained, symmetric structures can be divided into odd- and even-mode. This applies for theoretical developments but also for simulation.

The even- and odd-mode theory allows separating the problem into two, without losing any information on the circuit. Because of their independence, each mode can be studied (or in this case, simulated) in an isolated way and then superposed to the other to find the general response. To sum up, the idea is basically to divide a four-port network into two two-port networks with one main goal: reduce the dimension of the problem for (i) simpler analytical theory and (ii) simulation time and memory saving.

2.5.1. Validation of the method with the microstrip case

The first approach to this issue is the simulation of a well-known structure like a coupled microstrip line in order to validate the proposed algorithm and methodology; then the same algorithm will be implemented for our specific CS-CPW.

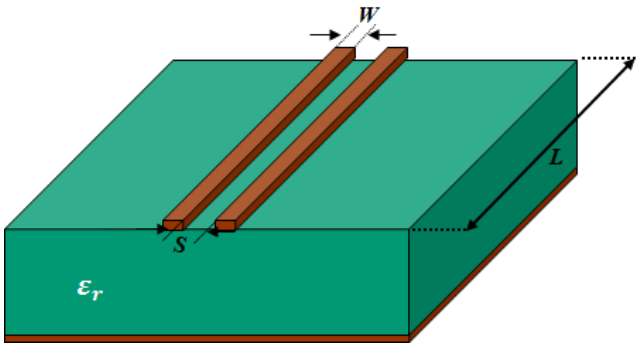

Figure 2-8: Coupled microstrip line (C-µstrip).

The coupled microstrip line (or C-µstrip) being an already known, analyzed and characterized circuit, a considerable amount of data and simulation tools exist. It will help to understand the coupling principle.

2.5.2. Simulation method: even- and odd-mode

In the first part of this section a description of the simulation on HFSS (High Frequency Structural Simulator by Ansys) [16] will be shown, and then it will be compared to the results provided by ADS (Advanced Design System by Keisight) [17].

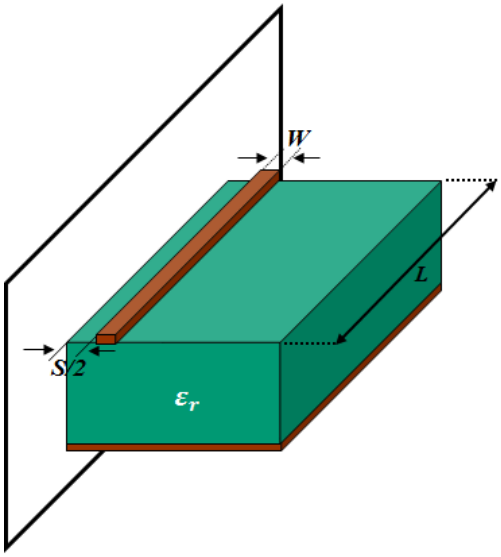

Figure 2-9: Half coupled microstrip line with the symmetry plane.

As previously explained, the study of a C-µstrip can be diced into odd- and even-mode. HFSS is an electromagnetic simulation tool. In this environment it is possible to impose a boundary condition in the structure, thus only the desired mode is excited. To simulate these modes in HFSS only half of the structure will be drawn, as shown in Figure 2-9. Full-wave analysis is required to simulate half a structure with specific boundary conditions on the symmetry plane (Figure 2-10). To simulate the odd-mode, a perfect E symmetrical boundary (short-circuit) must be chosen while a perfect H (open circuit) must be chosen for the even-mode, respectively.

Simulation has been performed using a conventional Rogers PCB substrate as reference, with the characteristics specified in Figure 2-10.

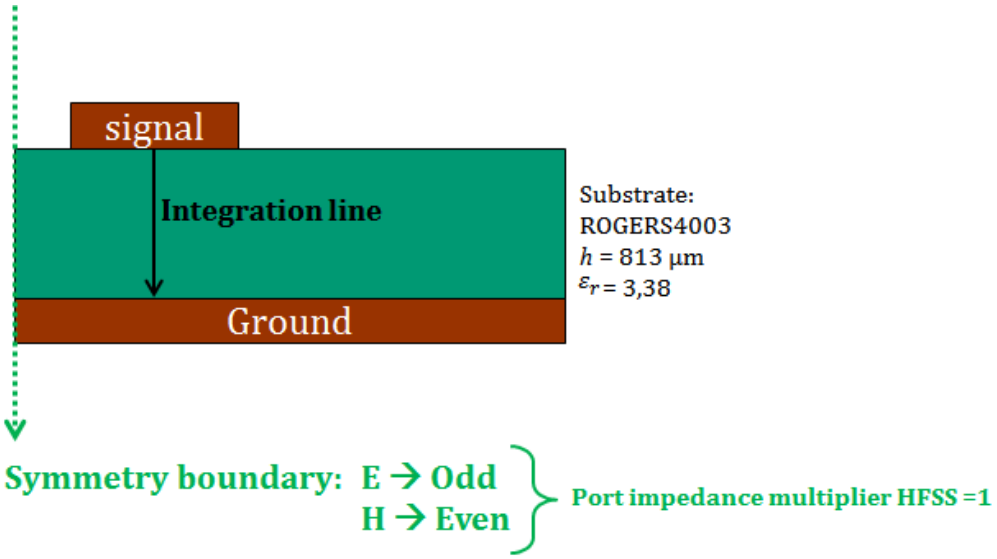

Figure 2-10: C-µstrip: Simulation of even- and odd-mode in HFSS.

Once the simulation with HFSS is done, the S Parameters of even and odd-mode are known. Then the characteristic impedance (Z_C) and the effective dielectric constant (ε_{reff}) are calculated as described in Figure 2-11.

Note: When using a symmetrical boundary, HFSS asks for the port impedance multiplier. It must be equal to 1 for both modes (even/odd). Otherwise ports impedance will be incorrectly renormalized. Ports impedance multipliers of 2 and ½ correspond to common and differential mode, respectively.

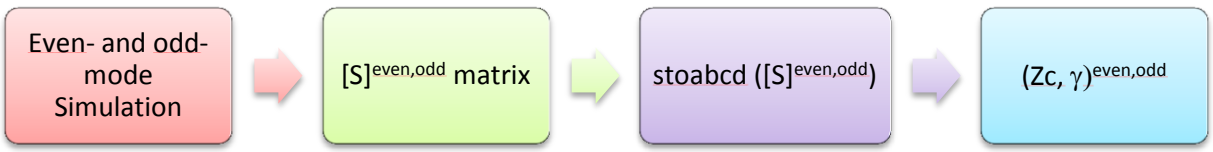

Figure 2-11: Algorithm to extract Zc and γ.

The same process is held in ADS. Simulation of the even- and odd-mode is carried out. ADS being a circuit simulation tool, specific circuits must be realized to simulate the desired modes. In that case the common- and differential-mode are the one implemented in the software and then, when calculating the characteristic impedance (Z_C) from the S-Parameters, it must be divided/multiplied by 2 following the note in Figure 2-12.

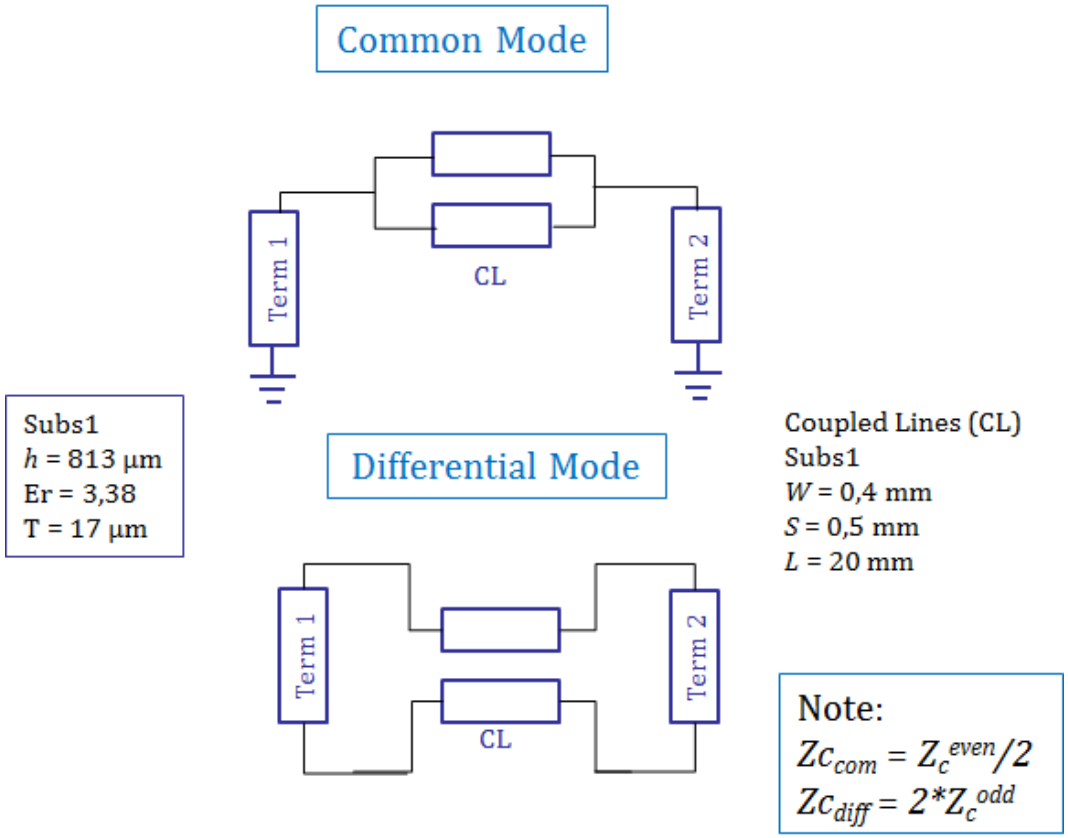

Figure 2-12: Even and odd-modes simulation in ADS.

The results from HFSS, ADS[17] and Linecalc (Transmission Line Calculator from Keisight) are compared in Table 2-1.

TABLE 2-1 COMPARISON OF Z_C AND $\boldsymbol{\varepsilon_{reff}}$ PARAMETERS EXTRACTED

Parameter	Linecalc	ADS	HFSS
Z_c^{even}	123	123	126
Z_c^{odd}	74	74	71
ε_{reff_even}	2.34	2.34	2.31
ε_{reff_odd}	2.26	2.27	2.22

As expected, the S-parameters obtained from simulation with Linecalc and ADS are similar since they both use the same electrical equations. From Table 2-1 the precision of HFSS is also assessed, since the results are similar.

At this point the method to extract characteristic impedance and propagation constant from simulations is validated. In the next section, these two parameters are used to calculate electrical parameters.

2.5.3. Electrical parameters extraction from even- and odd-mode simulation

First, the even- and odd-mode S parameters, S_{ij}^{even} and S_{ij}^{odd}, of the matrices $[S]^{even}$ and $[S]^{odd}$, were extracted and transformed into matrices $[ABCD]^{even}$ and $[ABCD]^{odd}$. Then according to equations (1-18) and (1-19), characteristic impedances, Z_C^{even} and Z_C^{odd}, and propagation constants, γ^{even} and γ^{oodd}, were calculated.

Now, Z_c and γ for each mode will be arranged in two matrices, $[Z_{c\ modal}]$ and $[\gamma_{modal}]$:

$$[Z_{c\ modal}] = \begin{bmatrix} Z_C^{even} & 0 \\ 0 & Z_C^{odd} \end{bmatrix} \tag{2-17}$$

$$[\gamma_{modal}] = \begin{bmatrix} \gamma^{even} & 0 \\ 0 & \gamma^{odd} \end{bmatrix} \tag{2-18}$$

Going through the symmetrical matrix $[M]$ (2-19), the observable matrix $[Z_{obs}]$ is calculated in (2-20):

$$[M] = \frac{1}{\sqrt{2}} \begin{bmatrix} 1 & 1 \\ 1 & -1 \end{bmatrix} \tag{2-19}$$

$$[Z_{obs}] = [M][Z_{c\ modal}][\gamma_{modal}][M]^{-1} \tag{2-20}$$

from which $[R]$ and $[L]$ are derived:

$$[Z_{obs}] = [R] + j\omega[L] \tag{2-21}$$

When losses are not taken into account, $[R]$ is neglected. The term L_{11} of $[L]$ represents the self-inductance (L_0), which is equal to the difference between even- and odd-mode inductances. The term L_{12} represents the mutual inductance (L_m), its equivalent is the sum of even- and odd-mode inductances.

Similarly, $[Y_{obs}]$ is obtained with (2-22). Matrices $[G]$ (negligible in a lossless study) and $[C]$ are derived (2-23). The term C_{11} of $[C]$ represents the difference between even- and odd-mode capacitances while C_{12} is the sum.

$$[Y_{obs}] = [M][\gamma_{modal}][Zc_{modal}]^{-1}[M]^{-1} \tag{2-22}$$

$$[Y_{obs}] = [G] + j\omega[C] = j\omega[C] \tag{2-23}$$

Finally from $[L]$ and $[C]$, the electric and magnetic coupling coefficients are calculated [15]:

$$k_C = \left|\frac{C_{12}}{C_{11}}\right| \tag{2-24}$$

$$k_L = \frac{L_{12}}{L_{11}} \tag{2-25}$$

The process flow to extract electrical parameters from simulations is summarized in Figure 2-13.

Figure 2-13: Algorithm to extract elecrtical parameters from the coupled lines.

Coming back to the previous case of study where a coupled microstrip line was analyzed, and according to Figure 2-13, the next step consists in converting the characteristic impedance and propagation constant from each mode (already extracted in the last section) into the electrical parameters of the transmission line (following Eq. (2-17) - (2-23)). Also from (2-24) and (2-25), coupling coefficients are computed. The results of the coupled microstrip simulation are shown in Table 2-2.

TABLE 2-2 COMPARISON OF Z_C, ε_{reff} AND LC PARAMETERS

Parameter	ADS	HFSS
Z_c^{even}	123	126
Z_c^{odd}	74	71
ε_{reff_even}	2.34	2.31
ε_{reff_odd}	2.27	2.22
Self-C (pF/m)	54.9	55.8
Mutual-C (pF/m)	13.3	15.7
Self-L (nH/m)	498	489
Mutual-L (nH/m)	128	129
k_C	0.24	0.28
k_L	0.25	0.26

As a conclusion, it is worth to notice that simulations in HFSS fits well with the circuit simulation results on microstrip lines. Hence, the deembedding technique afforded by the 3D

electromagnetic simulator will be used in further simulations when dealing with less conventional transmission lines.

Besides, an interesting parameter to focus on is the coupling coefficient, which can be inductive or capacitive. In the case of a microstrip, both coefficients are close to each other (presented in Table 2-2) and they will keep alike because of the strong link between them, irrespective of the topology of the microstrip transmission line. One of the problems with this technology is the difficulty of changing the coupling between the signals while keeping the same characteristic impedance.

2.5.4. Simulation method on the CS-CPW

As for the microstrip case, the even- and odd-mode theory will be used to simulate the CS-CPW and to extract its electrical parameters. From even- and odd-mode simulations, S-Parameters are extracted and converted into propagation constants γ^{even} and γ^{odd} and characteristic impedances Z_c^{even} and Z_c^{odd}; then these two are carried out to build the transmission line electrical model, as suggested in the methodology described in Figure 2-13.

The first step is to carry out the simulation with an electromagnetic simulation tool (in this case HFSS). Figure 2-14 shows the implemented structure. The integration line should be imposed from signal to ground.

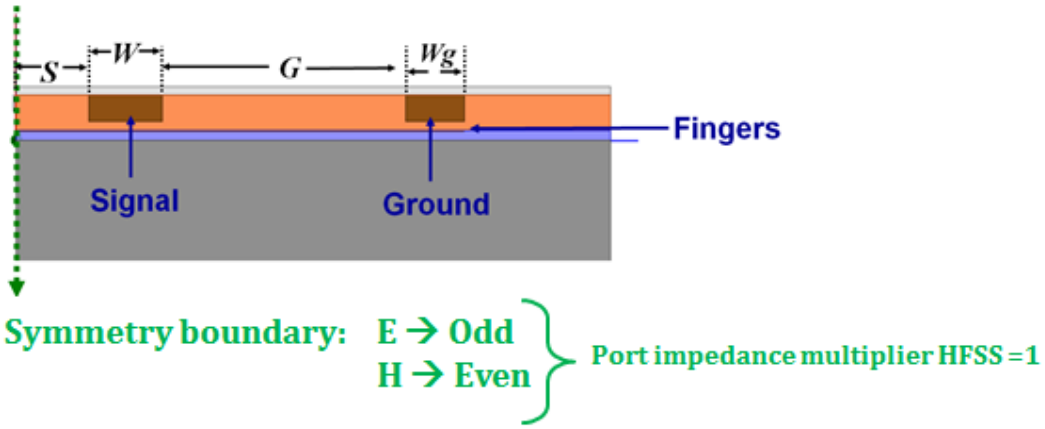

Figure 2-14: Even- and odd-mode simulation in HFSS for CS-CPW.

It is worth mentioning that when imposing the symmetrical boundary, it is important to ensure that the right mode is being excited in the structure. Specifically, during the implementation of a symmetrical E boundary (short-circuit) in HFSS, modifications in the excitation port must be done in order to energize the right mode. Symmetrical H plan (open circuit) does not present this issue. In both cases, HFSS will ask the port impedance multiplier which still should be fixed to 1 for both modes (even and odd).

2.5.5. Simulation results: electrical performance of CS-CPW vs C-µstrip

A simulation was made on the basis of the BiCMOS 55nm technology by ST Microelectronics. A simplified view of the back-end-of-line has already been shown in chapter 1.

The floating shielding was positioned in Metal 5 and both signals and grounds strips from Metal 7 to 8. This configuration leads to a distance h of 2 µm from the floating ribbons to the main conductors and a relative dielectric constant ε_r of 4.32. W_g and G were fixed to 12 µm and 50 µm, respectively. The signals width W varies from 5 to 25 µm. To observe the effect of S on the coupling coefficients, simulations were achieved for two different values (5 µm and 15 µm). Figure 2-15 gives some results for the LC parameters extraction of a slow-wave coupled line when varying the signal width W.

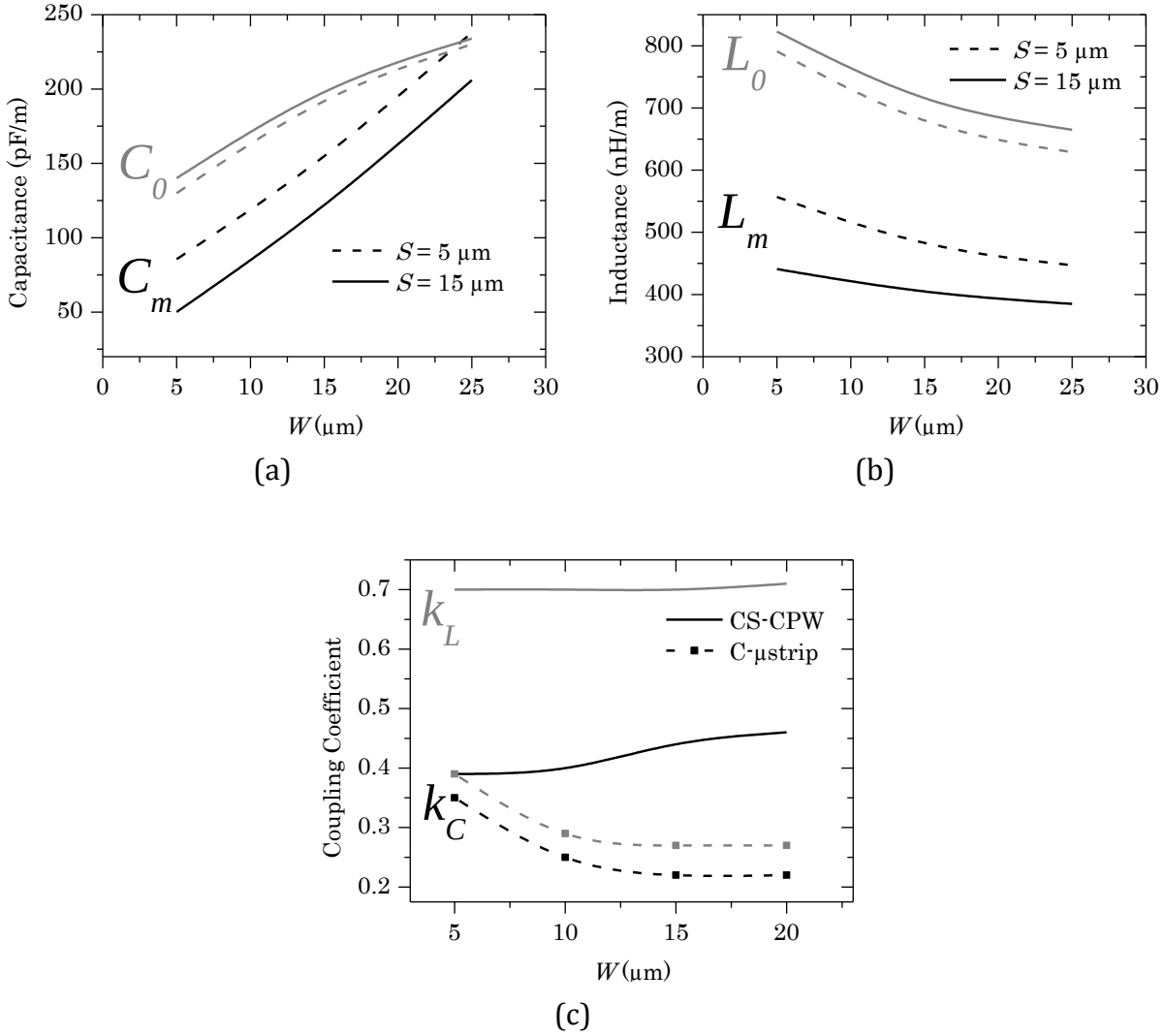

Figure 2-15: LC parameters vs W at 60 GHz. (a) Capacitances for CS-CPW with two different S, (b) inductances for CS-CPW with two different S and (c) coupling coefficients for CS-CPW and C-µstrip with S =5 µm in both cases.

Figure 2-15 presents the first results for a CS-CPW. As expected, capacitances increase with width (Figure 2-15 (a)); meanwhile inductances decrease with width (Figure 2-15 (b)) because magnetic flux decreases. Self-capacitance and self-inductance hardly depend on the distance S between the signal strips, whereas mutual capacitance and inductance do, which means that the coupling coefficient is going to vary with S.

The coupling in a classical coupled microstrip line is also given in Figure 2-15 (c). An interesting phenomenon is observed. As previously mentioned, both coupling coefficients (magnetic and electric) in C-μstrip solution are very close to each other and there is no simple way to control them separately. The difference between them is due to the inhomogeneous propagation medium. On the contrary, slow-wave coupled lines present very different and less related magnetic and electric coupling coefficients. This shows that the presence of the floating ribbons in slow-wave structures allows us to dissociate electric and magnetic coupling coefficients. This means a new degree of freedom in terms of design. In the next section, tunable coupled lines are presented using this effect, and some potential applications are derived.

In Table 2-3, an overview is presented of the variation of the electrical parameters with the design parameters S and W. These results are extracted from simulations in HFSS. For example to observe the effect of only S, W is fixed to 5 μm. h and G are settled all the time to 2 μm and 50 μm respectively.

TABLE 2-3 ELECTRICAL CHARACTERISTICS VERSUS DIMENSIONS

Parameter	$S \nearrow$	$W \nearrow$
L_m	↘	↘
L_0	↗	↓
$k_L = L_m/L_0$	↘	⟶
$C^{even} = C_g C_s/(C_g + C_s)$	⟶	↗
$C^{odd} = 2C_{ss} + C_s$	↗	↗
$\lvert k_C \rvert$	↘	↗

*↗ or ↘ means moderate variation ↑ or ↓ means faster variation. ⟶ means no variation.

The results are as expected. The variation of inductances is similar to the CPW case as predicted: When S is increased, the magnetic flux between the strips decreases thus the mutual-inductance decreases as well; however the proper-inductance (L_0) increases because each conductor is now less perturbed by the other strip. When W increases both inductances decreases.

For the electric field, the most practical way to understand the results are by looking at the capacitances of each mode (C^{odd} and C^{even}). Only the C^{odd} will be affected with S because the interaction signal-signal is only taken into account in the odd-mode; and both capacitances increase with W.

2.6.Cutting the floating shielding

2.6.1. Concept

The interesting idea developed to obtain the desired coupling consists in modifying the coupling coefficients k_C and k_L, by cutting the shielding ribbons, either between the two coupled strips (cut in the center, CC), or between the coupled strips and the ground strips (cut on the sides, CS), as shown in Figure 2-16.

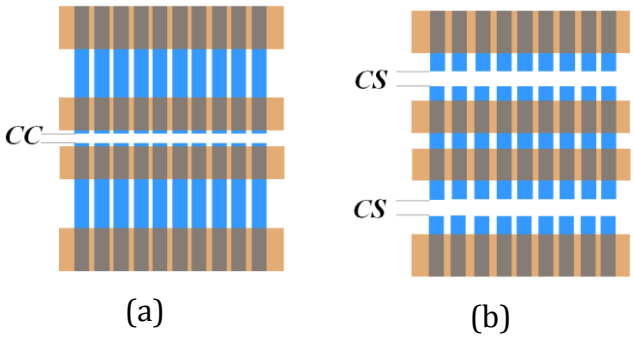

Figure 2-16: CS-CPWs top view. (a) Floating shield ribbons cut in the center and (b) on the sides.

Cutting the ribbons in the center will decrease the mutual capacitance while cutting the ribbons on sides will decrease the self-capacitance. Meanwhile the magnetic coupling coefficient will not change, because the magnetic field is almost unperturbed by the presence of the shielding ribbons. It is then possible to modify the electric coupling coefficient without modifying its magnetic counterpart. The modification of the latter is achieved by modifying the CPW topology as shown in the next sub-section. Therefore, coupling coefficients k_C and k_L can be tuned independently or at the same time, leading to high flexibility in the realization of high to weak couplings with high directivity by always maintaining these coefficients equal to each other.

2.6.2. Cut in the Center (CC)

When the floating shielding is cut between the two coupled CPW signal strips, the equivalent electrical circuit in Figure 2-5 (a) is replaced by that in Figure 2-17 (a). As explained before, the capacitances between the signal strip and the ground strip C_{sg} have been voluntarily omitted, since it is very weak compared to the ones brought by the shielding. C_{ss} is henceforth the only way to electrically control the coupling between the central strips. The cut in the center CC (see Figure 2-16) is fixed to a few micrometers (the influence of the width of the cut is

explored further in this chapter). The even- and odd-mode circuits are depicted in Figure 2-17 (b) and (c).

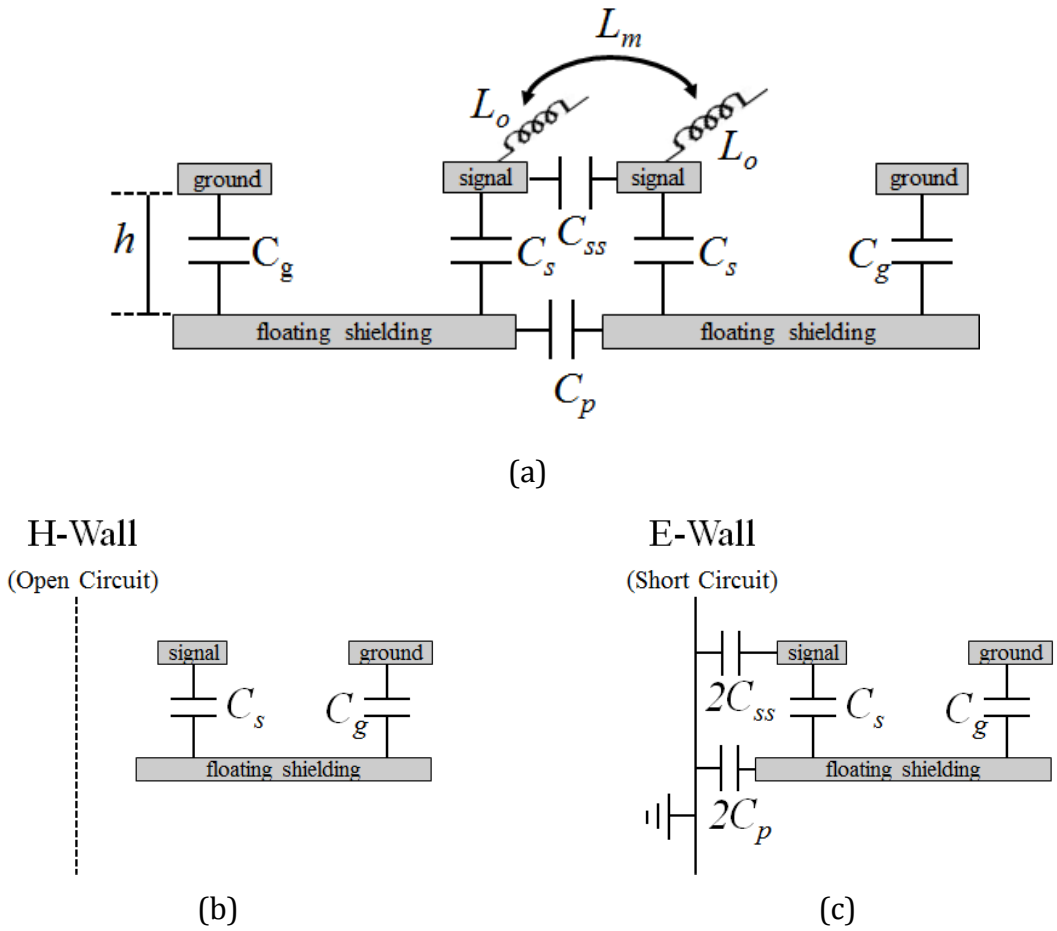

Figure 2-17: CS-CPW with floating shielding cut in the center. (a) Equivalent electrical circuit (b) even-mode and (c) odd-mode.

Only the pattern of the floating shielding has been modified. The dimensions of the CPW and the shielding have not been changed, therefore self and mutual inductances stay the same as in the case without any cut. Consequently, the magnetic coupling k_L keeps identical. On the contraryHowever, the values of the capacitances change. The equations are given in (2-26) and (2-27) for even- and odd-mode capacitances, respectively:

$$C^{even} = \frac{C_g C_s}{C_g + C_s} \tag{2-26}$$

$$C^{odd} = 2C_{ss} + \frac{C_s(C_g + 2C_p)}{C_g + C_s + 2C_p} \tag{2-27}$$

These equations show that even-mode capacitance remains the same while the odd-mode capacitance is reduced compared to the uncut case. The new value for k_C is presented in (2-28).

$$k_C = \left|\frac{C^{even} - C^{odd}}{C^{even} + C^{odd}}\right| = \frac{C_{ss}(C_g + C_s)(C_g + C_s + 2C_p) + C_p C_s^2}{C_g C_s^2 + C_s C_g^2 + 2C_p C_g C_s + C_p C_s^2 + C_{ss}(C_g + C_s)(C_g + C_s + 2C_p)} \quad (2\text{-}28)$$

Based on equation (2-28), the electric coupling coefficient when floating ribbons are cut in the center is expected to be much lower than the one for the case of uncut ribbons. For negligible values of C_{ss} and C_p, it is almost equal to zero.

2.6.3. Cut on the sides (*CS*)

The equivalent circuit corresponding to a floating shielding cut on the sides, along with the even- and odd-mode models, is presented in Figure 2-18. As for the center cut, the length of the cut, *CS*, is equal to a few micrometers. A parasitic capacitance C_p (Figure 2-18 (a)) must be taken into account especially in the even-mode (Figure 2-18 (b)). This parasitic capacitance is not affecting the odd-mode (Figure 2-18 (c)).

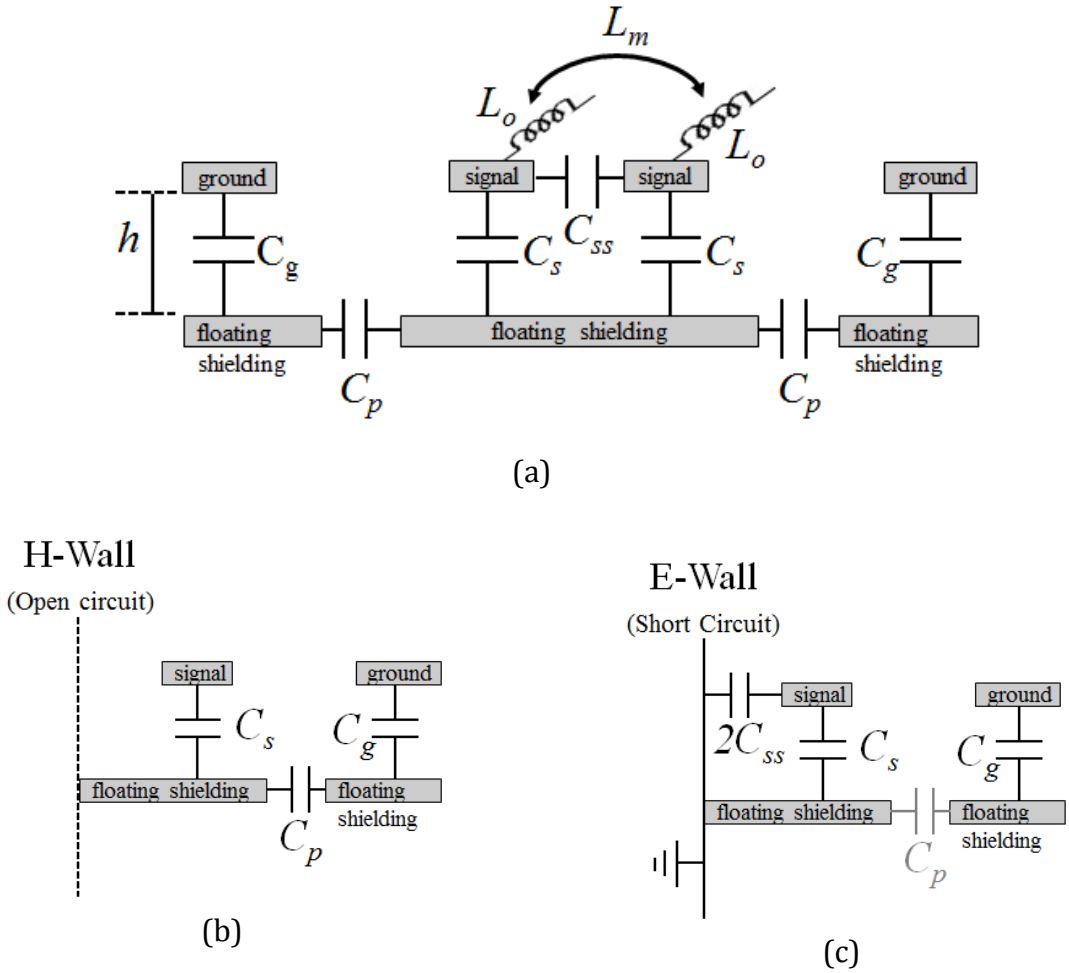

Figure 2-18: CS-CPW with floating shielding cut on the sides (a) Equivalent electrical circuit (b) even-mode and (c) odd-mode.

The magnetic coupling coefficient k_L is the same as in the uncut case in Figure 2-5 (a). On the contrary, the electric coupling coefficient k_C has changed according to equations (2-29) and (2-30).

$$C^{even} = \frac{C_g C_s C_p}{C_p C_g + C_s C_p + C_g C_s} \tag{2-29}$$

$$C^{odd} = 2C_{ss} + C_s \tag{2-30}$$

The resulting k_C:

$$k_C = \left|\frac{C^{even} - C^{odd}}{C^{even} + C^{odd}}\right| = \frac{2C_{ss}\left(C_p C_g + C_p C_s + C_g C_s\right) + C_s^2\left(C_p + C_g\right)}{2C_{ss}\left(C_p C_g + C_p C_s + C_g C_s\right) + C_s^2\left(C_p + C_g\right) + 2C_g C_s C_p} \tag{2-31}$$

In that case, using Figure 2-18 (b) and equation (2-29), it is possible to verify that the equivalent capacitance in the even-mode is a series of three capacitances while in the uncut case it is a series of two capacitances; thus the capacitance in the even-mode for the *CS*-case is lower than in the uncut case. On the other hand, the odd-mode capacitance is similar to the uncut case, which is coherent with equation (2-30). As C^{even} is reduced and C^{odd} remains the same for the *CS*-case, it is expected that k_C reaches very high values.

2.7. Coupling coefficient vs dimensions variation

The various parameters for cut or uncut topologies and the simulation method for coupled slow-wave coplanar waveguides have been explained. We will now show the way for controlling the behavior of this structure. At this point the designer needs to find the relationship between the geometrical dimensions and the electrical characteristics. The coupling coefficient is one of the most relevant parameters for couplers, because it allows the correct design of a pair of coupled lines. This is the reason why, for better understanding and simplicity in the explanations, we present in this section general trends for k_C and k_L only, in a given topology. Next section will focus on more general abacus concerning also Z_C^{even} and Z_C^{odd}.

2.7.1. Variation of coupling coefficients with *W* and *S*

The first case to consider is when the width *W* of the central strips and the distance *S* between them are changed. W_g, *h*, and *G* are fixed to 12 µm, 2.01 µm and 50 µm respectively (See Figure 2-3 for dimensions). The evolution of the electric and magnetic coupling coefficients is presented in Figure 2-19.

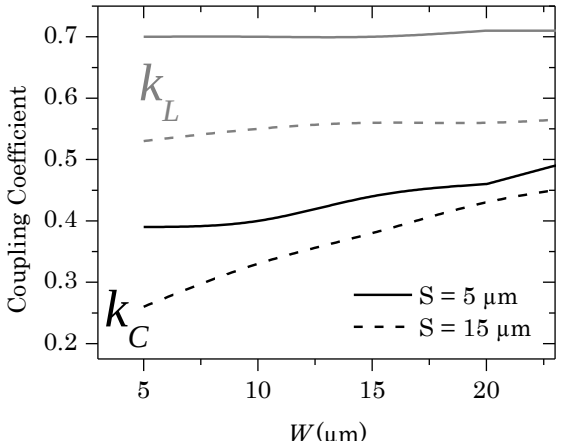

Figure 2-19: Coupling coefficients vs *W* for different *S*

As expected, both coupling coefficients increase when the gap between central strips decreases. On the other hand, when the strips' width increases, the equivalent capacitance also increases. Hence the electric coupling increases as well. In a first approach, both W and S will be considered to control the behavior of the CS-CPW. In sections 2.7.2 and 2.7.3 it is shown how to control one coupling coefficient without inducing any change on the other.

2.7.2. Variation of magnetic coupling with *G*

The distance between the ground and one of the central strips, G (See Figure 2-3), allows the control of the magnetic coupling coefficient without modifying the electric coupling coefficient. For this case W_g, h, and W are fixed to 12 µm, 2.01 µm and 10 µm respectively.

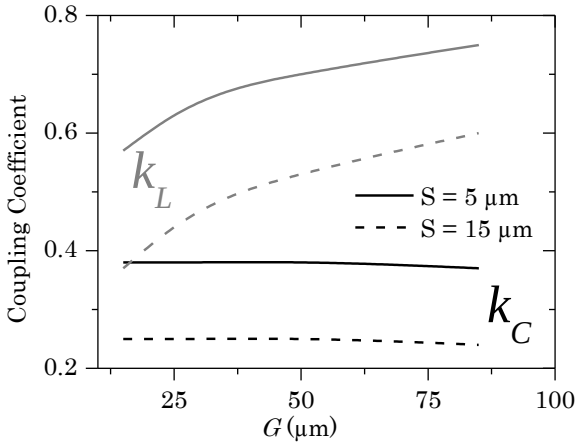

Figure 2-20: Coupling coefficients vs *G* for different *S*

The distance between the lateral ground and the central strip contributes to the magnetic flux, hence the equivalent inductance value. As long as G stays much higher than the height h, the electric field is mainly going through the floating shielding because the shielding is

very close to the CPW strips, thus the electric field is not modified with G. Therefore k_L varies with G without inducing any change on k_C. This first parameter will give us one degree of freedom in the implementation of a CS-CPW.

2.7.3. Cutting the floating ribbons for k_C

An interesting case to consider is when the floating shielding is cut as explained in section 2.6, because it will only affect the electric coupling k_C. To observe this influence, two structures were simulated: in the first one all the floating ribbons were cut in the center and in the second one, the floating ribbons were cut on the sides. Both structures have the same dimensions ($W = 20\ \mu m, G = 50\ \mu m, S = 5\ \mu m$ and $h = 2\ \mu m, W_g = 12\ \mu m$). In Table 2-4 the effects of the different cuts are showed.

TABLE 2-4 COUPLING COEFFICIENTS WHEN CUTTING THE FLOATING RIBBONS

Coupling coefficient	*Cut in center*	*Without any cut*	*Side Cut*
k_C	0.31	0.5	0.77
k_L	0.64	0.64	0.65

The results in Table 2-4 illustrate the concept of cutting the floating shielding. Only the electric coupling k_C is being modified when the shielding is being cut. As explained before in sections 2.6.2 and 2.6.3, the cut in the center *CC* will reduce the mutual capacitance, which according to equation (2-15), it will reduce k_C. The cut on the sides *CS* reduces the self-capacitance, increasing k_C according to equation (2-15) . In all of these cases the magnetic coupling k_L is unmodified.

Hence at this point, the designer has two more degrees of freedom in the implementation of a CS-CPW, *CS* or *CC*.

2.7.4. Effect of the cut width

The idea proposed to vary the electric coupling implies a cut in the floating shielding. In this section the width of this cut is studied. The electric field for different widths of the cut is shown in Figure 2-21.

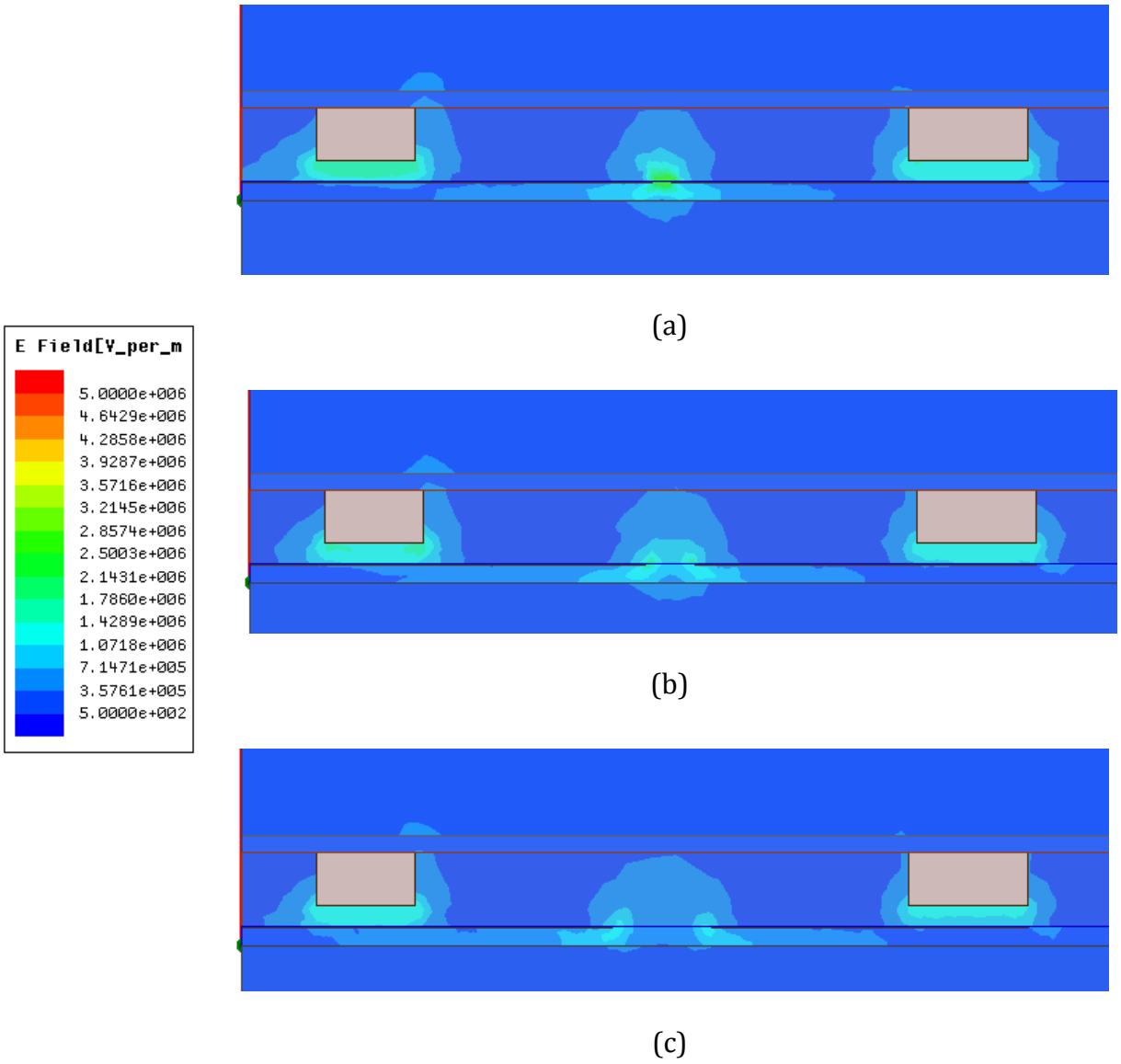

Figure 2-21: Distribution of the electric field for different cut width (a) 2 µm (b) 5 µm and (c) 10 µm

Simulations were carried out for CS-CPW with shielding cut on the side (CS), because it is for this specific case that the parasitic capacitance C_p will have the greatest impact. The results in terms of coupling for different widths are synthetized in Table 2-5. For this simulation $W_g = 12\ \mu m$, $h = 2.01\ \mu m$, $S = 15\ \mu m$, $G = 50\ \mu m$ and $W = 10\ \mu m$.

TABLE 2-5 COUPLING COEFFICENTS FOR DIFFERENT CUT

Cut width	k_C	k_L
2 µm	0.60	0.55
5 µm	0.63	0.55
10 µm	0.66	0.55

From the results, there is evidence that the width of the cut hardly changes the coupling parameters. This change in the coupling is due (as expected) to the parasitic capacitance C_p brought by the cut in the shielding.

From Figure 2-18 (b) and equation (2-29) we can see that C_p is in series with C_s and C_g. When the cut width increases, C^{even} decreases leading to a higher k_C. The cut width might seem as an interesting parameter to control the electric coupling. However, this width will be limited to few micrometers (2 – 5 µm) in order to prevent the possibility of electric field going into the lossy silicon substrate.

2.7.5. Effect of strip spacing *SS* and strip length *SL*

The dimensions of the shielding are briefly studied in this section. Previous works [18] and [19] have studied more deeply the shielding effect. Simulations corresponding to different sizes of the shielding are showed in Table 2-6.

TABLE 2-6 COUPLING COEFFICENTS FOR DIFFERENT *SS* AND *SL*

Dimensions	k_C	k_L
SS = 0.5 µm *SL* = 0.5 µm	0.44	0.71
SS = 0.16 µm *SL* = 0.64 µm	0.44	0.71

From Table 2-6, it is possible to observe that the dimensions of the floating shielding are not modiying the coupling in the structure. In both cases, the electric field is being well confined between the floating ribbons and the CPW strips; meanwhile with these dimensions the magnetic field is not being perturbed and it is still free propagating through the floating shielding.

2.8.Analytical model and abacus

2.8.1. Analytical model

Previous simulation results are in HFSS. In fact, the required time for these sorts of simulations is very long. The time can go from 1-2 hours to even days depending on the configuration. To avoid this inconvenient, an analytical model was created and then implemented on Matlab. In this way, the implemented tool takes then only a few seconds in terms of design.

A parametric predictive electrical model of the CS-CPW is developed at IMEP-LAHC and the principle (for S-CPW) is presented in [20]. This model is realized considering a quasi-TEM mode, which allows the study of electric and magnetic fields separately.

The magnetic field is not perturbed by the presence of the floating shielding, which means that the equivalent inductance of slow-wave CPW is the same as in conventional CPW. The inductance was therefore calculated with the formulation developed in [21].

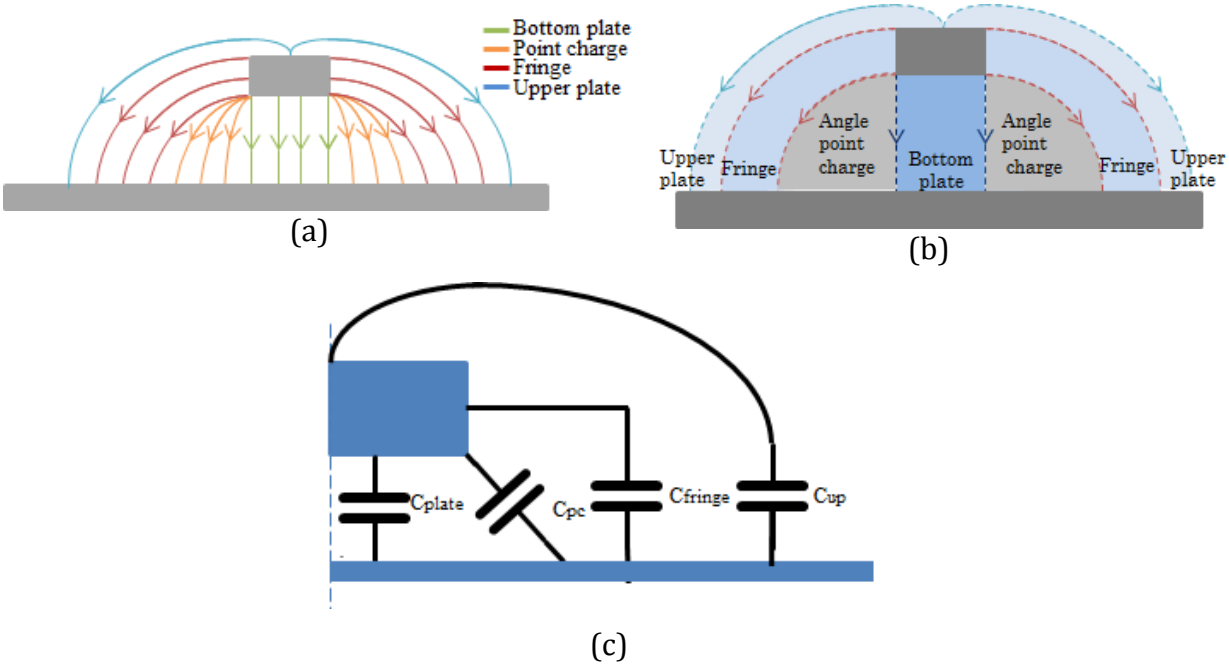

Figure 2-22: Representation of electric field distribution in microstrip in terms of (a) vector fields, (b) regions and (c) equivalent circuit of half-structure

The study here is made mainly over the electric field. For its estimation, the distribution of the electric field is separated into four different regions (bottom plate, angle point charge, finger and upper plate) as shown in Figure 2-22 (a) and (b); leading to the equivalent capacitances in Figure 2-22 (c).

Thanks to these approaches, capacitances and inductances are extracted separately for each even- and odd-mode for signal and ground. Finally to create the complete model for CS-CPW, these parameters extracted from the analytical model are computed with equations from (2-10) to (2-16).

2.8.2. Charts

Charts were constructed, providing an easier and faster solution for designing and optimizing the circuits based on CS-CPW. The model uses the real dimensions and conductivities of the technology provided by ST Microelectronics (B55), but it also can be adapted to any other integrated technology. To show the use of this model, a chart is presented in Figure 2-23. The stack was chosen to present a strong slow-wave effect (increasing the equivalent capacitance while keeping good attenuation). For this reason the floating ribbons were placed in Metal 5 and

then signal and ground in Metal 8-7. Signal and ground strips will be in the thicker layers while the shielding in the thinner layer, which ensures a better quality factor. The resulting distance h is around 2 µm leading to a high equivalent capacitance. The central frequency was chosen in order to test the circuit at very high frequency where other topologies cannot compete.

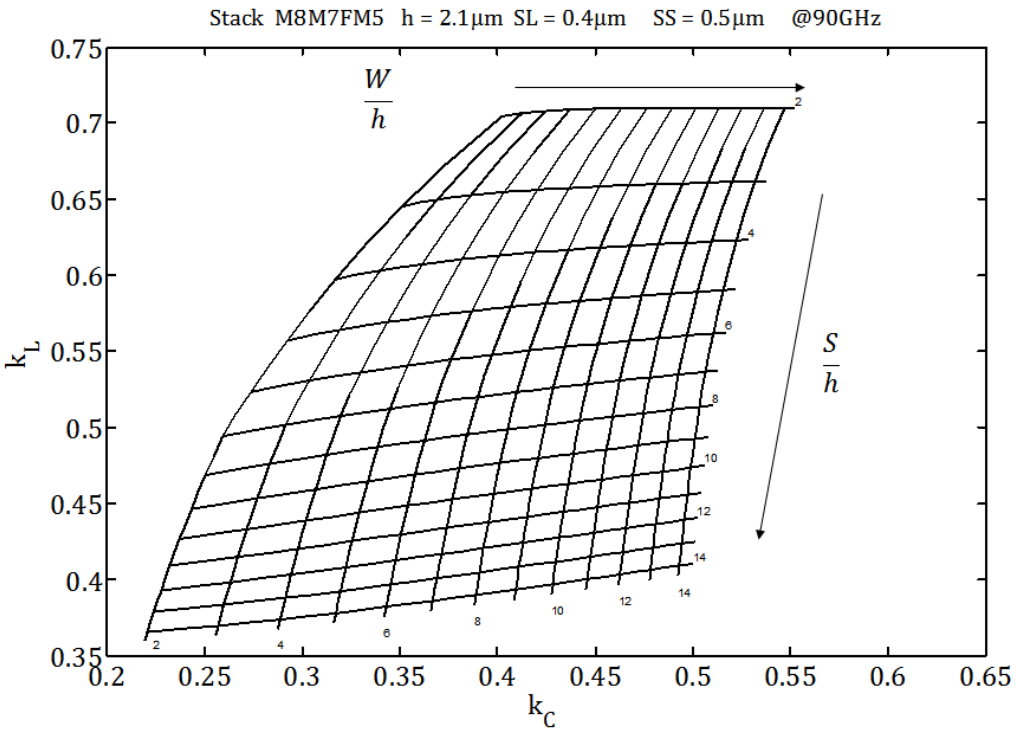

Figure 2-23: Electric coupling and magnetic coefficient design data for CS-CPW.

An example of the chart that can be made with the model is shown in Figure 2-23. Considering the practical case corresponding to $G \gg h$, the capacitance C_{sg} was neglected in the model. The distance G was fixed to 50 µm and W_g to 12 µm for the example presented in Figure 2-23.

2.9.Technological issues

2.9.1. Effect of dummies in CS-CPW

As discussed in Chapter 1, the technology used during this thesis (BiCMOS 55nm by ST Microelectronics) presents 8 metallic layers. However, not all the metallic layers are used in the design of a CS-CPW. Having unused layers forces the addition of metallic "dummies" in the structure in order to validate the DRC[1] requirement. Specifically the "Minimum Density" design rule forces the designer to add little tiny metals in the middle of the structure. We have categorized these dummies in three classes, as presented in Figure 2-24.

[1] DRC : Design Rules Check

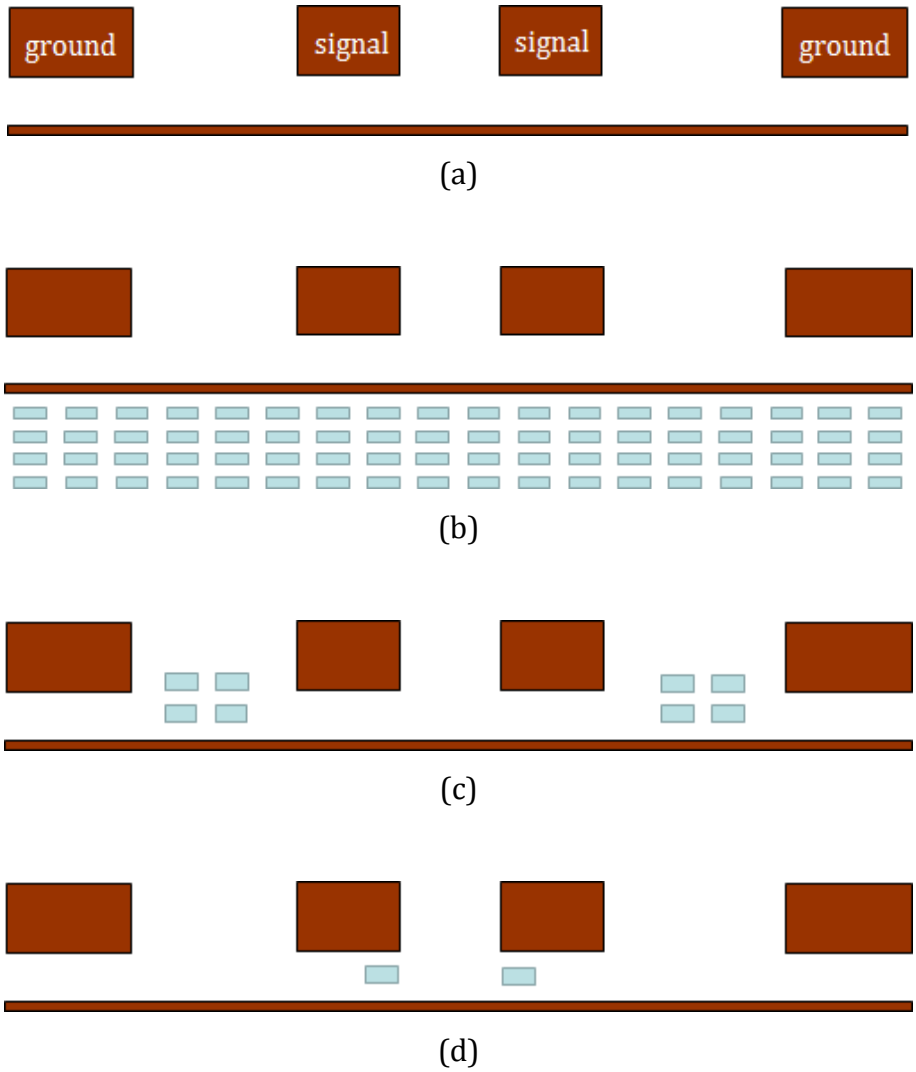

Figure 2-24: Front-view of CS-CPW (a) without any dummies, then divided into three categories. (b) Dummies under the shielding, (c) dummies between CPW ground and signal strips and (d) dummies between CPW signal strip and shielding.

In Figure 2-24 (a) the already discussed CS-CPW structure is represented without the presence of any dummies. Figure 2-24 (b)-(d) present the different zones where dummies must be added.

The first zone of interest is showed in Figure 2-24 (b): dummies are under the floating ribbons. In this case the electric field is not perturbed because it is already confined above the shielding. However, the magnetic field is going through the shielding, therefore eddy currents might be generated on the dummies as well as on the shielding; thus dummies under the shielding must be very small and aligned to the floating ribbons to avoid eddy currents.

The second category is illustrated in Figure 2-24 (c): dummies are between the signal and the ground strips. The electric field could be perturbed by the dummies if they are close to

any of the coplanar strips. Therefore, dummies should be added at a distance around $5h$ to prevent any impact on the electric field. And as for the first category, to avoid perturbation on the magnetic field and eddy currents, dummies must be aligned to the floating ribbons.

Finally the third category is presented in Figure 2-24 (d): dummies are between the signal strip and the floating shielding. In this case the impact of dummies on the electric field is immediate. Capacitance C_S is modified by the presence of dummies, consequently affecting the electric coupling with an observable increase of around 5%. To prevent this, two considerations must be made: 1) the minimum metal (and if possible, none at all) should be added under the signal and 2) this minimum must be previously considered in the design phase.

2.9.2. Dimensions limitations

All technologies present a limit in the width of the thick metals (normally placed in the top layers). In BiCMOS 55nm by ST Microelectronics, a thick metal with a width over 12 µm cannot be sent to fabrication. In this thesis, a simple solution to bypass this limitation is used. It is presented in Figure 2-25.

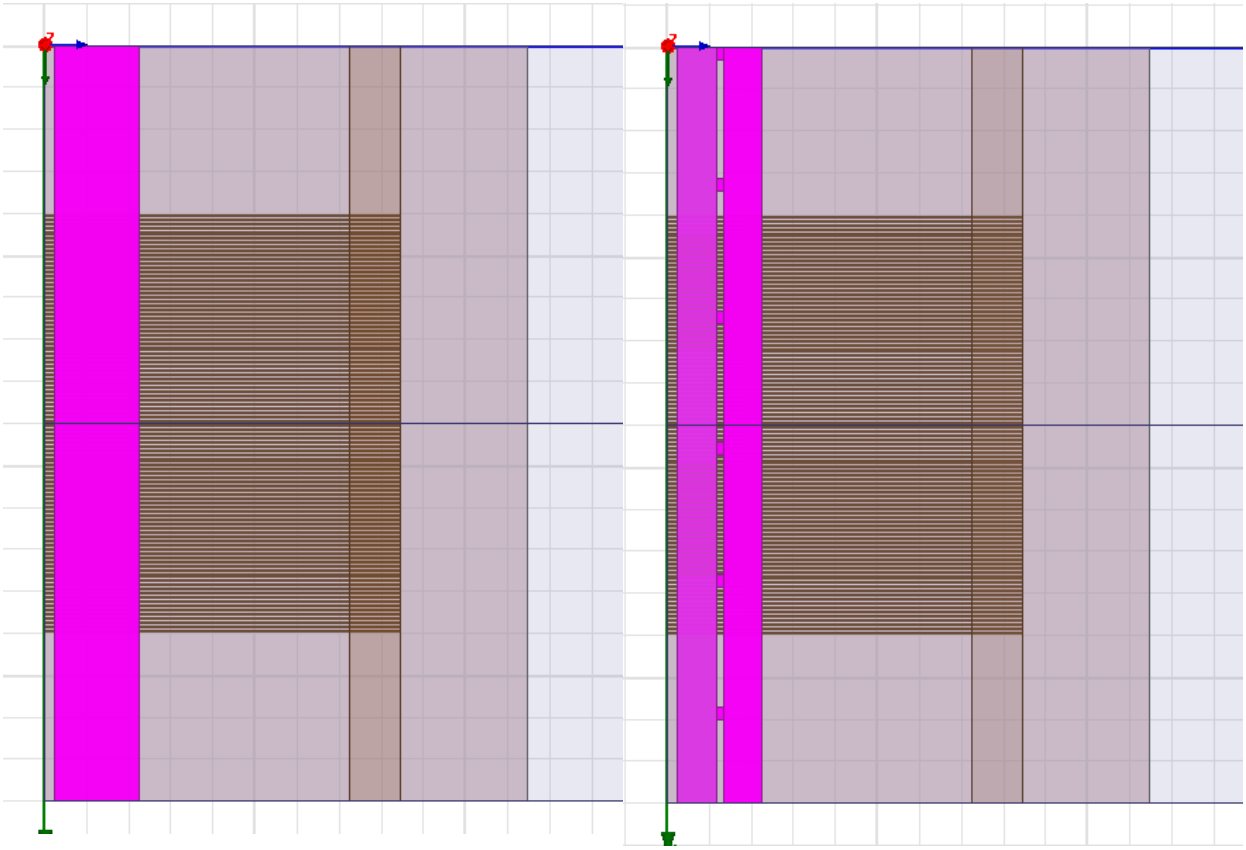

(a) (b)

Figure 2-25: Top view of half CS-CPW structure with (a) complete strip and (b) two parallel central strips connected every 50 µm

Instead of using one single strip as in Figure 2-25 (a), two parallel strips, leading to a width larger than 12 µm, are connected every 50 µm (Figure 2-25 (b)). This concept was simulated and the behavior of the structure was validated. In this way, high widths can be implemented in CMOS technology while respecting the fabrication rules.

2.10. Conclusion

In this chapter, a new concept of integrated coupled lines for mm-wave applications compatible with CMOS technology has been proposed. The concept is based on CS-CPW where the slow-wave effect leads to very interesting characteristics in terms of quality factor and longitudinal length reduction. Electrical models were derived in order to study the evolution of coupling coefficients when varying the geometrical dimensions. The extra degree of freedom offered by S-CPW leads to high-flexibility coupled lines. In particular, it was shown the possibility to control magnetic and electric coupling coefficients independently, contrarily to microstrip lines. Besides, the method described in section 2.5.2 and 2.5.3 was applied to fully describe the behavior of CS-CPW. Table 2-7 summarizes the simulation results for CS-CPW. The results in Table 2-7 are extracted from simulations in HFSS. As for Table 2-3, to observe the impact of one parameter, this was varying while the rest were fixed.

TABLE 2-7 ELECTRICAL CHARACTERISTICS FOR CS-CPW VERSUS DIMENSIONS AND CUTS

Parameter	$S\nearrow$	$W\nearrow$	$G\nearrow$	CS	CC
L_m	↘	↘	↑	⟶	⟶
L_0	↗	↓	↗	⟶	⟶
$k_L = L_m/L_0$	↘	⟶	↗	⟶	⟶
$C^{even} = C_g C_s/(C_g + C_s)$	⟶	↗	⟶	↓	⟶
$C^{odd} = 2C_{ss} + C_s$	↗	↗	⟶	⟶	↓
$\lvert k_C \rvert$	↘	↗	⟶	↗	↘

*↗ or ↘ means moderate variation ↑ or ↓ means faster variation. ⟶ means no variation.

These results will be used to develop high-directivity couplers in the next chapter, with several couplings values, in particular high coupling values greater than 3 dB.

2.11. References

[1] W. Yongle, L. Qiang, L. Sai-Wing, L. Yuanan, X. Quan, "A Novel Planar Impedance-Transforming Tight-Coupling Coupler and Its Applications to Microstrip Baluns," *IEEE Trans. Compon. Packag. Manuf. Technol.,* vol. 4, no. 9, pp. 1480-1488, Sept. 2014.

[2] D. M. Pozar, "Power dividers and Directional Couplers," in *Microwave Engineering*, 4th ed., USA: Wiley, 1998, ch. 7, sec. 6, pp. 337-349.

[3] R. K. Mongia, I. Bahl, and P. Bhartia, "Characteristics of Planar Transmission Lines," in *RF and microwave coupled-line circuits*, 2th ed., USA: Artech House, 2007, Chap. 3.

[4] B. Hur, and W. R. Eisenstadt, "Tunable Broadband MMIC Active Directionnal Coupler," *IEEE Trans. Microw. Theory Techn*., vol. 61, no. 1, pp. 168-176, Jan. 2013.

[5] S. Simion, Marcelli, Romolo, G. Bartolucci, G. Sajin, "Silicon CPW coupled-lines meta-material coupler and on-wafer characterization using a 2-port vector network analyzer," in *Int. Conf. Microw., Radar and Wireless Communications,* 2008.

[6] B. Pan, *et al.* "A broadband surface-micromachined 15-45 GHz microstrip coupler," in *Int. Microw. Symp. Dig.*, 2005.

[7] B. M. Oliver, "Directional electromagnetic couplers," in *Inst. Radio Eng. (IRE)*, vol. 42, no. 11, pp. 1686–1692, 1954.

[8] Y.-H. Chun, J.-Y. Moon, S.-W. Yun, J.-K. Rhee, "Microstrip line directional couplers with high directivity," in *Electron. Lett.*, vol. 40, no. 5, pp. 317-318, Mar. 2004.

[9] J.-Y. Shen, *et al.*, "High-directivity single- and dual-band directional couplers based on substrate integrated coaxial line technology," in *Int. Microw. Symp. Dig.*, 2013.

[10] R.-X. Wu, J. Xin-yi, R.-F. Chen, Y. Poo, "A novel microstrip coupler with EBG structures," in *Asia-Pacific Microw. Conf. Proceedings*, 2008.

[11] J. Lugo-Alvarez, A. Bautista, F. Podevin, P. Ferrari, "High-directivity compact slow-wave CoPlanar waveguide couplers for millimeter-wave applications," in *European Microw.Conference,* Rome, Italy, 2014.

[12] J. Reed, G.J. Wheeler, "A Method of Analysis of Symmetrical Four-Port Networks," *IEEE Trans. Microw. Theory Techn*., vol. 4, no. 4, pp. 246-252, Oct. 1956.

[13] K.C. Gupta, R. Garg, and I.J. Bahl, "Microstrip Lines and Slot Lines," USA: Artcech House, Dedham, MA, 1979.

[14] T.S.D. Cheung, *et al.*, "On-chip interconnect for mm-wave applications using an all-copper technology and wavelength reduction," in *IEEE Int. Solid-State Circuits Conf. Dig. of Technical Papers,* 2003.

[15] D.W. Kammler, "Calculation of Characteristic Admittances and Coupling Coefficients for Strip Transmission Lines," *IEEE Trans. Microw. Theory Techn*., vol. 16, no. 11, pp. 925-937, Nov. 1968.

[16] Ansys, HFSS [Online], Available: http://www.ansys.com

[17] Keysight, Advanced Design Symtem, Available: http://www.keysight.com/en/pc-1297113/advanced-design-system-ads

[18] A-L. Franc, "Lignes de propagation intégrées à fort facteur de qualité en technologie CMOS – Application à la synthèse de circuits passifs millimétriques," Ph.D. dissertation, Université de Grenoble-Alpes, 6 Jul., 2011.

[19] X. Tang, "Apport des lignes à ondes lentes S-CPW aux performances d'un front-end millimétrique en technologie CMOS avancée," Ph.D. dissertation, Université de Grenoble-Alpes, 8 Oct. , 2012.

[20] Bautista, A.; Franc A.-L.; Ferrari, P.; "An Accurate Parametric Electrical Model for Slow-wave CPW," in *Int. Microw. Symp.,* Phoenix, USA, 2015.

[21] W. Heinrich, "Quasi-TEM description of MMIC coplanar lines including conductor-loss effects," *IEEE Trans. Microw. Theory Techn*., vol. 41, no. 1, pp. 45-52, Jan. 1993.

Chapter 3

Millimeter-Waves CS-CPW High-Directivity Directional Couplers

3.1.Introduction

As previously stated, coupled line directional couplers coupled lines are extremely important in many mm-wave applications. Currently, the only way available to develop coupled line couplers in CMOS technologies is based on microstrip lines. However, microstrip lines couplers suffer from many drawbacks:

- Inhomogeneity of the medium, leading to lower directivity because of the difference of the phase velocity of each mode.
- High coupling (i.e. above 3 dB) requires very narrow gaps between the coupled strips; which are incompatible with advanced CMOS/BiCMOS fabrication processes for edge-coupled structures. As explained in Chapter 1, this issue is overcome by arranging microstrip in broadside-coupled configuration [3]-[5].
- Longer length needed for microstrip lines, increasing prices in the design.

Many works were carried out at RF frequencies in PCB technology, in order to face the problem of inhomogeneous substrate. For instance, capacitances were added to artificially increase the electric coupling coefficient in order to equalize with the magnetic field [1]. Defected ground structures (DGS) were also used for the same purpose [7]; as well as the

insertion of metallic cylinders [8] or the use of slot technique on planar microstrip [9]. However, these concepts cannot be implemented when dealing with CMOS technologies and mm-wave frequencies. In the same manner, the use of DGS would lead to a significant increase of the insertion loss due to low bulk resistivity (few Ω.cm).

In Chapter 1, the current solutions and their tradeoff are presented. Also, a review of the classical theory about directional coupler is already made in Chapter 1. In this chapter an alternative approach for directional couplers in CMOS is proposed. First, the methodology to design couplers based on CS-CPW is presented as well as some examples developed with this concept. Next, a comparison of a coupler implemented with C-µstrip and with CS-CPW is showed. And finally a discussion about the deembedding challenge and the measurements is done.

3.2. Design method with CS-CPW

Similarly to any integrated passive device, two types of transmission lines give the point to address high performance integrated couplers: coupled microstrip lines (C-µstrip) and coupled slow wave coplanar waveguides (CS-CPW). However, C-µstrip suffers from many drawbacks. This has already been discussed in detail in chapter 1.

By reminding section 2.7.3 in chapter 2, CS-CPW theoretically offer the opportunity to vary the electric coupling from 0 to 1, without modifying the magnetic coupling. In this section, the design method developed during this thesis is presented.

3.2.1. Principle

The designer of a coupler using CS-CPW has six parameters (*G*, *S*, *W*, *L*, cut at the center *CC* and cut on the sides *CS*) to obtain the desired coupling. Parameters are showed in Figure 3-1 and Figure 3-2.

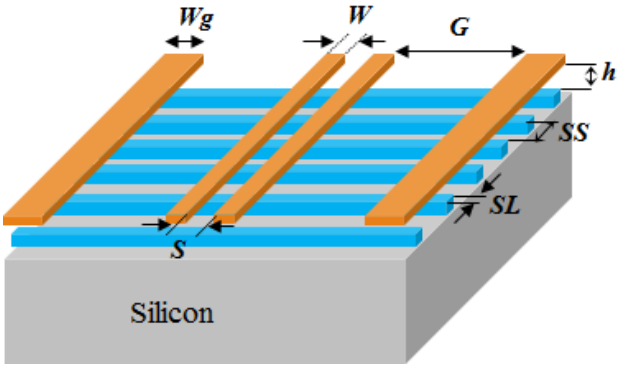

Figure 3-1: CS-CPW structure with nomination of the dimensions.

The maximum directivity is reached when $k_L = k_C = k$. Since the magnetic coupling is not affected when cutting the floating ribbons, the designer can first choose the dimensions of G, W and S, compatible with the technology, in order to reach the targeted k_L which should be the same as the targeted k.

The next step consists in setting k_C at the same value as k_L. As discussed in Chapter 2, the electric coupling varies when the floating shielding is cut while the magnetic coupling stays unperturbed. It is shown by simulations in section 2.7.3 that a cut in the center (CC) reduces k_C, while a cut on the sides (CS) increases k_C. Consequently with a combination of floating ribbons (CC and CS) it is possible to choose any value for k_C. This is achieved by choosing the number of center cut and sides cut ribbons, i.e. the number of CC- and CS-ribbons, as described in Figure 3-2.

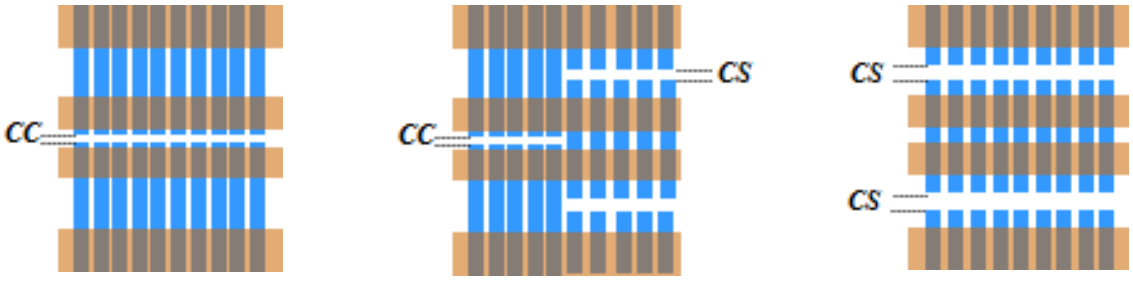

Figure 3-2: Top-view of CS-CPW structure with (a) only *CC*-ribbons, (b) Mix of *CC- and CS*-ribbons and (c) only *CS*-ribbons.

The design procedure consists therefore in optimizing the density of CS-ribbons over the total number of ribbons (CS- and CC-). As an example, Figure 3-3 shows CS-CPW as a succession of N repetitive elementary cells with a density of CS-ribbons of 90 % (1 CC-ribbon for 9 CS-ribbons).

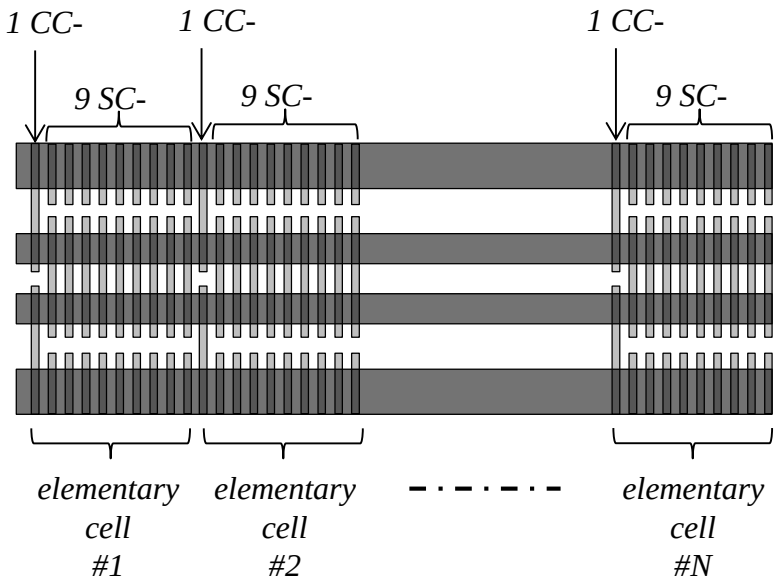

Figure 3-3: Top-view of CS-CPW when 1 floating ribbon is cut in the center *CC* and 9 are cut at the sides *CS*. The elementary pattern is repeated N times. The density of *SC*-ribbon is 90%.

The procedure presented above allows the design of a directional coupler with any desired coupling while keeping at the same time a very high directivity.

3.2.2. Example

In [13], the proposed method has been applied to design two directional couplers having weak coupling ($k = 0.16, C = 16$ dB) and strong coupling ($k = 0.7, C = 3$ dB), respectively, for a proof-of-concept, in BiCMOS 55 nm technology from STMicroelectronics. The CPW strips were stacked in the thick metallic layers from M8 to M7 and the floating shield ribbons lay in the thinner layer below M5. Figure 3-4 represents the magnetic and electric coupling coefficients as a function of the *CS*-ribbons density. In both cases the geometrical dimensions (W, G, S, W_g, SS and SL) are fixed and only the density of *CS*-ribbons is changing. For Figure 3-4 (a): $W = 20$ µm, $G = 55$ µm, $S = 5$ µm, $W_g = 12$µm $SS = SL = 0.5$ µm. For Figure 3-4 (b): $W = 20$ µm, $G = 20$ µm, $S = 25$ µm, $W_g = 12$µm, $SS = SL = 0.5$ µm.

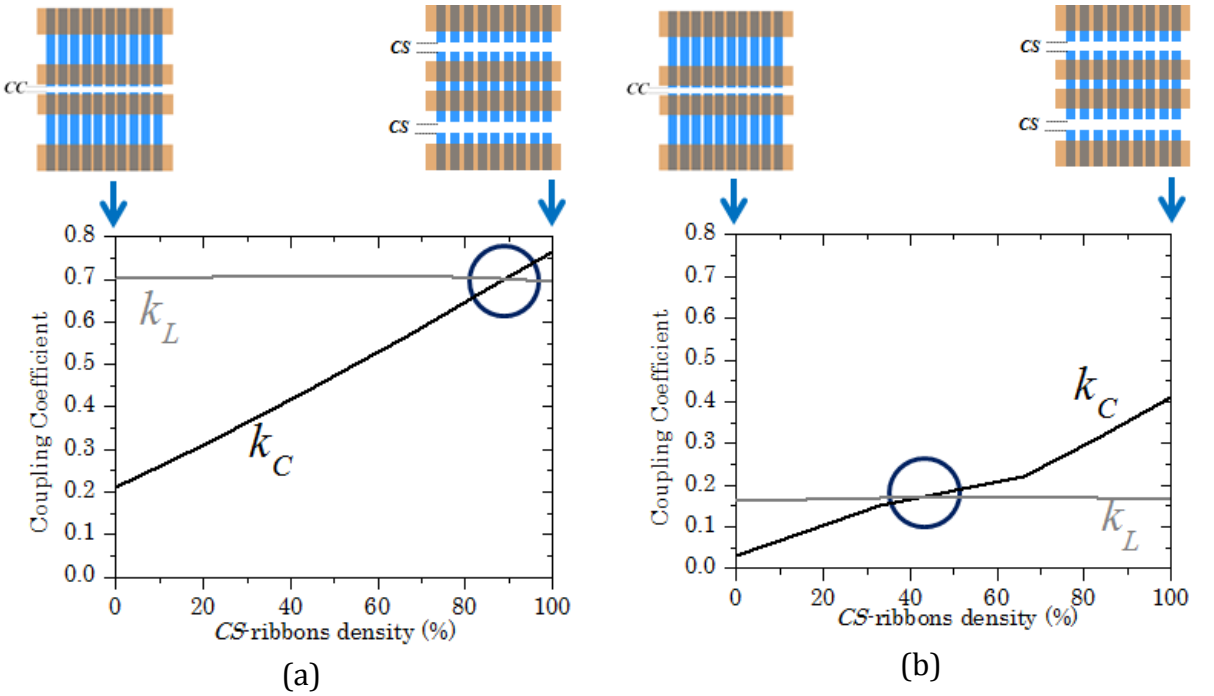

Figure 3-4: Coupling coefficients for two proof-of concept couplers. (a) $k = 0.7$, (b) $k = 0.16$.

As shown in Figure 3-4, k_L is not affected by the shielding ribbons, as predicted by the theory, and $|k_C|$ increases with the *CS*-ribbons density. A specific density enables to equalize $k = k_L = |k_C| = 0.7$ (Figure 3-4 (a)) and $k = k_L = |k_C| = 0.16$ (Figure 3-4 (b)). Figure 3-4 results give a validation of the design concept. At this point, this thesis offers a novel method to implement high directivity couplers at mm-waves. Figure 3-4 shows to the designer the possibility to reach any coupling coefficient when using CS-CPW. In the next section, mm-wave couplers are designed based on this concept.

3.3.Practical couplers design

In this section, the design as well as the practical issues of two different directional couplers are presented. The first coupler (3 dB coupling) is designed as a proof-of-concept; the idea is to validate the design procedure with CS-CPW at 50 GHz. The second coupler (18 dB coupling) is designed because it was required for a specific on-wafer measurement system at working at 150 GHz.

3.3.1. 3 dB coupler at 50 GHz

The central frequency of this coupler was basically chosen because it could be measured with the equipment in the laboratory. The goal was to show that a high coupling coupler could be implemented with the CS-CPW, being a solution to the struggle for integrating high coupling couplers at high frequency with the advanced CMOS/BiCMOS technologies. Due to the many applications demanding this kind of circuit, a 3 dB coupling was the target for this coupler. The procedure described in section 3.2 to design a coupler with CS-CPW was used. The results of the

simulated coupler as well as its layout are presented in Figure 3-5. The parameters for this structure are: $W = 20$ µm, $G = 55$ µm, $S = 5$ µm, $W_g = 12$µm $SS = SL =$ 0.5 µm and the entire floating shielding is cute on the sides *CS*.

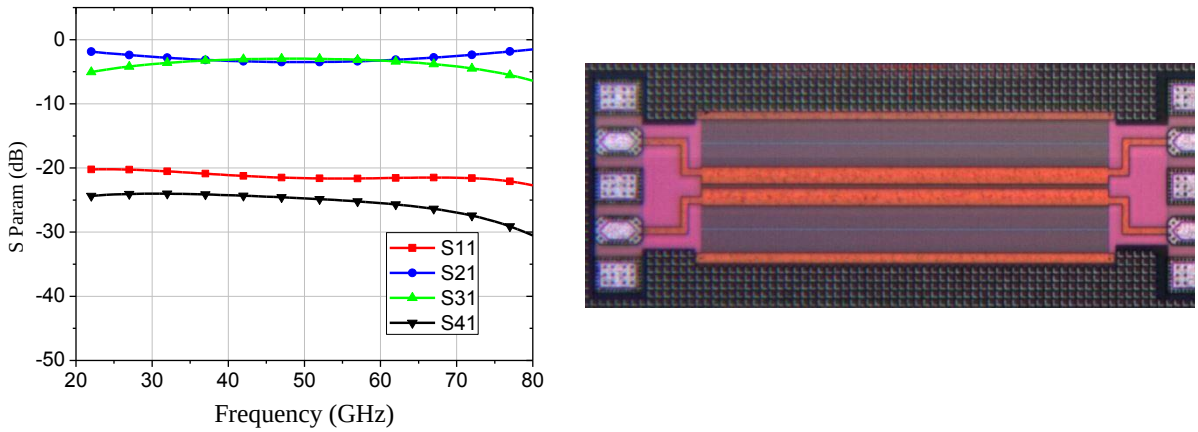

Figure 3-5: (a) S-Parameters and (b) photograph of the 3-dB coupler fabricated at 50 GHz.

From Figure 3-5 (a), it can be seen that the coupler has 22 dB of directivity, a 3 dB coupling and a good matching over a wide bandwidth from 35 GHz to 65 GHz. The length of the coupler is 478 µm. The coupler being a 4-ports device, the de-embedding procedure is a bit tricky. It is described in section 3.5.

3.3.2. 18 dB coupling at 150 GHz

The major interest of studying new topologies for directional couplers concerns frequencies beyond 100 GHz. Hence it was important to demonstrate that the CS-CPW concept still works at such frequencies. The frequency of 150 GHz was fixed in order to address a specific project in the IMEP-LAHC laboratory, linked to the realization of an on-wafer measurement system around 150 GHz.

3.3.2.1. Design

The technical specifications for this coupler were: good matching, low coupling and very high directivity. Figure 3-6 presents the scattering parameters of the simulated coupler. The parameters for this structure are: $W = 10$ µm, $G = 15$ µm, $S = 25$ µm, $W_g = 12$µm, $SS = SL =$ 0.5 µm and all the floating shielding is cut in the center *CC*.

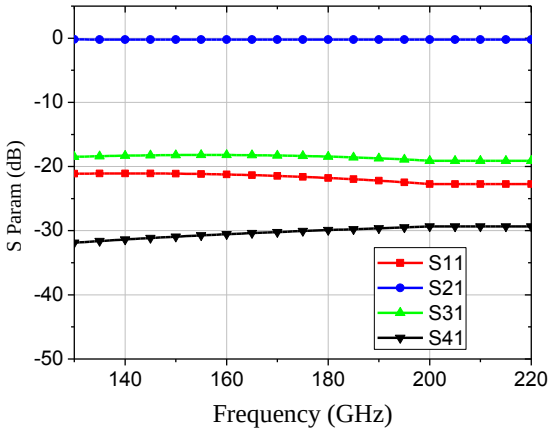

Figure 3-6: S-Parameters of the 18 dB coupler designed at 150 GHz.

A directional coupler with very low coupling and high directivity, as the one required for the system at 150 GHz, implies that the isolation of the coupler should be even lower than coupling. This creates a trade-off between the isolation and the coupling, because very low isolation is difficult to reach in real cases due to fabrication process. For this reason, the coupler designed presents 18-dB coupling and a directivity of 12 dB. This was the best trade-off for the system's requirements.

3.3.2.2. Practical issues

This coupler is designed at very high frequency (at 150 GHz). The dimensions are not an issue in the fabrication process. However, measurements of a four-port network at 150 GHz are not simple because of limitations due to the available measurement systems. Currently there are no four-ports VNA at 150 GHz; therefore a way for measuring the coupler at very high frequency with a 2-port VNA is proposed. The measurement protocol is presented in Figure 3-7.

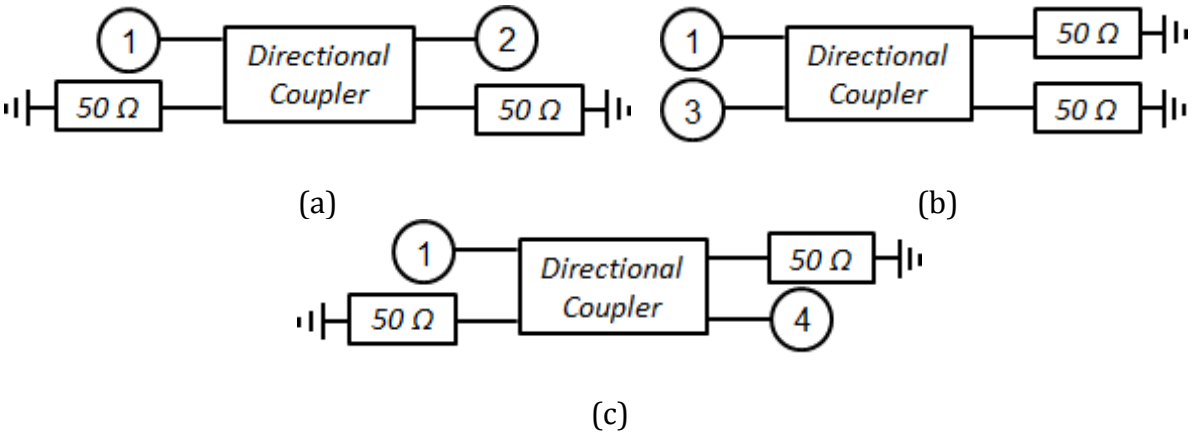

Figure 3-7: Procedure proposed to measure the directional coupler parameters at 150 GHz. (a) Port 1 and Port 2 of the coupler are connected to the VNA, Port 3 et Port 4 charged by 50 Ω, measurement of insertion losses and matching. (b) Port 1 and Port 3 of the coupler are connected to the VNA, Port 2 et Port 4 charged by 50 Ω, measurement of the coupling. (c) Port 1 and Port 4 of the coupler are connected to the VNA, Port 2 et Port 3 charged by 50 Ω, measurement of the isolation.

As shown in Figure 3-7, two ports of the coupler are connected to the VNA while the remaining two are loaded by a 50 Ω load. Three measurements are necessary to extract all the coupler's S-parameters: return loss and insertion loss (Figure 3-7 (a)), coupling (Figure 3-7 (b)) and isolation (Figure 3-7 (d)).

3.3.2.3. Active load

As shown in the previous section, a 50-Ω load is needed in order to measure all the S-parameters of the directional coupler at 150 GHz. Since resistances available in the Front-End-Of-Line are not consistent at 150 GHz, an active load was developed in ST Microelectronics for this purpose. The principle consists in using the R_{ON} resistance of a CMOS transistor. The value of the resistance will be then controlled by a DC voltage (Vdd). The schematic of the active load is presented in Figure 3-8.

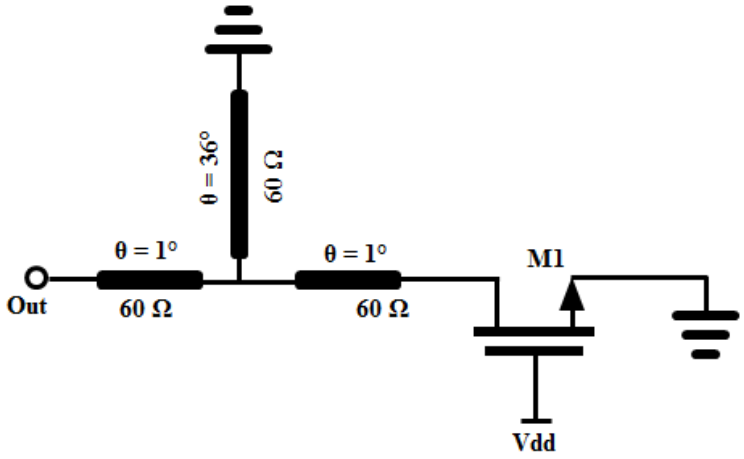

Figure 3-8: Schematic of the active load.

In order to cancel the imaginary part, a stub ended by a short-circuit is implemented. The simulation of the return loss of the load is shown in Figure 3-9.

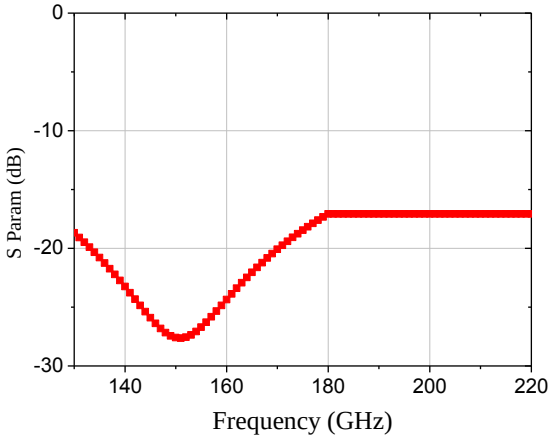

Figure 3-9: Return loss of the active load.

From Figure 3-9 we can see that this solution presents a good matching through the entire frequency band.

3.3.2.4. 2-port measurement setup: simulations

The measurement method at 150 GHz has been explained in the previous sections. The measurement protocol mentioned in section 3.3.2.2 and illustrated in Figure 3-7 is simulated with the load introduced in section 3.3.2.3. Results are presented in Figure 3-10.

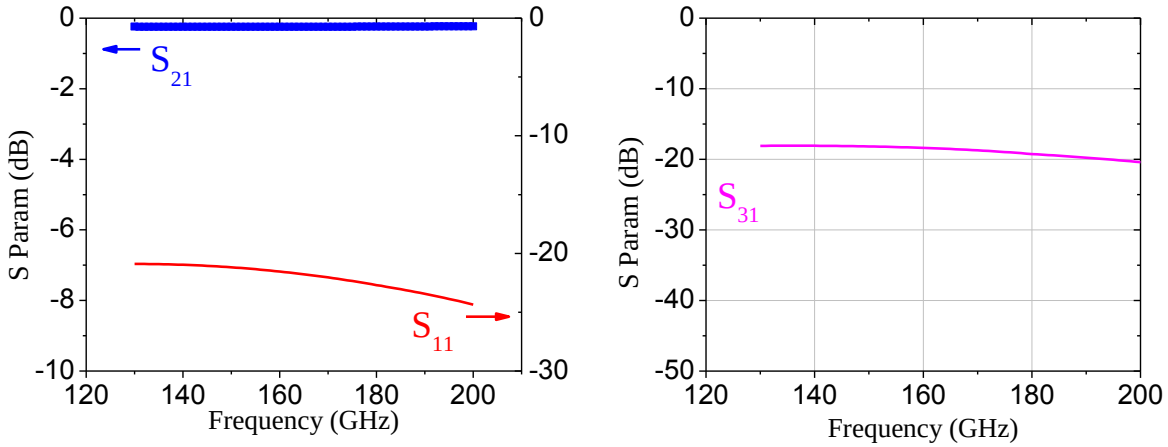

(a) (b)

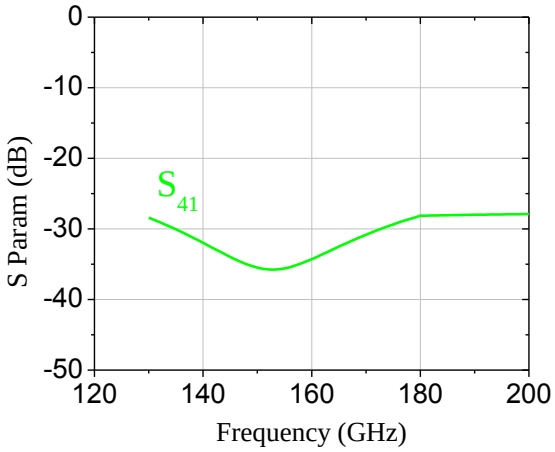

(c)

Figure 3-10: Simulation results. (a) Return loss and insertion loss. (b) Coupling and (c) Isolation.

Figure 3-10 presents the resulting S-parameters when two ports of the directional coupler are loaded with the active load. Return loss (Figure 3-10 (a)), insertion loss (Figure 3-10 (a)), coupling (Figure 3-10 (b)) and isolation (Figure 3-10 (c)) are extracted. The limited bandwidth of the load is affecting mainly the isolation measurement (Figure 3-10 (c)) since it is the lowest-magnitude S-parameter.

3.4. Comparison of CS-CPW with C-µstrip directional couplers

In [13], the performance of a coupler based on CS-CPW is compared to a coupler carried out with C-µstrip in the same BiCMOS 55 nm technology, see Table 2-1.

TABLE 3-1 CS-CPW COUPLERS COMPARED TO C-USTRIP COUPLERS. RESULTS @60GHZ

Parameter	Weak coupling		Strong coupling	
	S CPW $k = 0.16$ $C = 16\ dB$	*µstrip* $k = 0.16$ $C = 16\ dB$	*S CPW* $k = 0.7$ $C = 3\ dB$	*µstrip* $k_{max} = 0.28$ $C_{max} = 11\ dB$
$S_{11}\ (dB)$	-20.7	-24.3	-29	-25.5
$S_{21}\ (dB)$	-0.4	-0.8	-3.3	-1.05
$S_{31}\ (dB)$	-17	-16.4	-3.5	-11.7
$S_{41}\ (dB)$	-33.25	-28.9	-28.6	-33.6
Dir. (dB)	**16.25**	**12.5**	**25.1**	**21.9**
Length (µm)	**540**	**710**	**388**	**753**
S (µm)	15	8.9	5	5
W (µm)	20	8	25	6

Layout rules (minimum gap between the coupled strips) limit the highest coupling achievable with the C-µstrip to 11 dB, whereas 3 dB coupling can be reached with CS-CPWs couplers. The directivity (see Table 2-1) is better for the CS-CPW. Finally, thanks to the slow-wave effect, the length reduction of the CS-CPW couplers is at least 37 % compared to their

microstrip counterpart. Another interesting parameter already mentioned above is the highest directivity achieved with CS-CPW couplers, as shown in see Figure 3-11.

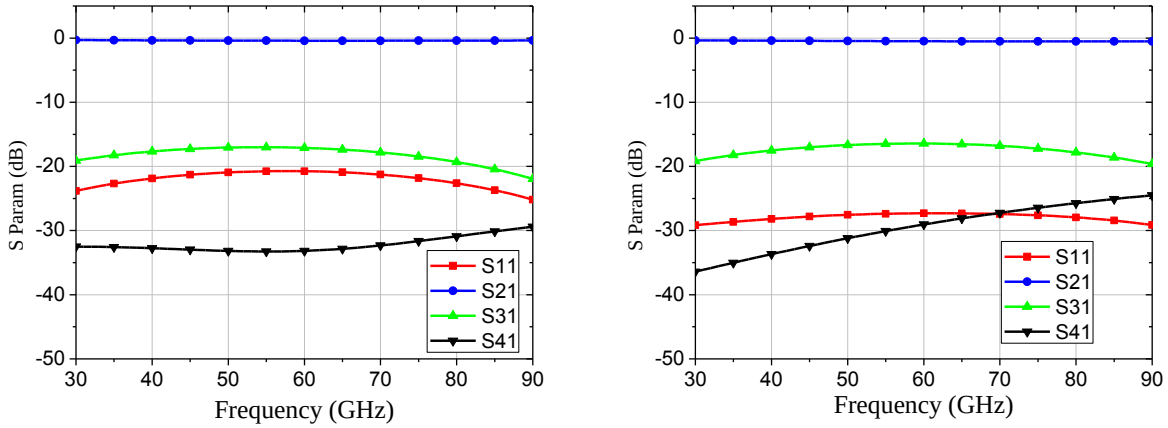

Figure 3-11: S-Parameters for a directional coupler implemented with (a) CS-CPW and (b) C-µstrip

A high directivity can be obtained over more than one octave, with isolation below -30 dB. This is not the case with the C-µstrip couplers, for which the directivity is much lower.

3.5. Multimode TRL de-embedding method

To de-embed the 4-port directional coupler at high frequency, a Multimode TRL calibration technique was used. The de-embedding technique is presented in [14]. A comprehensive analytical derivation of the multimode thru-reflect-line (TRL) calibration algorithm is given. This technique is based on the new generalized reverse cascade matrix formulation, which is very practical because it can account for some symmetries in the measurement setup and reflect them in the symmetry of the derived relationships [14]. Besides, this technique presents interesting advantages:

- It enables zero- and nonzero-length thru standards;
- It can be extended for networks with higher number of modes;
- It is very efficient by the use of symmetry in the error networks reducing the need of a reflect standard.

The general formulation is fully detailed in [14], here only the equations needed for our case are presented.

A measurement with a VNA is the result of the product of three matrices:

$$M_x = AN_x\overline{B} \tag{3-1}$$

where N_x is the generalized cascade matrix of the measured device-under-test (DUT) and A and B are nonsingular generalized cascade matrices that describe the networks used to realize the connection between the on-wafer reference plane and the VNA. Figure 3-12 illustrates the the measurement principle.

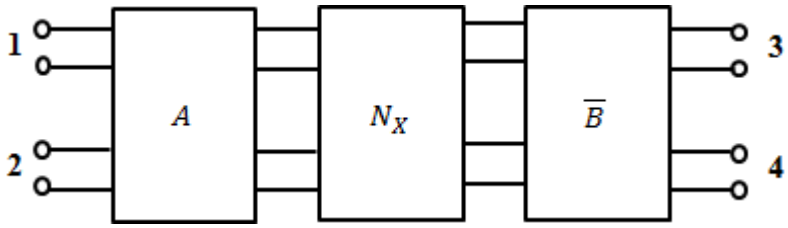

Figure 3-12: Block diagram of the measurement of a DUT represented by matrix $N_x$with a VNA, and the embedding networks A and $\overline{B}$.

From equation (3-1), N_x can be derived:

$$N_x = A^{-1}M_x\overline{B}^{-1} \tag{3-2}$$

The principle of the method is thus to identify matrices A and B to finally being able to calculate N_x. To do this, two extra measurements must be done. Thru- and Line-standard measurements are therefore required to obtain A and B. The block diagram of the thru-measurement is presented in Figure 3-13.

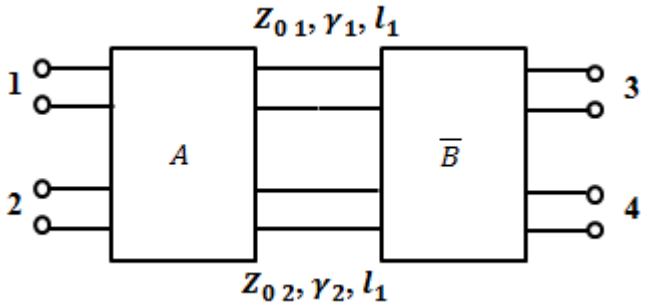

Figure 3-13: Schematic of the thru measurement.

Thru-standard measurement (Figure 3-13) is represented by matrix M_1. It gives:

$$M_1 = AN_1\overline{B} \tag{3-3}$$

where N_1 is the generalized cascade matrix of the thru-standard. The line-standard must be measured by the same manner (Figure 3-14).

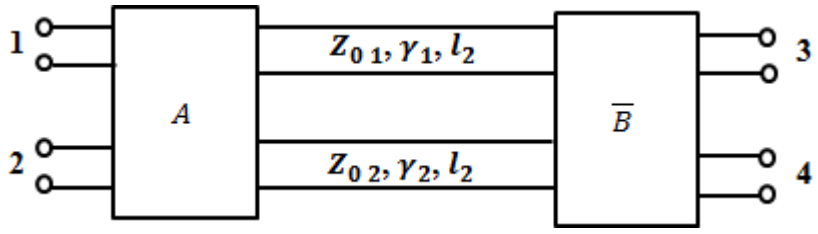

Figure 3-14: Schematic of the line measurement.

Line-standard measurement is presented in matrix M_2:

$$M_2 = AN_2\overline{B} \tag{3-4}$$

where N_2 is the generalized cascade matrix of the line-standard. From these two measurements, matrix Q can be calculated:

$$Q = M_2 M_1^{-1} \tag{3-5}$$

Then eigenvectors are derived from Q:

$$Y_0 \Lambda = QY \tag{3-6}$$

Eigenvectors Y_0 will be named as A_0:

$$A_0 = Y_0 \tag{3-7}$$

From which matrix B_0 is computed:

$$B_0 = \overline{Y_0^{-1} M_1 \widetilde{N_1}} \tag{3-8}$$

A_0 is a 4x4 elements matrix:

$$A_0 = \begin{bmatrix} A_{0\,11} & A_{0\,12} & A_{0\,13} & A_{0\,14} \\ A_{0\,21} & A_{0\,22} & A_{0\,23} & A_{0\,24} \\ A_{0\,31} & A_{0\,32} & A_{0\,33} & A_{0\,34} \\ A_{0\,41} & A_{0\,42} & A_{0\,43} & A_{0\,44} \end{bmatrix} \tag{3-9}$$

Matrices A_0 and B_0 can be written with sub-matrices:

$$A_0 = \begin{bmatrix} A_{0\,11} & A_{0\,12} \\ A_{0\,21} & A_{0\,22} \end{bmatrix} \tag{3-10}$$

$$B_0 = \begin{bmatrix} B_{0\,11} & B_{0\,12} \\ B_{0\,21} & B_{0\,22} \end{bmatrix} \tag{3-11}$$

From sub-matrices $A_{0\,22}$ and $B_{0\,22}$, L is calculated:

$$L = A_{0\,22}^{-1} B_{0\,22} \tag{3-12}$$

From which matrix K_0 is then computed:

$$K_0 = \begin{bmatrix} I & 0 \\ 0 & L \end{bmatrix} \tag{3-13}$$

With these terms, matrix N_{x0} is extracted:

$$N_{x0} = K_0^{-1} A_0^{-1} M_x \widetilde{B_0} K_0 \tag{3-14}$$

Finally the matrix N_{x0} is the de-embedded matrix of the DUT. Before being named as N_x, it should be de-normalized with the impedance of the line-standard and then re-normalized to 50 Ω. The resulting matrix of the re-normalization is the desired matrix N_x. This is the method used in the case of the measurement of the CS-CPW. As the circuits that will be implemented to measure the CS-CPW will present symmetry, there is no need of a reflect-standard.

3.6. Measurement results

The measurements of the directional couplers previously presented in section 4.4 are presented in this section. The first coupler (4-ports device at 50 GHz) will be measured in IMEP-LAHC laboratory in November; the measurement results will be presented during the dissertation of this thesis. The second coupler (2-ports device at 150 GHz) was measured in IEMN laboratory and the results are presented below.

3.6.1. 18-dB coupling at 150 GHz

The coupler was implemented and measured in stand-alone in a VNA (ref=ZVA24 ROHDE/SCHAWARZ) from 140 to 220 GHz. The RF probes used to measure were the Picopobre (ref 220-GSG-50-BT-W-M). Figure 3-15 shows a picture of the layout of the fabricated coupler for the measurement of the S_{11} and S_{21} parameters.

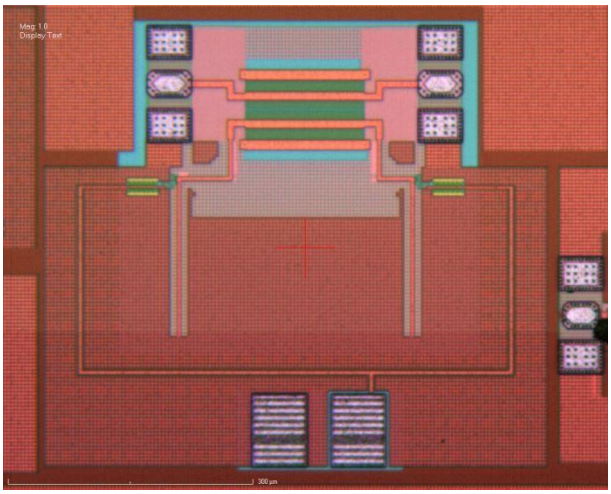

Figure 3-15: Photograph of the coupler measured at 150GHz.

Port 1 and port 2 of the coupler are connected to the VNA which will allow to measure the return loss and the insertion loss. The same manipulation was made to measure coupling and isolation. Measurement results are given in Figure 3-16.

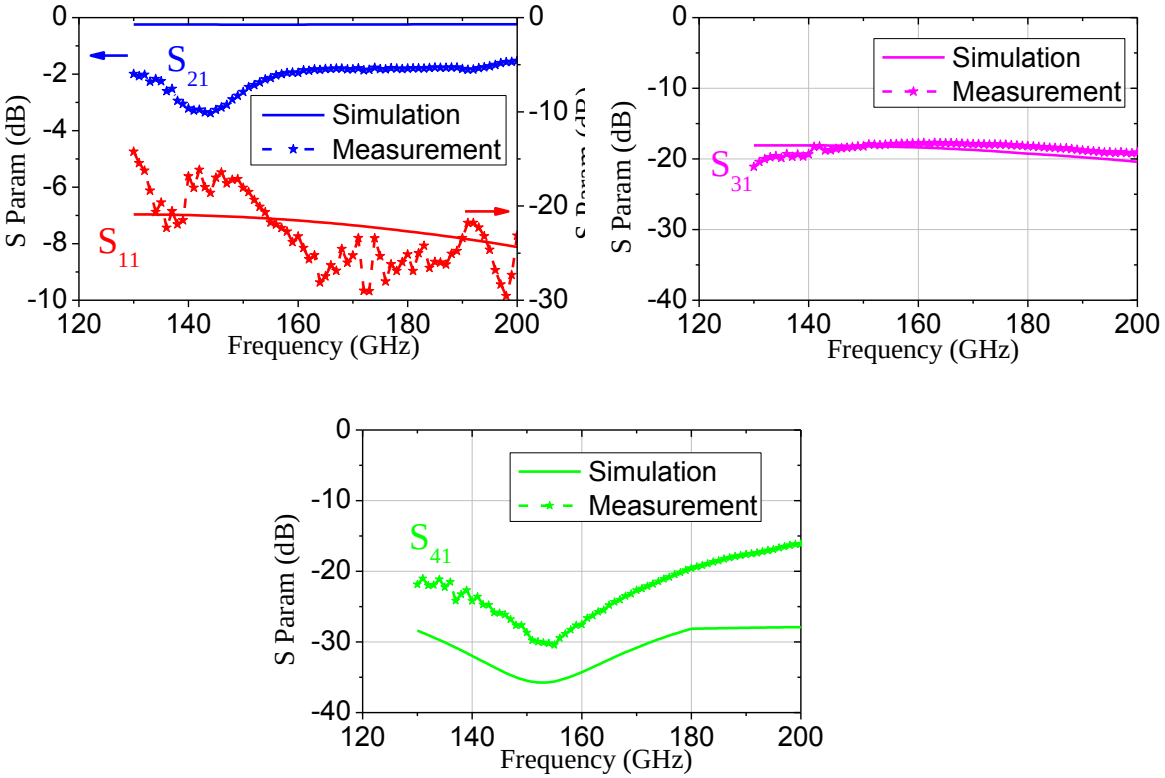

Figure 3-16: Simulation vs Measurements results. (a) Return loss and insertion loss. (b) Coupling and (c) Isolation.

The measurement results in Figure 3-16 were de-embedded so that they can be compared to the simulations. Return loss is better than 20 dB. Coupling is around 18 dB as simulated; it is almost flat through the entire bandwidth. 12-dB of directivity is reached at 150 GHz. These overall results permit to validate the concept of CS-CPW in the studied frequency band (140 – 200 GHz) for directional couplers.

3.7. Discussion

This chapter proposes a new concept of integrated coupled lines couplers for mm-wave applications. The concept is based on CS-CPW. The modification on the S-CPW shielding layer leads to great design flexibility. Cutting some floating ribbons can be used to modify coupling while maintaining equal magnetic and electric coupling coefficients. This solution overcomes all the C-µstrip couplers limitations, and offers the possibility to design compact directional couplers, with strong to weak couplings and high-directivity. Electrical models were derived in order to study the evolution of coupling coefficients when varying the geometrical dimensions in previous chapter. For a proof-of-concept, two couplers were designed with weak and strong coupling, at 150 GHz and 50 GHz working frequencies, respectively. They both exhibit good directivity when compared to microstrip counterpart couplers. Furthermore, the slow-wave behavior of the S-CPWs leads to more compact devices.

3.8. References

[1] H. T. Nguyen, “Design of Coupled Three-Line Impedance Transformers”, *IEEE Microw. Compon. Lett.,* vol. 24, no. 2, pp. 84-86, Feb. 2014.

[2] A. Pottrain , “State of the art 200 GHz power measurements on SiGe:C HBT using an innovative load pull measurement setup”, in *Int. Microw. Symp. Dig.*, Montreal, Canada, 2012.

[3] M. Meng, M. Chirala, N. Cam, "Millimeter-wave CMOS miniature resonator and coupler," in *Microw. Radar and Wireless Commun.*, Wroclaw, Poland, 2008.

[4] K. Chun-Lin, K. Che-Chung, L. Chun-Hsien, T. Jeng-Han, W. Huei, "A Novel Reduced-Size Rat-Race Broadside Coupler and Its Application for CMOS Distributed Sub-Harmonic Mixer," *IEEE Microw. Compon. Lett.,* vol. 18, no. 3, pp. 194,196, Mar. 2008.

[5] T.A. Winslow, "A novel broadside coupler model for MMIC impedance transformer design," in *European Microw. Conf.*, Manchester, UK, 2011.

[6] M. Dydyk, *et al*, "Accurate design of microstrip directional couplers with capacitive compensation,” in *Int. Microw. Symp. Dig.,* Dallas, USA, 1990.

[7] K. Dong-Joo; *et al*, "A novel design of high directivity CPW directional coupler design by using DGS," in *Int. Microw. Symp. Dig.,* Long Beach, USA, 2005.

[8] N.S.A Arshad, S.F. Yaacob, S.Z. Ibrahim, M.S. Razalli, "0 dB coupler employing slot technique on planar microstrip," in *Int. Conf. Computer, Communications, and Control Technology,* Langkawi, Malaysia, 2014.

[9] J. Shi, X.Y. Zhang, K.W. Lau, J.-X. Chen, Q. Xue, "Directional coupler with high directivity using metallic cylinders on microstrip line," *Electron. Lett.*, vol. 45, no. 8, pp. 415-417, Apr. 2009.

[10] D. M. Pozar, “Power dividers and Directional Couplers,” in *Microwave Engineering*, 4th ed., USA: Wiley, 1998, ch. 7, sec. 6, pp. 337-349.

[11] R. K. Mongia, I. Bahl, and P. Bhartia, “Characteristics of Planar Transmission Lines,” in *RF and microwave coupled-line circuits*, 2th ed., USA: Artech House, 2007, ch. 3.

[12] Ansys, HFSS [Online], Available: http://www.ansys.com

[13] J. Lugo-Alvarez, A. Bautista, F. Podevin, P. Ferrari, "High-directivity compact slow-wave CoPlanar waveguide couplers for millimeter-wave applications," in *European Microw.Conference,* Rome, Italy, 2014.

[14] M. Wojnowski, V. Issakov, G. Sommer, and R. Weigel, “Multimode TRL Calibration Technique for Charecterization of Differential Devices,” *IEEE Trans. Microw. Theory Techn*., vol. 60, no. 7, pp. 2220-2247, Jul. 2012 .

Chapter 4

Millimeter-Waves Parallel-Coupled Line Filters with CS-CPW

4.1. Introduction

In the previous chapters, the study of coupled lines was mainly focused on the realization of directional couplers. Coupled lines can also be used to realize filters. As well as directional couplers, filters are fundamental elements in several applications at mm-wave. All microwave receivers, transmitters, mixers, multiplexers, satellite communications (SATCOM), mobile communications, radars [1], or test and measurement systems, require filters.

Traditional filters are fabricated with lumped elements. This solution is very useful at low frequency. In the mm-wave range, lumped elements are not the most appropriated solution because of the high losses of these components, the numerous parasitics to consider and consequently many troubles whilst designing. Distributed elements as transmission lines are thus a good approach to implement filters at high frequency. Above say 80-100 GHz, distributed filters can show sizes comparable to their lumped counterparts. Besides, the electrical characteristics of the transmission lines can be fully predicted, which simplifies the design, leading to even lower-cost devices. For this reason, there is a high interest in finding new topologies of transmission lines to implement mm-wave filters. In this thesis the CS-CPW is proposed to improve the current performance of filters.

In this chapter filters implemented with parallel-coupled lines based on CS-CPW are studied. First, the classical theory for filters with parallel-coupled lines is presented. Then, charts of CS-CPW characteristic impedance versus geometrical parameters are developed. These are drawn with the help of the analytical model presented in Chapter 2. Next, resonators and filters are designed at 80 GHz. Finally measurement results are shown and results are compared to the state-of-the-art.

4.2.Classical parallel coupled line filter theory

This section is a brief review of a filter implementation with parallel-coupled lines.

A filter is a two-port network used to control the frequency response by enabling transmission at chosen frequencies. Classical frequency responses for filters are: low-pass, high-pass, band-pass, and band-reject. In this thesis, parallel-coupled line filter based on CS-CPW is analyzed as a solution for band-pass filtering at mm-wave.

The parallel-coupled line filter equations were formulated in [2]. Until the 1990's, other authors have modified those formulas depending on their proper application [3]-[9]. In [5], a procedure for microstrip tapped-line was introduced. In [7] a new design technique for parallel-coupled line filters based on a line and a stub equivalent circuit was presented. Finally, in [9] a capacitive compensation technique was described for the design of parallel-coupled line filter with improved passband symmetry.

Passband filters can be obtained by cascading coupled line sections of the form shown in Figure 4-1 [10].

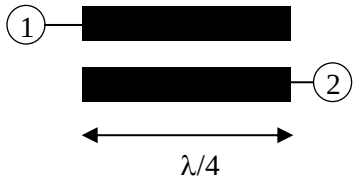

Figure 4-1: Parallel-coupled line section. Microstrip line technology.

A classical filter based on coupled lines consists of $n+1$ sections of the same electrical length ($\lambda/4$), leading to a structure composed by n resonators of length $\lambda/2$, as represented in Figure 4-2.

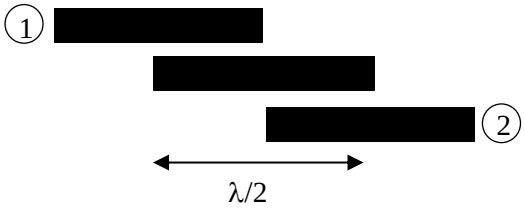

Figure 4-2: Top view of a parallel-coupled line resonator filter composed by two sections of $\lambda/4$ length each. Microstrip line technology.

Each pair of parallel-coupled lines is specified by the characteristic impedances of even- and odd-modes. Using the characteristic impedances values of each mode, the dimensions of the coupled lines can then be determined thanks to charts.

On the basis of the equations given in [1], the design method is summarized below.

The section of coupled line in Figure 4-1 is equivalent to the electrical circuit given in Figure 4-3.

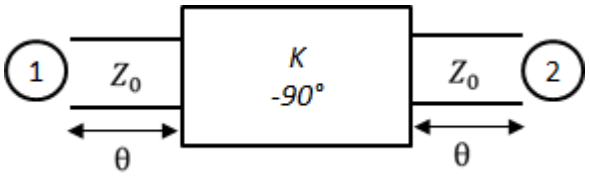

Figure 4-3: Equivalent circuit of the coupled line section consisting of an ideal impedance transformer inserted between two transmission lines of electrical length θ.

The ABCD matrix of the ideal impedance inverter in Figure 4-3 is equivalent to the ABCD matrix of a regular transmission line of length $\lambda/4$ and characteristic impedance K. Therefore, the total ABCD parameters of a single section filter (Figure 4-3) can be calculated from the multiplication of the ABCD matrices of the transmission lines with the ABCD matrix of the ideal impedance inverter:

$$\begin{bmatrix} A & B \\ C & D \end{bmatrix} = \begin{bmatrix} \cos\theta & jZ_0 \sin\theta \\ \dfrac{j\sin\theta}{Z_0} & \cos\theta \end{bmatrix} \begin{bmatrix} 0 & -jK \\ -j/K & 0 \end{bmatrix} \begin{bmatrix} \cos\theta & jZ_0 \sin\theta \\ \dfrac{j\sin\theta}{Z_0} & \cos\theta \end{bmatrix} \quad (4\text{-}1)$$

Each section of coupled line must have an electrical length equivalent to $\lambda/4$. For $n+1$ sections, there are $n+1$ impedance inverters, namely $K_{j,j+1}$, $j = 0$ to n. The impedance inverter $K_{j,j+1}$, equivalent to a $\lambda/4$ section, is calculated according to equations (4-2) to (4-4), where Z_0 is the input impedance and FBW is the fractional bandwidth of the filter [1]. The terms g_j are polynomial coefficients of order n (Chebishev or any other function, depending on the flatness or equal ripple to be reached).

$$\frac{Z_0}{K_{01}} = \sqrt{\frac{\pi FBW}{2\omega_1 g_0 g_1}} \tag{4-2}$$

$$\frac{Z_0}{K_{j,j+1}} = \frac{\pi FBW}{2\omega_1 \sqrt{g_j g_{j+1}}}, j = 1 \text{ to } n-1 \tag{4-3}$$

$$\frac{Z_0}{K_{n,n+1}} = \sqrt{\frac{\pi FBW}{2\omega_1 g_n g_{n+1}}} \tag{4-4}$$

Equations (4-5) and (4-6) specify the value of the characteristic impedances of the even- and odd-modes of each parallel section. They are expressed as a function of the previously computed inverters coefficients:

$$\frac{(Z_C^{even})_{j+1}}{Z_0} = 1 + \frac{Z_0}{K_{j,j+1}} + \left(\frac{Z_0}{K_{j,j+1}}\right)^2, j = 0 \text{ to } n \tag{4-5}$$

$$\frac{(Z_C^{odd})_{j+1}}{Z_0} = 1 - \frac{Z_0}{K_{j,j+1}} + \left(\frac{Z_0}{K_{j,j+1}}\right)^2, j = 1 \text{ to } n \tag{4-6}$$

Once the needed characteristic impedances to realize the filter are calculated from previous equations, the physical dimensions of the coupled lines can be found. In the next section the characteristic impedances of the CS-CPW and the relation with their dimensions are presented.

4.3. Odd and even-modes characteristic impedances

The required dimensions for the coupled lines are going to vary according to the chosen topology (in this case we use CS-CPWs) and also according to the technology where these lines will be integrated. In the literature we can find similar charts for the microstrip topology [11].

To know the dimensions of the CS-CPWs that must be fabricated, a chart giving the odd- and even-modes characteristic impedances is presented in Figure 4-4.

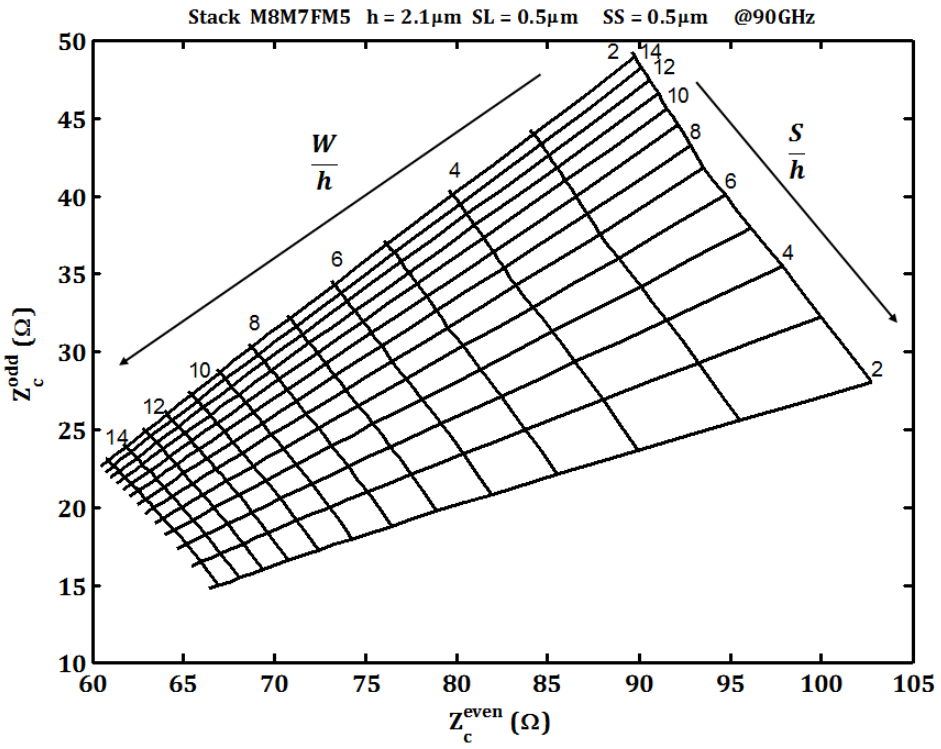

Figure 4-4: Even-(Z_c^{even}) and odd-(Z_c^{odd}) modes characteristic impedance for CS-CPW, as a function of W and S.

The evolution of the characteristic impedances versus the ratios (S/h and W/h) is represented. It permits the choice of the CS-CPW dimensions. Hence, from these charts, the designers can extract the information to implement resonators and filters for mm-wave applications. In Figure 4-4, the CS-CPW has been analyzed without any modification in the shielding under the CPW strips. In next sub-section, we will see that cutting the floating shielding may give a new degree of freedom to design filters.

4.3.1. Characteristic impedances when cutting the floating ribbons

Previously in Chapter 2, we have discussed about the effect in terms of coupling when the floating electromagnetic shielding is cut (either in the center *CC* or on the sides *CS*). It has been explained that the cut does not perturb the magnetic field. However, the electric field is being modified. Therefore the equivalent capacitances of the CS-CPW are being affected. In Chapter 2 and Chapter 3, the main concern was the coupling coefficient. However, the modification in the shielding also leads to a variation in the characteristic impedance of the coupled line. In this chapter, the main focus will be on the study of the even- and odd-mode characteristic impedances.

When the floating shielding is cut, two cases are possible. Let consider the first case when the electromagnetic shielding is cut in the center (*CC*). The characteristic impedances of each mode with a *CC* of 2 µm are presented in Figure 4-5.

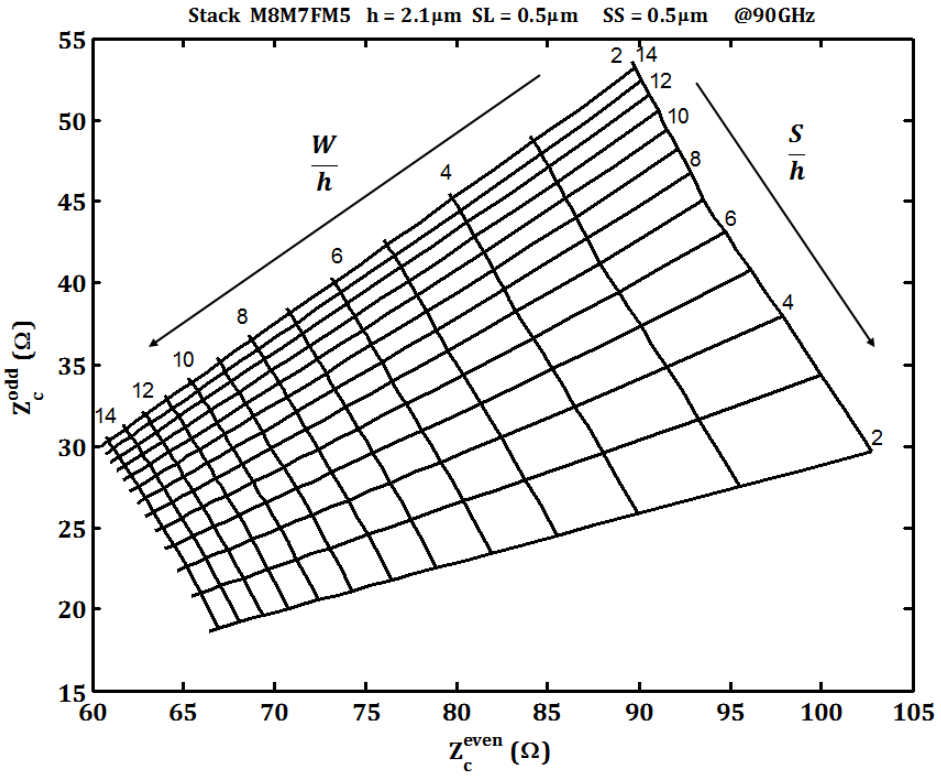

Figure 4-5: Even-(Z_c^{even}) and odd-mode (Z_c^{odd}) characteristic impedance for CS-CPW as a function of W and S when the shielding is cut in the center (CC = 2 µm).

In Figure 4-5 the evolution of the characteristic impedances versus the ratios (S/h and W/h) is showed for CC = 2 µm. In that case, the odd capacitance C^{odd} is affected. C^{odd} decreases when the shielding is cut in the center, leading to an increase up to 20 % of the odd-mode characteristic impedance Z_C^{odd}; while the Z_C^{even} is not perturbed by the cut in the center.

Now, let consider the second case when the shielding is cut on the sides (CS). The CS is placed just underneath the middle of the gap G. Similarly, the characteristic impedances of the modes are presented in Figure 4-6.

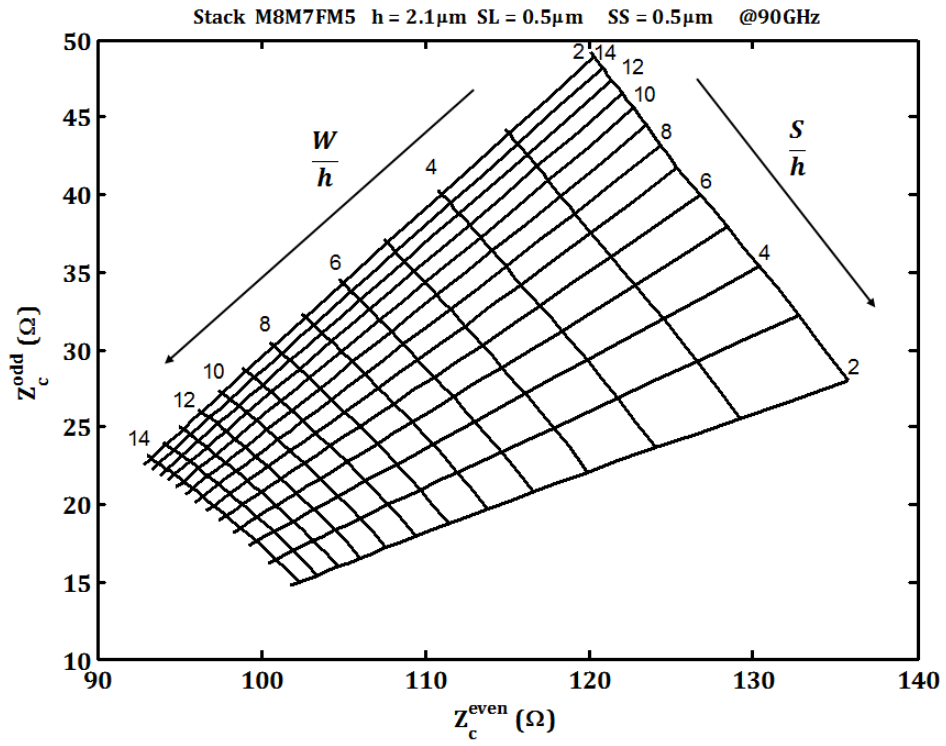

Figure 4-6: Even-(Z_c^{even}) and odd-mode (Z_c^{odd}) characteristic impedance for CS-CPW as a function of W and S when the shielding is cut on the sides (*CS*).

In Figure 4-6 the evolution of the characteristic impedances versus the ratios (S/h and W/h) is showed for CS = 2 µm. The even capacitance C^{even} is affected when cut on the sides. C^{even} decreases when the shielding is cut on the sides, therefore Z_C^{even} increases up to 30 %; meanwhile Z_C^{odd} remains unperturbed.

Table 2-3 summarizes the effect of cutting the electromagnetic shielding over the capacitances and the characteristic impedances. The equivalent inductances are not mentioned because cutting the floating shielding does not affect the magnetic field.

TABLE 4-1 EQUIVALENT CAPACITANCES AND IMPEDANCES VERSUS CUT

Parameter	*CS*	*CC*
C^{even}	↓	⟶
Z_C^{even}	↑	⟶
C^{odd}	⟶	↓
Z_C^{odd}	⟶	↑

Cutting the electromagnetic shielding gives the filter designer a new degree of freedom. Characteristic impedances (even- and odd-modes) can be controlled independently thanks to this concept.

In general, the even-mode characteristic impedance is high for the CS-CPW with regular shielding (without any cut). High even-mode characteristic impedance is appropriated for the design of filters; therefore, there is no interest in *CS* in that case. On the other hand, the odd-mode characteristic impedance is in general very low for CS-CPW. This is due to odd-mode capacitance (C^{odd}) which is high for the CS-CPW. However, in the filter design, high odd-mode characteristic impedances are required. This is why the cut in the center *CC* is very interesting. *CC* will allow the designer to increase the odd-mode characteristic impedance.

The three charts presented in this section are a result of the analytical model developed for CS-CPW in the laboratory. The theoretical basis of this model has been discussed in Chapter 2, section 2.8, and published in [43]. The dimensions have been chosen according to the design kit of the technology BiCMOS 55 nm by ST Microelectronics. The stack enables a strong slow-wave effect thanks to floating ribbons placed in Metal 5 and signal and ground strips in Metal 8-7, respectively. The resulting height h is around 2 µm, leading to a high equivalent capacitance. In order to maintain good attenuation, signal and ground strips are in the thicker layers while shielding is designed in the thinner layer. This stack is the best compromise to ensure a quality factor better than 30.

4.4.Design

In this section, the opportunities offered by the cutting of the shielding are used to implement two bandpass filters centered at 80 GHz. First a single resonator (i.e two identical CS-CPW sections) is designed. Second, the work focuses on a 3-pole filter where three resonators (i.e. four CS-CPW sections) are cascaded in order to increase selectivity. Implementing a single resonator is mandatory since it is the fundamental element of the final targeted filter. It provides useful information in order to understand the behavior of the third-order filter. The single resonator measurement also gives information concerning the quality factor of the transmission lines. Also, high quality factor in the resonator is the *sine qua non* condition to ensure a good quality factor of the third-order filter.

4.4.1. Parallel-coupled lines resonator

Equations (4-1) to (4-6) are used for the resonator design. However these equations result in any pair of characteristic impedances for each mode. At the meantime, it is observed that maximum Z_C^{odd} for CS-CPW with the BiCMOS 55 nm technology from ST Microelectronics is around 60 Ω. This value limits the design solutions regardless the function used for the filter design (Chebyshev, Butterworth, Bessel, etc). For this reason, an optimization of the filter was carried out with ADS, which takes into account the CS-CPW limits in terms of characteristic impedances. As a result of the optimization, each section of coupled lines presents a

characteristic impedance $Z_C^{even} = 95\ \Omega$ and $Z_C^{odd} = 51\ \Omega$. Figure 4-7 shows the layout of this resonator.

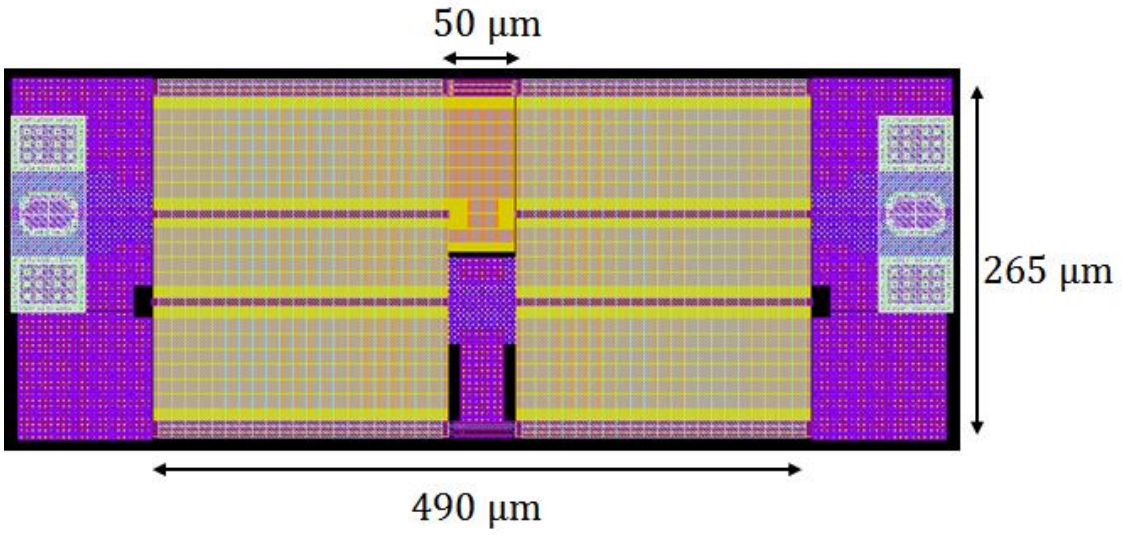

Figure 4-7: Layout of the fabricated parallel-coupled lines resonator implemented with a CS-CPW topology.

The resonator in Figure 4-7 is composed of two identical sections of CS-CPWs. Each section has the following dimensions: $W = 5$ µm, $W_g = 12$ µm, $G = 85$ µm, and $S = 60$ µm. As already mentioned the floating ribbons are placed in metal M5 and signal and ground strips are stacked from metal M8 to M7. The resonator results with ideal coupled lines from ADS and CS-CPWs simulated in HFSS are plotted in Figure 4-8.

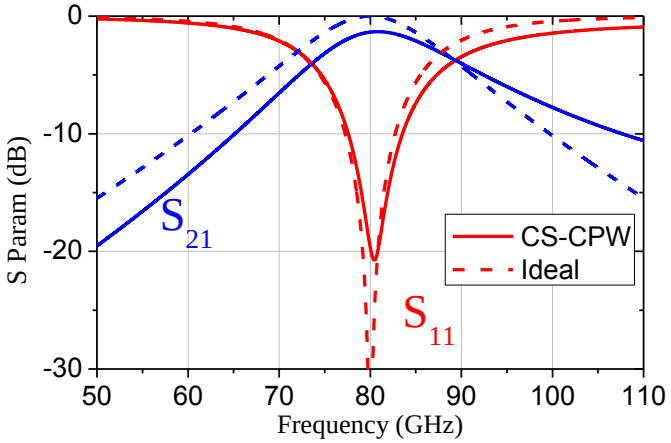

Figure 4-8: Simulation results of the parallel-coupled lines resonator implemented with a CS-CPW topology.

The resonator in Figure 4-8 presents a relative bandwidth equal to 21.9 %. The insertion loss at center frequency is 1.3 dB. At 80 GHz, the performance of the resonator is very promising.

The design of this single resonator at 80 GHz allows the design of a more complex circuit, i.e. the filter presented in next section.

4.4.2. Parallel-coupled lines third-order filter

According to the theory presented in section 1.3, a third-order filter was implemented by using four sections of CS-CPW, as shown in Figure 4-9 . Section 1 is identical to section 4; these are referred as the external sections. Besides, section 2 is identical to section 3; these are referred as the central sections.

Due to the maximum values of Z_C^{odd}, design formulas could not be used, therefore an ADS optimization was needed as well. The external CS-CPWs (section 1 and section 4 in Figure 4-9) have the same characteristic impedance as the single resonator ($Z_C^{even} = 95\ \Omega$ and $Z_C^{odd} = 51\ \Omega$) designed in the previous section. The central CS-CPWs (section 2 and section 3 in Figure 4-9) were built with $Z_C^{even} = 63\ \Omega$ and $Z_C^{odd} = 48\ \Omega$. Figure 4-9 shows the final layout of this filter.

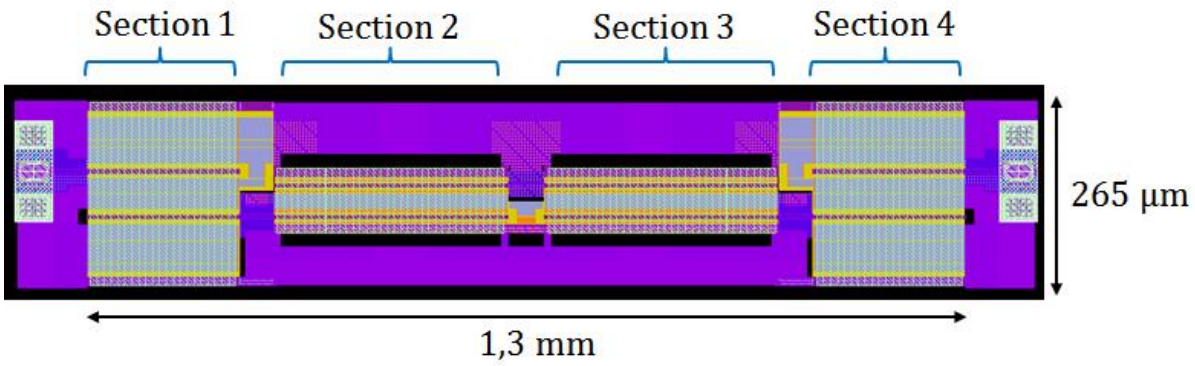

Figure 4-9: Layout of the parallel-coupled lines filter implemented with three cascaded resonators based on a CS-CPW topology.

The dimensions of the CS-CPWs used for the filter design are given in Table 4-2.

TABLE 4-2 SUMMARY OF THE FILTER DIMENSIONS

Dimension	Section 1	Section 2	Section 3	Section 4
W	5 µm	5 µm	5 µm	5 µm
S	60 µm	40 µm	40 µm	60 µm
G	85 µm	10 µm	10 µm	85 µm
W_g	12 µm	12 µm	12 µm	12 µm
Cut	No	Only *CC*	Only *CC*	No

The simulation results of the filter are shown in Figure 4-10.

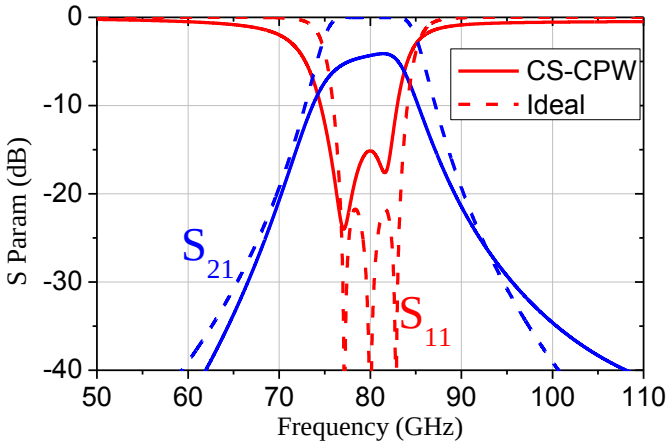

Figure 4-10: Simulation results of the parallel-coupled transmission lines filter implemented with three series resonators based on a CS-CPW topology.

The response of the filter simulated with the CS-CPWs electrical model is compared to the response of a filter implemented with ideal coupled lines. The CS-CPW filter in Figure 4-10 has a fractional bandwidth of 11.1 %. The insertion loss of 4 dB, although it quite high, correspond to the state-of-the-art for filters integrated in CMOS/BiCMOS technology at mm-wave. In section 4.5 the performance of this filter is compared to the state-of-the-art. Besides, these results are a way to evaluate the performance of the proposed CS-CPW technology. In the next section, a discussion is carried out concerning the practical implementation (layout) issues for these devices.

4.4.3. Practical issues

Up to now, all the previous designs considered sections that can be easily interconnected. In this part the layout issues, leading to parasitic effects, are discussed. The layout proposed in Figure 4-2 can be easily applied to a coupled microstrip topology. However, this distribution could present some complications (red circles in Figure 4-11) when using a CS-CPW topology.

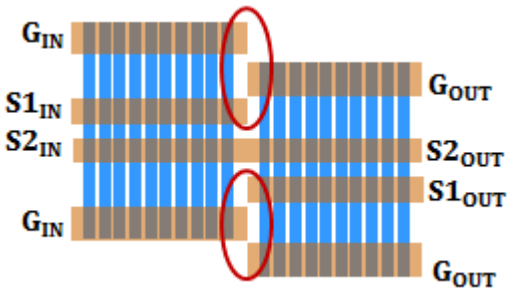

Figure 4-11: Top-view of first proposition to implement a resonator with CS-CPW.

From Figure 4-11 we can see that ground strips connections must be optimized in order to minimize parasitic couplings between ground and signal strips. In the layout, the ground strips can almost touch the signal strips. Particularly G_{OUT} is close to $S1_{IN}$ and G_{IN} to $S1_{OUT}$ (see Figure 4-11) which might results into strong parasitic couplings. The solution in practical terms for this issue is proposed in Figure 4-12.

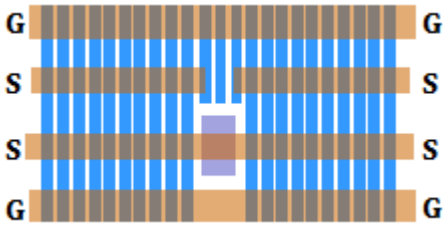

Figure 4-12: Top-view of the second solution to implement a CS-CPW based resonator.

Ground strips are aligned. Then, and most important, the transition between the two sections of coupled lines is considered. It consists of a very short microstrip line with no ground reference but floating ribbons to prevent the electric field from flowing through the lossy substrate, as illustrated in Figure 4-12. In this way, a small phase will have to be previously compensated during the design of each pair of coupled lines. The presented performances in this chapter are the results of electromagnetic simulations with HFSS [17]. The transition with microstrip lines was not yet considered.

4.5. Comparison of CS-CPW with state-of-the-art

The circuits designed in section 4.4 will be fabricated in a BiCMOS 55 nm technology by ST Microelectronics. The targeted tape-out is December, 2015. In order to better predict measurement results, simulations of the topology considering practical issues were carried out. Simulation results are presented and compared to the state-of-the-art in the next subsections below.

4.5.1. Simulation with HFSS of the CS-CPW based resonator

It has been shown that a transition between the two CS-CPWs was needed. Even if compensated by a modification of the coupled lines, the transition electrical length must be as small as possible so that it can be compensated without scarifying the filter performance. 50 µm long transition were used, as shown in Figure 4-13.

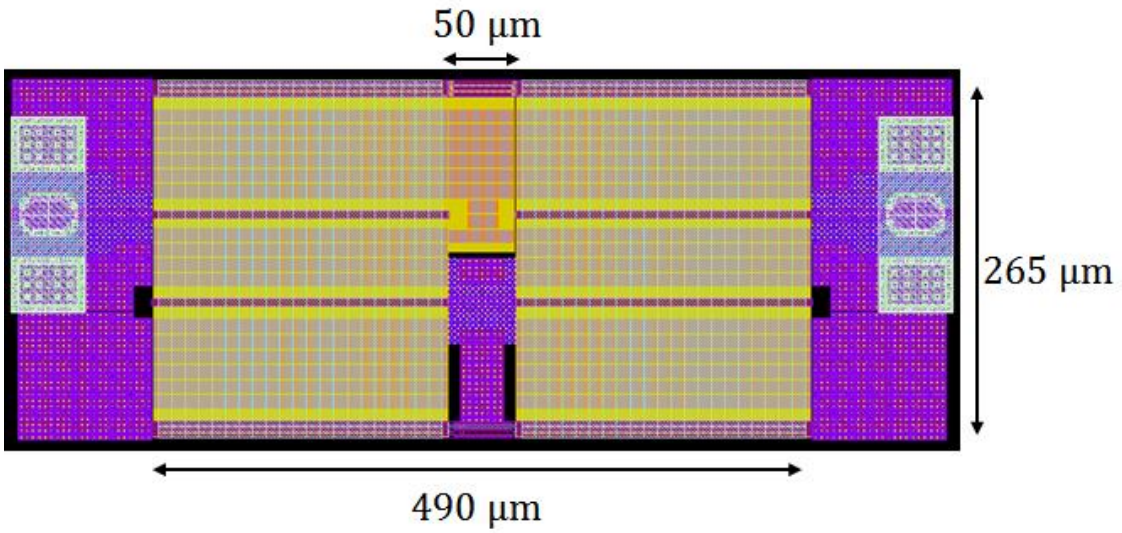

Figure 4-13: Layout of the fabricated parallel-coupled transmission lines resonator implemented with a CS-CPW topology.

This 50 µm transition is equivalent to an electrical length of 5° at the center frequency (80 GHz). The choice of 50 µm results from a compromise between parasitic coupling between opposite strips and electrical length. The simulation results of the resonator after optimization with the transition are presented in Figure 4-14.

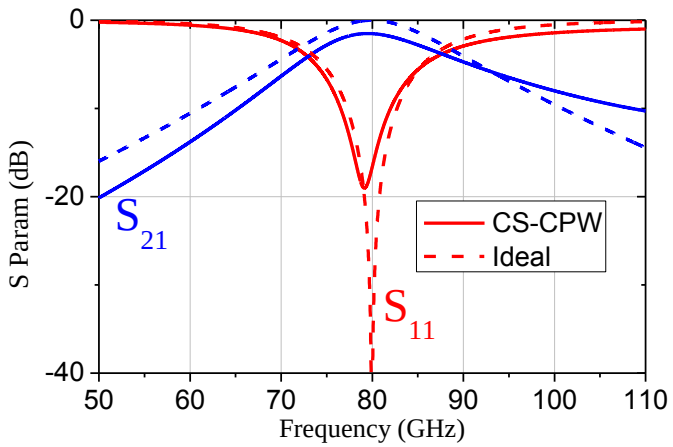

Figure 4-14: Simulation results of the parallel-coupled transmission lines resonator implemented with a CS-CPW topology considering the transition.

The simulation results are compared to those obtained for a lossless resonator implemented with ideal coupled lines. The resonator in Figure 4-14 presents a relative bandwidth equal to 22 %. The insertion loss at center frequency is 1.5 dB. We can observe in Figure 4-14 that the filter response is not that much modified, thanks to an efficient optimization of the filter taking into account the transition.

4.5.2. Comparison with the state-of-the-art

In order to understand the electrical performance or the space occupied by these filters, a summary of the filter listed in Table 1-1 is presented in Figure 4-15. A 70 GHz compact folded loop dual-mode filter is showed in [13]. The filter consists in a planar ring resonator structure with two transmission zeros. The ring resonator is interesting in terms of high selectivity and size. The filter in Figure 4-15 (a) is composed of a ring resonator, two feeding lines and a perturbation section. A similar technique is used in [14], planar dual-mode ring resonators are considered to design the filter illustrated in (Figure 4-15 (b)). The ultra-compact size occupied by filter in [15] is because of the grounded pedestal stepped-impedance technique (Figure 4-15 (c)). The grounded-pedestal introduces the slow-wafe effect which reduces the size of the filter. Finally the slow-wave effect is also used in [16], where a bandpass filter is made with S-CPW open stubs (Figure 4-15 (d)).

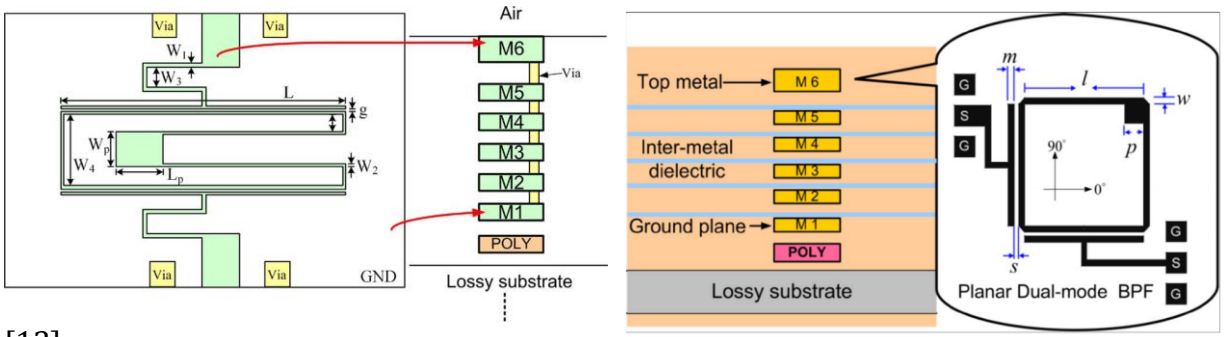

[13]

(a)

(b)

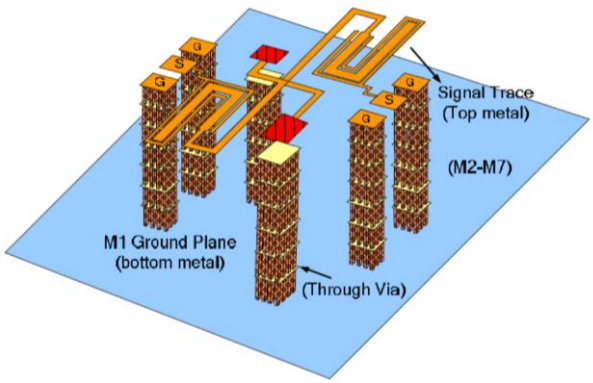

(c)

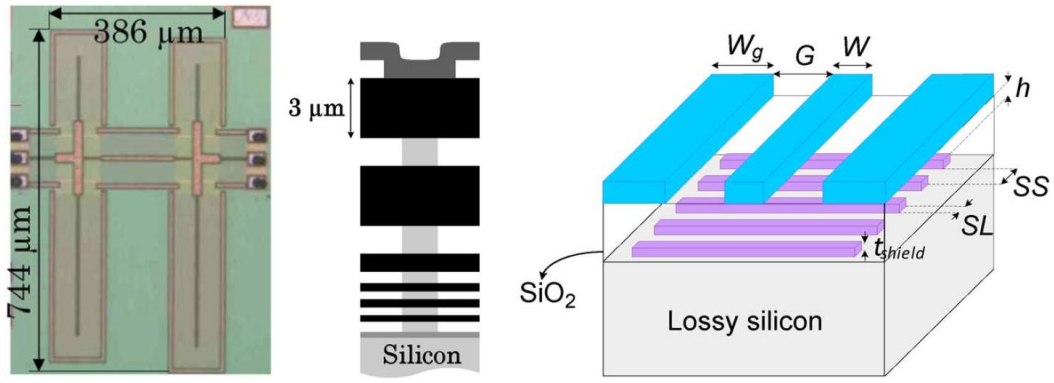

(d)

Figure 4-15: Mm-wave filters integrated in advanced CMOS technologies. (a) Folded loop dual-mode filter [13], (b) square loop dual-mode filter [14], (c) filter using grounded pedestal stepped-impedance stubs [15] and (d) filter with T-junctions and open stubs using S-CPWs [16].

The performance of four filters in a 0.18 µm CMOS and a 0.13 µm technology are compared in Table 1-1 to the one developed in this work. All these filters work around the 60 - 80 GHz frequency range.

TABLE 4-3 STATE-OF-THE-ART OF FILTER AROUND 80 GHZ IN CMOS TECHNOLOGIES

Technology	Surface	Freq.	FBW	IL (dB)	Q_u	Order	References
CMOS 0.18 µm	0.44 mm²	70 GHz	26 %	-3.6	15.8	2	[13]
	1.71 mm²	64 GHz	20 %	-4.9	15.1	2	[14]
CMOS 0.13 µm	0.08 mm²	76 GHz	25 %	-4	14.8	2	[15]
	0.29 mm²	60 GHz	17 %	-4.1	21.3	2	[16]
BiCMOS 55 nm	0.13 mm²	80 GHz	22 %	-1.3	32	1	This work
	0.34 mm²	80 GHz	11.2 %	-4.1	24.6	3	This work

The unload quality factor Q_u allows the comparison between filters. This parameter is calculated with equation [17] when the design process explained at the beginning of this chapter can be followed:

$$Q_u = 4.343 \frac{\sum_{i=1}^{n} g_i}{FBW\ (IL)} \tag{4-7}$$

This equation cannot be used in our precise case and equation (4-8) is then used.

$$Q_u = \frac{1}{FBW\left(1 - 10^{\frac{IL}{20}}\right)} \tag{4-8}$$

considering that the insertion loss can be expressed as:

$$S_{21} = IL = 20\log\left(1 - \frac{Q_L}{Q_u}\right) \tag{4-9}$$

where Q_L is calculated from:

$$Q_L = \frac{1}{FBW} \tag{4-10}$$

The unload quality factor of our 3rd order filter is multiplied almost by two as compared to the references thanks to the slow-wave effect. In [15] they are using microstrip technology, the overall size of the filter is smaller than the filter in this thesis. This is because of the folding; however, the physical propagation length reminds a classical one leading to more conductive losses. This can also be observed with the *IL* and the bandwidth. For the same value of *IL*, the designed filter presents more selectivity than the other filters on the literature. Finally it is important to emphasize that the single resonator filter needed very small area. These results prove the interest of CS-CPWs in mm-wave systems.

4.6. Conclusion

In this chapter, the new topology for coupled lines presented in this thesis has been used to implement mm-wave passband filters. First, the study was focused on the characteristic impedances of the CS-CPWs, in order to draw charts necessary for the filter design. It was demonstrated that cutting the floating strips could lead to new degrees of freedom. When cutting the floating strips of the shielding on the sides, the even-mode characteristic impedance is increased from 102 Ω to 135 Ω. On the other hand, when cutting them in the center, the odd-mode characteristic impedance is increased from 50 Ω to 60 Ω. These new improvements permitted to design an efficient third-order filter working at 80 GHz. Its overall electrical performance is very interesting, with predicted state-of-the-art "low" insertion loss, and a wideband rejection band. These circuits will be fabricated in a BiCMOS 55 nm technology by ST Microelectronics.

4.7.References

[1] R. K. Mongia, I. Bahl, and P. Bhartia, "Coupled-Line Filter Fundamentals," in *RF and microwave coupled-line circuits*, 2th ed., USA: Artech House, 2007, ch. 9, sec. 3, pp. 283-287.

[2] S. B. Cohn, "Parallel Coupled Transmission Line Resonant Filters," *IEEE Trans. Microw. Theory Techn*., vol. 6, no. 2, pp. 223-232, Apr. 1958.

[3] M. R. Moazzam, S. Uysal, and A. H. Aghvami, "Improved performance Parallel Coupled Microstrip Filters," *Microw. J.*, vol. 34, no. 11, Nov. 1991.

[4] J. F. Mara, and J. B. Schappacher, "Broadband Microstrip Parallel-coupled Filters using Multi-Line Sections," *Microw. J.*, vol. 22, no. 4, pp. 97-99, Apr. 1979.

[5] J. S. Wong, "Microstrip Tapped-Line Filter Design," *IEEE Trans. Microw. Theory Techn*., vol. 27, no. 1, pp. 328-339, Jan. 1979.

[6] M. Tran, and C. Nguyen; "Wideband Bandpass Filters Employing Broadside Coupled Micrstrip Lines for MMIC Applications," *Microw. J.*, vol. 37, no. 4, pp. 210-225, Apr. 1994.

[7] B. J. Minnis, "Printed Circuit Coupled Line Filters for Bandwidths up to and greater than an Octave," *IEEE Trans. Microw. Theory Techn*., vol. 29, no. 3, pp. 215-222, Mar. 1991.

[8] C. Y. Ho, and J. H. Werdman, "Improved Design of Parallel coupled Line Filters with Tapped Input/Output," *Microw. J.*, vol. 26, no. 18, pp. 127-130, Oct. 1983.

[9] I. J. Bahl, "Capacitively compensated High-Performance Parallel-Coupled Microstrip Filters," in *Int. Microw. Symp. Dig.,* Jun. 1989.

[10] D. M. Pozar, "Microwave Filters," in *Microwave Engineering*, 4th ed., USA: Wiley, 1998, ch. 8, sec. 7, pp. 416-425.

[11] D. M. Pozar, "Power dividers and Directional Couplers," in *Microwave Engineering*, 4th ed., USA: Wiley, 1998, ch. 7, sec. 6, pp. 339-340.

[12] A. Bautista, A.-L Franc, and P. Ferrari, "An Accurate Parametric Electrical Model for Slow-wave CPW," in *Int. Microw. Symp.,* Phoenix, USA, June 2015.

[13] C. Y. Hsu, C.Y. Chen, and H.R. Chuang, "70 GHz Folded Loop Dual-Mode Bandpass Filter Fabricated Using 0.18-μm Standard CMOS Technology," *IEEE Microw. Compon. Lett.*, vol. 18, no. 9, pp. 587-589, Sept. 2008.

[14] C. Y. Hsu, C. Y. Chen, and H.R. Chuang, “A 60-GHz millimetre-wave bandpass filter using 0.18-μm CMOS technology,” *IEEE Electron Device Lett.*, vol. 29, no. 3, pp. 246-248, Mar. 2008.

[15] Y. -M. Chen, and S.-F. Chang, "A ultra-compact 77-GHz CMOS bandpass filter using grounded pedestal stepped-impedance stubs," in *European Microw. Conf.,* Manchester, United Kingdom, Oct. 2011.

[16] A.-L. Franc, E. Pistono, D. Gloria, and P. Ferrari, "High-Performance Shielded Coplanar Waveguides for the Design of CMOS 60-GHz Bandpass Filters," *IEEE Trans. Electron Devices*, vol. 59, no. 5, pp. 1219-1226, May 2012.

[17] J.-S. Hong, and M. J. Lancaster, Microwave filters for RF/microwave applications, Ed. John Wiley & Sons, Inc., 2001.

[18] Ansys, HFSS [Online], Available: http://www.ansys.com

Chapter 5

Applications of the CS-CPW Directional Couplers

5.1. Introduction

In the previous chapters CS-CPW based directional couplers have been validated by simulations and measurements up to 150 GHz. Directional couplers are fundamental parts of several mm-wave systems. Because of the promising characteristics of CS-CPW couplers, good performance is expected for these systems.

In this chapter some applications of the directional couplers are presented. These applications were developed in our laboratory by several researchers. The first exploitation of CS-CPW is the design of a Reflection Type Phase Shifter (RTPS) at 47 GHz. Next an isolator is integrated with CS-CPWs at 77 GHz. Finally, an 80 GHz balun with CS-CPW couplers is presented.

5.2. Reflection-Type Phase Shifter (RTPS) with CS-CPW

The first RTPS was proposed in 1960 [1]. RTPS theory and applications have been discussed in a previous PhD thesis by François Burdin [2], and is currently studied by the IMEP-LaHC PhD student Zyad Iskandar, [3]and [4]. The RTPS is a two-port network allowing the phase shift of a signal, while assuming low insertion loss and return loss at both input and output ports. Figure 5-1 shows the block diagram of a conventional RTPS.

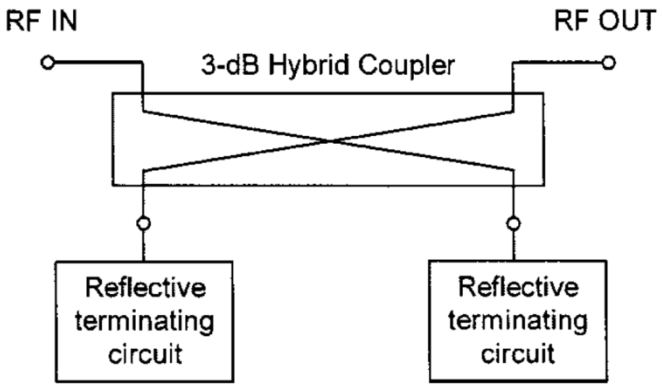

Figure 5-1: Schematic of the conventional reflection-type phase shifter (RTPS).

Conventional RTPS consists of a 3-dB 90° hybrid coupler and a pair of reflective terminating circuits [5]. The signal at the input port gets divided equally except the quadrature phase at coupled and through ports. These signals reflect from the terminating circuits and combine in phase at the output port. The advantage of this device is that matching at input and output ports is preserved for any phase shifting. This is not the case for tunable transmission lines based phase shifters. One disadvantage of conventional RTPS is their oversize due to bulkiness of hybrid couplers. More compact couplers have thus to be considered.

Figure 5-2 presents an antenna phased array system where phase shifters are needed for beam steering [6]; especially structures based on RTPS are much appreciated [7].

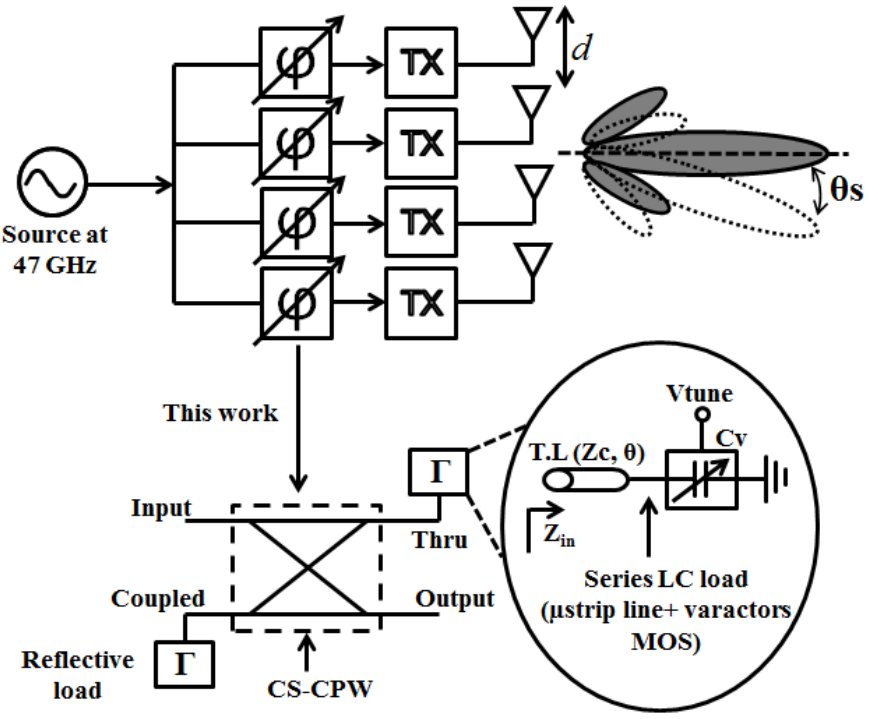

Figure 5-2: Antenna network and architecture of the RTPS with CS-CPW.

More precisely, the block diagram in Figure 5-2 corresponds to a 47 GHz transceiver front-end that will be integrated in a 55 nm SiGe technology. Phase shift is varied from 0 to 60° thanks to a series reflective load. It is worth mentioning that the hybrid coupler in Figure 5-1 has been replaced by a CS-CPW coupler. This solution combines low insertion loss as well as small footprint [8]. In this section the principle of this RTPS implemented with a CS-CPW is first presented, later coupler and RTPS performances are presented.

5.2.1. State-of-the-art of mm-wave phase shifters

This section reviews some designs of phase shifter used at mm-wave. It includes active and passive circuits. At the end, a table comparing the performance of the phase shifters is given.

A varactor-based passive phase shifter was presented in [9]. It was implemented in the IBM 0.13-µm SiGe BiCMOS technology. A π-type C-C load was used to achieve 180° continuous phase tuning in the RTPS. The schematic is presented in Figure 5-3.

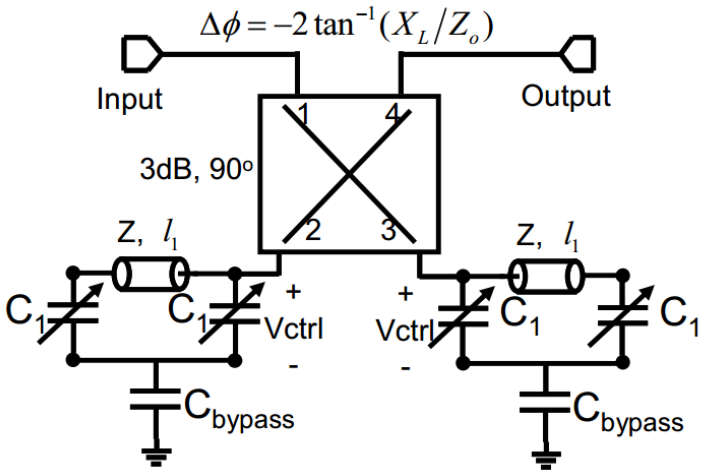

Figure 5-3: Schematic of RTPS with π-type C-L-C load [10].

It achieves the desired 180° phase variation with loss varying from 4.2 dB to 7.8 dB while the active interpolator provides 360° phase variation across the 57 GHz-64 GHz band while providing >10 dB gain control. In fact, the low quality factor of the silicon varactors increases the losses of the RTPS.

Insertion loss can be improved thanks to the use of MEMS switches, which exhibit much higher figure of merit than varactor diodes. A V-band 2-bit switched-line phase shifter using dc-contact single-pole four-throw (SP4T) RF-MEMS switches for 60-GHz applications was presented in [10]. The layout of the switch is presented in Figure 5-4.

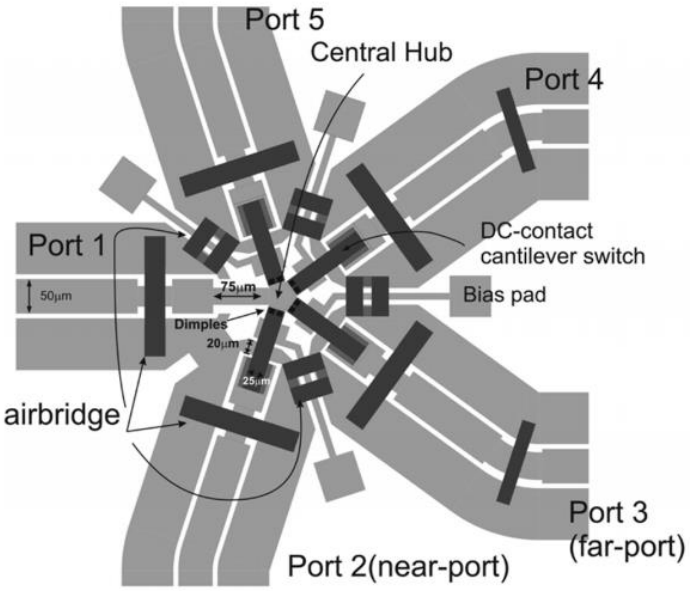

Figure 5-4: Layout of the SP4T RF-MEMS switch [11].

The circuit in Figure 5-4 is a broadband (up to 74 GHz) dc-contact SP4T RF-MEMS switch. In measurement, it presents insertion loss less than 1 dB and return loss better than 16 dB in the 55-65 GHz band. Using the switch in Figure 5-4 a phase shifter was fabricated. It has a phase error less than 1° and an average insertion loss of 2.5 dB at the center frequency. A similar idea was used in [11], where a 4-bit switch type phase shifter with low group delay and low loss flatness was presented. Nevertheless, switched-path type phase shifter are digital, which means that it could become bulky if a large number of phase states is desired. Usually phase shifters require high resolution in phase control, leading to a large and lossy digital phase shift system.

An "classical" solution is to periodically load a high-impedance transmission line with MEMS capacitors. In [12] low-loss digital distributed phase shifters were developed using micromachined capacitive shunt switches for V-band applications. In order to minimize the loss at V-band, high-Q metal-air-metal (MAM) capacitors in series with the MEMS capacitors were used for the shunt capacitive switch. The diagram of the MEMS-based phase shifter is shown in Figure 5-5. The insertion are quite low, i.e. 3.6 dB for a 337° phase shift, leading to a high figure of merit (FOM), defined as the maximum phase shift divided by the maximum insertion loss, equal to more than 90°/dB.

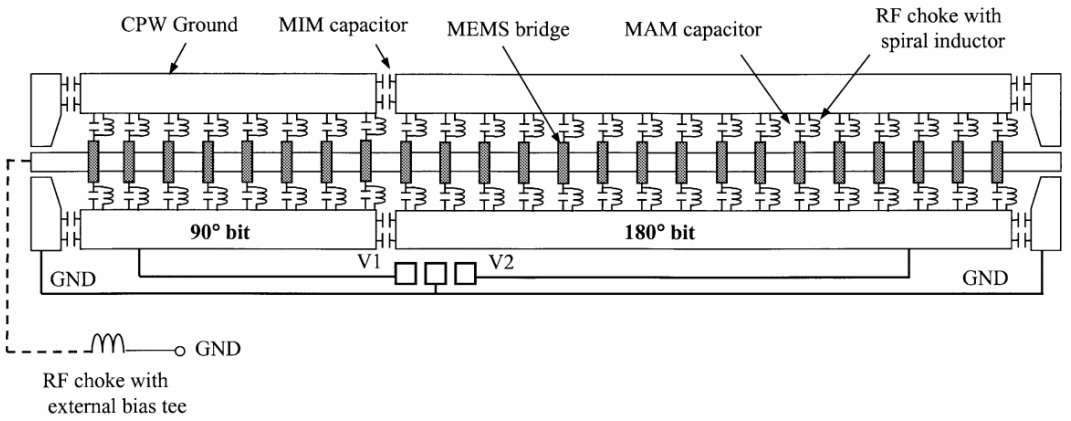

Figure 5-5: Diagram of the V-band 2-b MEMS-based phase shifter [12].

A similar idea was presented in [13] where a transmission line is loaded with MOS varactors. A differential varactor-loaded transmission line phase shifter was used (Figure 5-6).

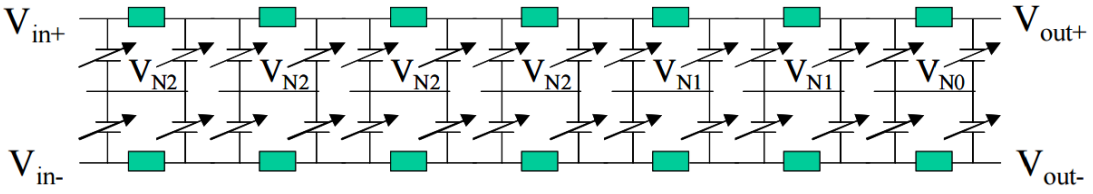

Figure 5-6: Schematic of a phase shifter where seven π-type sections are cascaded to realize a phase control range of 157.5° [13].

The phase shift of the loaded line can be controlled by varying the capacitance of each section (or set of sections).

The issue with this solution is the high loss brought by the varactors, i.e. 12.5 dB for a 156° phase shift, leading to a FOM limited to 12°/dB. Table 1-1 summarizes more in detail the state-of-the-art for the phase shifters described above.

TABLE 5-1 STATE-OF-THE-ART OF PHASE SHIFTER IN MM-WAVE

Ref./ Technology	Freq. (GHz)	Topology	Phase Shift (°)	IL (dB)	IL Variation (dB)	Return Loss (dB)	FoM (°/dB)	Area (mm²)
[9]/130nm SiGe	60	RT Varactor MOS	180	5.85	±1.65	N/A	24	0.18
[10]/quartz substrate	60	SL MEMS	269.2	2.5	±0.5	-13	89.7	4
[11]/90nm CMOS	60	SL without small-size capacitor	360	12.5	±2	<-10	24.8	0.28
[12]/quartz substrate	65	CPW loaded MEMs	337	2.8	±0.8	-10	93.6	9.45
[13]/65nm CMOS	60	Differential TL loaded MOS	156	9.25	±3.25	-13	12.5	0.2

According to Table 1-1 MEMS solutions are very interesting because it presents the best FoM. The maximum FoM of the phase shifters presented is around 90°/dB, [10] and [12]. The issue with these options is the surface occupied by these circuits. The area of these two devices is 4 and 9.45 mm² respectively. Besides, both solutions are fabricated on quartz substrate, which is not compatible with integrated technologies. For these reasons MEMS solutions are not the fittest for most of the applications. Among the moderate areas, the FoM dramatically decreases down to around 25°/dB for a maximal phase shift of 180° for RTPS and 360° for switched-network approach.

5.2.2. Principle of the RTPS with CS-CPW

The RTPS is composed of a 3-dB coupler realized with CS-CPWs, and a reflective load realized with a microstrip line and a MOS varactor. The signals reflected from the reflective load add in phase at the RTPS output, i.e. the isolated port of the directional coupler. The phase shift $\Delta\varphi$ and the insertion loss of the RTPS are computed with:

$$\Delta\varphi = -2\arctan\left(\frac{\Im(Z_{IN})}{Z_0}\right) \tag{5-1}$$

$$|S_{21}|_{dB} = |P_c|_{dB} + |\Gamma|_{dB} \tag{5-2}$$

where $|P_c|_{dB}$ represents the insertion loss of the coupler.

The coupler design theory has been already developed in Chapter 3.

5.2.3. Results of the CS-CPW directional coupler for the RTPS

For the RTPS system working at 47 GHz, a coupler with the following specifications is designed:

- $k = 0.7$ $(C = 3\ dB)$
- $Z_0 = 43\ \Omega$ $(Z_C^{even} = 102\ \Omega, Z_C^{odd} = 18\ \Omega)$
- $\theta = 90°$
- High directivity and good return loss

The CPWs are placed in metal M8 to M7 and the floating ribbons are placed in metal M5 in the B55 nm technology from ST Microelectronics, leading to $h = 2.1\ \mu m$. This configuration allows obtaining a good tradeoff between insertion loss and compactness.

After setting $SS = SL$ =0.5µm, W =20 µm, W_g =12 µm, S =5 µm; G =50 µm, with all the ribbons cut on sides, the even- and odd-modes analysis of the CS-CPW structure was carried out in HFSS. The layout of the CS-CPW coupler implemented in the RTPS is given in Figure 5-7 (a) while simulation results are given in Figure 5-7 (b).

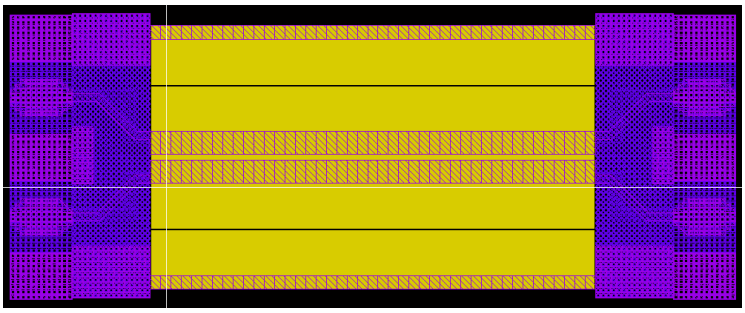

(a)

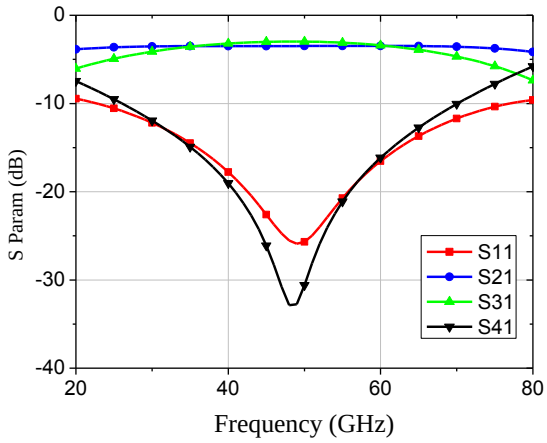

(b)

Figure 5-7: (a) Layout and (b) S-parameters of the CS-CPW directional coupler for RTPS application.

The simulations results at 47 GHz show that the coupler achieves the targeted 3 dB coupling with insertion loss of 0.2 dB on its transmission path and 0.5 dB on its coupled path. For the frequency band between 40 GHz and 60 GHz, the return loss is better than 17 dB. Also it has a high directivity, greater to 14 dB in the entire bandwidth. At the center frequency of 47 GHz, the coupler reaches a high directivity of 30 dB, as expected. This coupler is used in the next section for the design of the RTPS.

5.2.4. Results of the RTPS using the 3-dB CS-CPW directional coupler

Simulations were realized for the RTPS implemented at 47 GHz. The simulation results include the effect of the CS-CPW directional coupler previously showed in section 5.2.3. The voltage V_{tune} over the varactor is varied from 0 V to 2.5 V. The results in Figure 5-8 are for several values of V_{tune}.

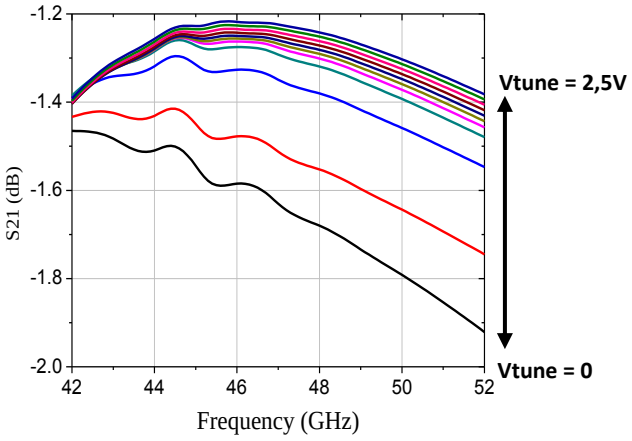

(a)

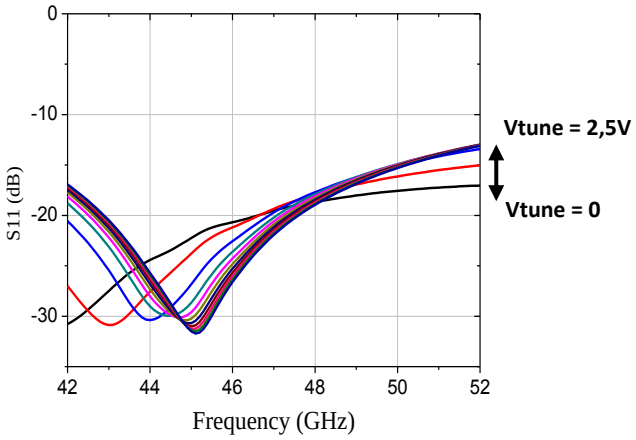

(b)

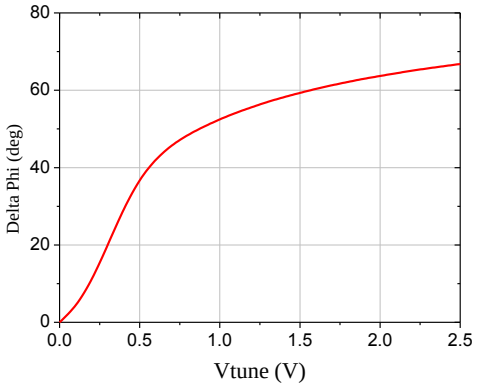

(c)

Figure 5-8: Simulation results of the designed RTPS with a CS-CPW directional coupler for different values of V_{tune}. (a) S_{21}. (b) S_{11}. (c) Relative phase shift at 47 GHz.

In the extreme case ($V_{tune} = 0V$), insertion loss reaches 1.9 dB with a return loss of 13 dB, Figure 5-8 (a) and (b) respectively. The corresponding relative phase shift (in Figure 5-8 (c)) for this condition is around 67°. This case also corresponds to the extreme case in terms of insertion loss variation (around 0.5 dB). Therefore the figure of merit reaches 41°/dB. At 47 GHz, the minimum insertion loss is 1.2 dB and maximum insertion loss is 1.6 dB, leading to a variation of 0.4 dB.

To conclude this section, promising performance is achieved for the RTPS implemented with CS-CPWs.

In the next section, the second application of the CS-CPW directional coupler is presented.

5.3. Isolator

The second application of the CS-CPW directional coupler presented herein is an isolator. The latter has been studied by the MSc student Vishaka Dang during her master thesis in 2015 [14].

An isolator is a two-port network allowing to transmit signal in one direction only whilst isolating the return signal, as shown in Figure 5-9.

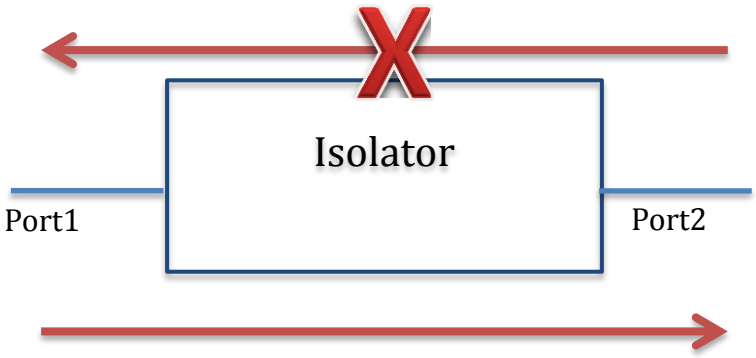

Figure 5-9: Principle of an isolator.

The scattering matrix for an ideal isolator has the following form:

$$[S] = \begin{bmatrix} 0 & 1 \\ 0 & 0 \end{bmatrix} \tag{5-3}$$

[S] matrix (5-3) shows that both ports are matched, and that transmission occurs only in the direction from port 2 to port 1. Since the scattering matrix is not unitary, the isolator must be lossy. An isolator is a non–reciprocal component; therefore the [S] matrix is not symmetric.

Magnetic ferrites is the most popular material for making passive isolators in microwave systems since the isolator with ferrite has the merits of high power handling, no DC power consumption, and high isolation [15]. However, due to the physical nature of ferrite, these isolators require a magnetic bias, usually provided by a permanent magnet. The size and weight of this magnet represents great difficulties in terms of miniaturization and integration. Active isolators, on the other hand, can be integrated with other RF/microwave circuits to realize a system–on–chip solution without sacrificing performance [16]-[17]. Important figures-of-merit for active isolators include insertion loss, isolation and return loss. Generally speaking, these three figures-of-merit are a direct trade off with bandwidth: the more bandwidth is desired, the more degraded set of specs will be attained.

5.3.1. State-of-the-art for mm-wave isolators

This part reviews the major designs of active and passive isolators used at mm-wave. At the end, a table comparing the performance of the phase shifters is presented.

A configuration of isolator was proposed in [15]. It consists of a directional coupler and a non–reciprocal phase shifter in feedback, as shown in Figure 5-10.

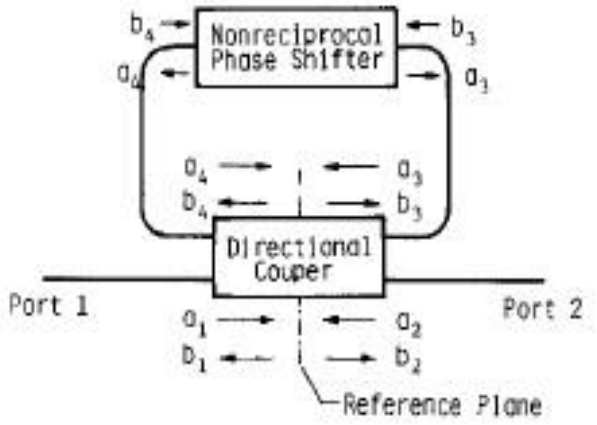

Figure 5-10: Schematic of an isolator based on a non-reciprocal travelling-wave resonator.

The configuration in Figure 5-10 results in a low insertion loss of 1 dB, a high isolation of 18 dB and a narrow bandwidth at a frequency of 50.61 GHz. However, the use of magnetized ferrite pillbox to realize the non-reciprocal travelling wave resonator limits its integration capability with advanced CMOS technologies.

In [16] an active isolator was designed using a parallel combination of common-gate (CG) and common-drain (CD) transistor configurations as shown in Figure 5-11.

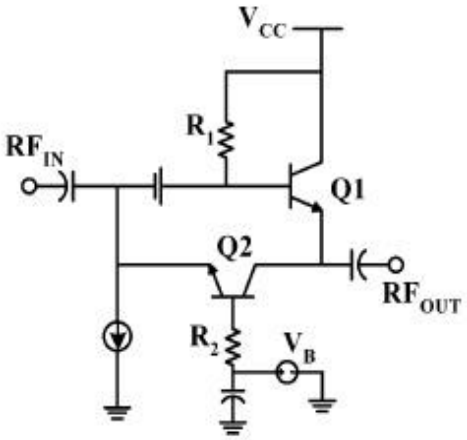

Figure 5-11: Isolator designed using parallel CG and CD transistor configuration for 5-6 GHz.

The isolator in Figure 5-11 presents insertion loss of 2 dB and high isolation greater than 30 dB in the 5-6 GHz frequency band. Nevertheless, high insertion loss at low frequency limits the use of this circuit for higher frequencies.

In [17] was described the creation of movement of magnetic field using a microstrip line and two rows of periodic resonators on both sides of the microstrip line. These are placed on a dielectric substrate as shown in Figure 5-12.

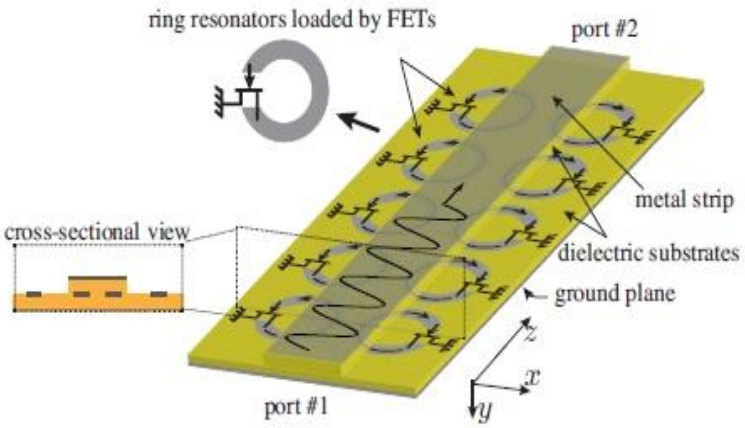

Figure 5-12: Isolator at 3 GHz designed using metamaterials.

This configuration leads to insertion loss of 7.5 dB and isolation greater than 30 dB at 3 GHz. The disadvantage of this structure is clearly the high insertion loss.

A GaAs MMIC active isolator was presented in [18]. It was designed using low-noise amplifier and a Tee attenuator. The center frequency is 1.4 GHz and the bandwidth is 200 MHz. The configuration shown in Figure 5-13 lessens the output of a low-noise amplifier with a 50 Ω Tee attenuator.

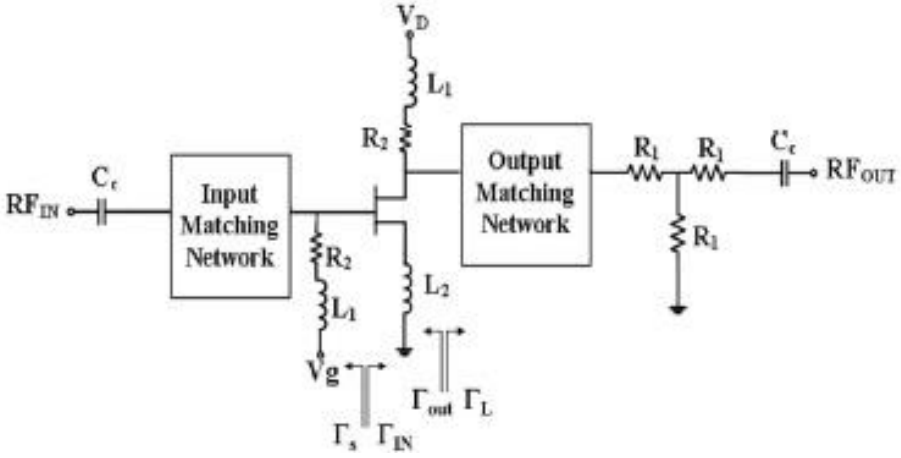

Figure 5-13: Schematic of the MMIC active isolator.

The configuration in Figure 5-13 has 2.5 dB of insertion loss, input and output return loss better than 12 dB, and finally a reverse isolation of 31 dB. The limitation of the topology is linked to non linearities that would appear since the signal is flowing through the transistor.

In our opinion, the best tradeoff between insertion loss, return loss, isolation and non linearities was presented in [19]. The isolator uses TSMC 0.18µm CMOS technology and was designed at 24 GHz. The proposed topology uses a directional coupler and a non-reciprocal amplifier in feedback, as shown in Figure 5-14.

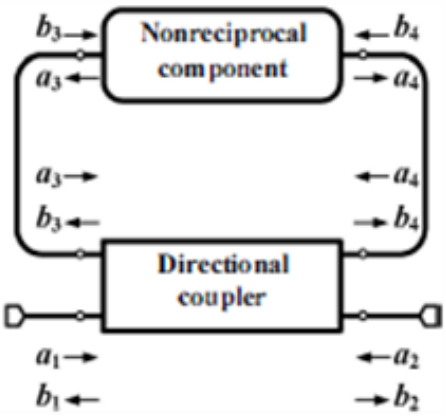

Figure 5-14: Block diagram of the proposed isolator [19].

This isolator achieved 36 dB of isolation with 1.8 dB of insertion loss. The DC power consumption is only 3.6 mW. This configuration gives attractive results at a high frequency. This configuration is used in this section to design an active isolator at 77 GHz. Table 5-2 summarizes in detail the state-of-the-art for the isolators presented above.

TABLE 5-2 STATE-OF-THE-ART OF MICROWAVE ISOLATORS

Ref	Freq. (GHz)	Topology	IL (dB)	Isolation (dB)	Return Loss (dB)	P_{DC} (mW)	Area (mm^2)
[15]	50.61	Non-reciprocal travelling wave ferrite resonator	1	18	N/A	0	N/A
[16]	5-6	SiGe HBT Active isolator	2	>30	>12	5.4	0.28
[17]	3	Metamaterials	7.5	>30	>13	112	0.36
[18][17]	1.4	MMIC active isolator with attenuator	2.5	31	>12	4.5	0.65
[19]	24	MMIC active isolator with CS amplifier	1.8	36	>17	3.6	0.29

5.3.2. Principle of the isolator with CS-CPW

The block diagram of the proposed isolator is presented in Figure 5-15 (a). Its schematic is shown in Figure 5-15 (b). The isolator is composed of a matched common-source amplifier and a CS-CPW directional coupler. The transmission lines in Figure 5-15 (b) are used for phase adjustment.

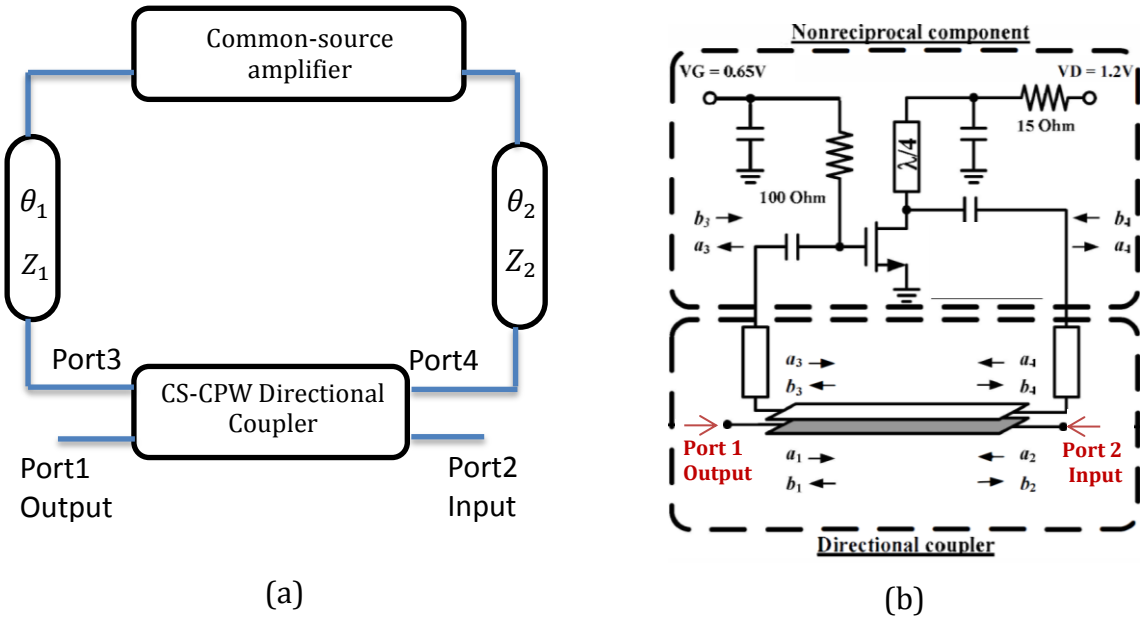

Figure 5-15: (a) Diagram block for the isolator implemented with CS-CPW and (b) electrical circuit for the isolator, inspired from [19].

Figure 5-15 (b) shows the circuit of the isolator designed at 77 GHz by Vishaka Dang and inspired by the 24 GHz active isolator proposed in [19]. Theoretical principle, design and dimensions are fully detailed in [14]. Theoretical principle can be found as well in [19]. Any signal coming from the output port either gets coupled and flows through the feedback loop, or goes directly to the input port. The part of the signal going through the feedback loop gets coupled again from port 4 to port 2. It reaches the input port with a phase difference of 180° with respect to the part of the signal going directly from output port 1 to input port 2. Hence, the two signals cancel each other and results in no signal flow from output port to input port.

Any signal entering at input port either gets coupled from port 2 to port 4 and goes through the feedback loop, or flows directly to the output port. The part of the signal in the feedback loop gets absorbed by the amplifier, thanks to the perfect matching of the amplifier. Therefore the circuit shown in Figure 5-15 allows signal to flow in only one direction.

5.3.3. Results of the CS-CPW directional coupler for the isolator

For the isolator system working at 77 GHz, a coupler with the following specifications was desirable:

- $k = 0.42$ $(ie. C = 7.5$ dB$)$
- $Z_c = 50\Omega$ $(Z_C^{even} = 78\Omega, Z_C^{odd} = 32\Omega)$
- $\theta = 90°$
- High directivity and good return loss

High directivity ensures that no signal reaches the isolated port. Signal at the isolated port would flow through the loop to be coupled back to the input port, which is undesirable.

From the design perspective, it is very difficult to get k_L equal to k_c, both equal to 0.42, along with the desired values of Z_c^{even} and Z_c^{odd}, i.e. $Z_c = 50\Omega$. So a trade-off was adopted between the coupling coefficient and characteristic impedance, in order to meet the specifications. For this reason it was better to choose the CS-CPW as a solution, because it presents flexibility in terms of design, allowing decreasing the complexity of the study.

A CS-CPW structure was designed to be included in the isolator system. The signals and grounds strips are stacked from metal M8 to metal M7 and floating ribbons are placed in Metal M5, leading to $h = 2.1$ µm. After setting $SS = SL$ =500 nm, W =15 µm, Wg =12 µm, S =18 µm, G =20 µm, and a combination of the shielding cut in the center and on the sides *CC-CS*, the even- and odd -modes analysis of the CS-CPW structure was carried out in HFSS. The resulting structure is presented in Figure 5-16 (a). S-parameters of the coupler with the above mentioned dimensions are shown in Figure 5-16 (b).

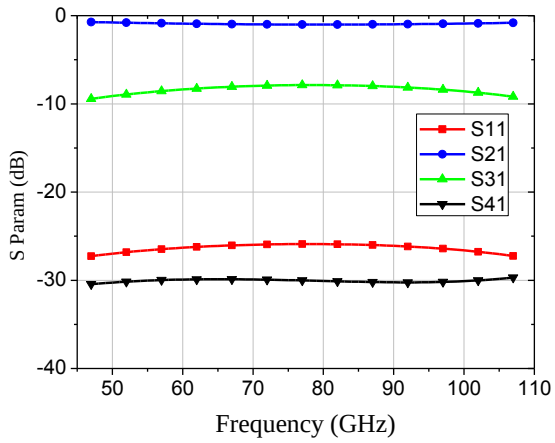

Figure 5-16: S-parameters of CS-CPW directional coupler designed for isolator application.

Figure 5-16 shows -30 dB on the isolated port with good return loss of -26 dB, Θ =90°, k =0.41 (i.e. 7.7 dB) and Z_c =48Ω. In the next section, the behavior of the isolator with the CS-CPW is described.

5.3.4. Results of the isolator using the 7.5-dB, CS-CPW directional coupler

The S-parameter results of the final isolator circuit are shown in Figure 5-17.

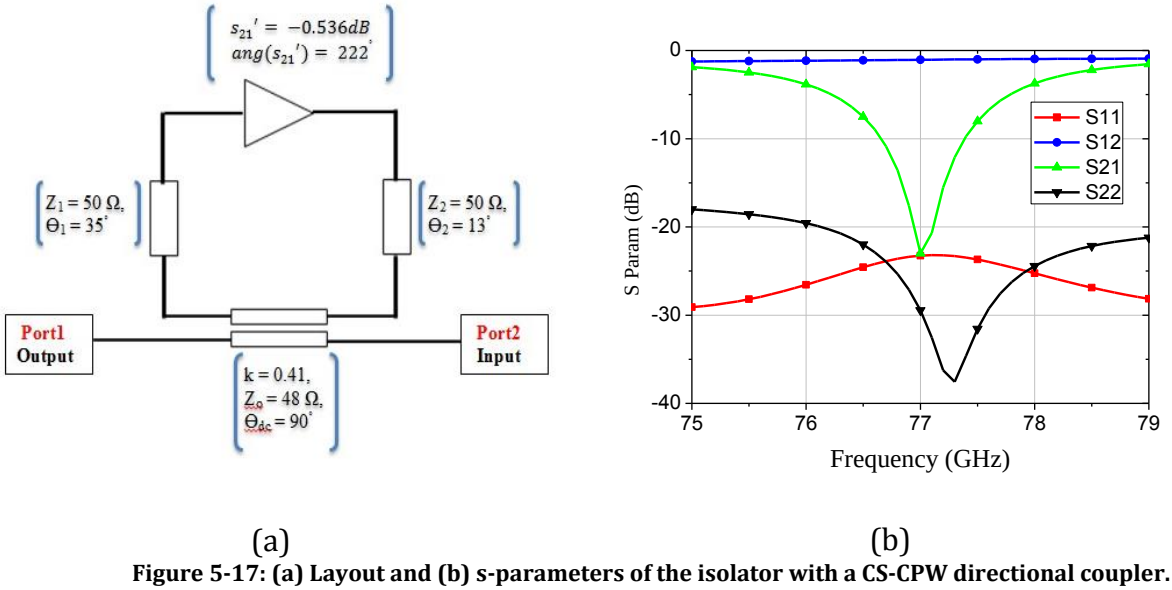

(a) (b)

Figure 5-17: (a) Layout and (b) s-parameters of the isolator with a CS-CPW directional coupler.

The isolator circuit designed at 77 GHz using a BiCMOS 55 nm technology achieves 1 dB of insertion loss, 23 dB of isolation and a return loss better than 20 dB on both ports in a 2 GHz band. Design analysis and results show that the isolator is very sensitive to gain/loss of the amplifier and electrical length of the transmission lines.

5.4. Baluns

The third application of the CS-CPW directional couplers developed in the laboratory is a balun. The study was performed by the PhD student Ayssar Serhan [20]. A balun is a three-port network allowing the transition between a common-mode signal into a differential-mode signal. Figure 5-18 illustrates the block diagram of a balun.

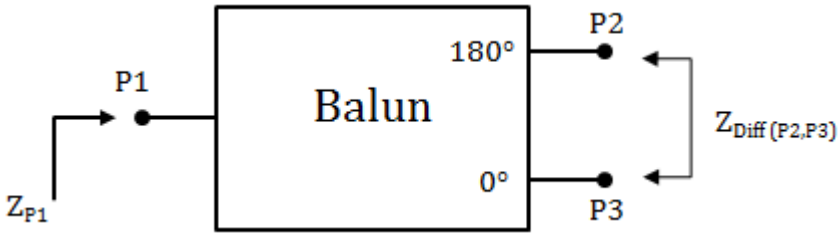

Figure 5-18: Block diagram of a balun.

As shown in Figure 5-18, the balun must transform a single signal into two with the same amplitude and an out-of-phase difference of 180°. Since the balun is a passive reversible device, it could also transform a differential signal into a single one.

5.4.1. State-of-the-art for mm-wave baluns

A Marchand balun was presented in [23]. As shown in Figure 5-19 (a) and (b), a floating bar was placed under the coupled strips in order to have an extra parameter to control the coupling.

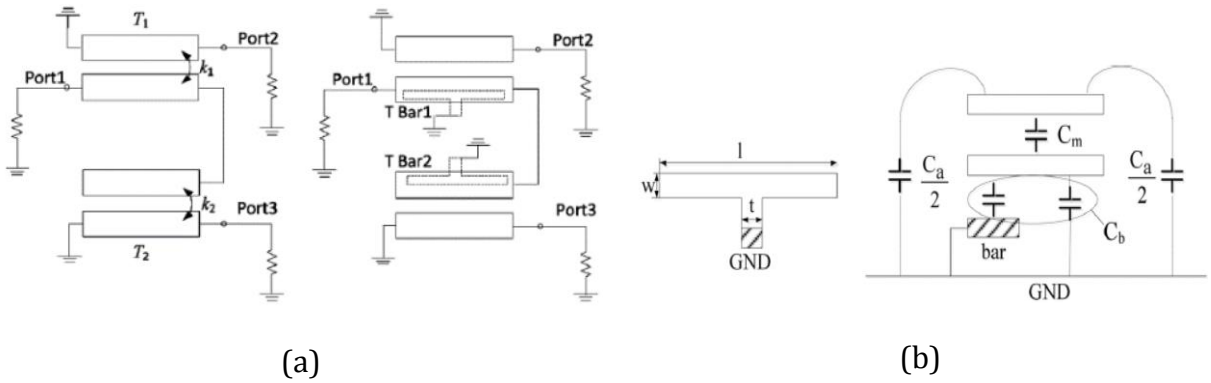

(a) (b)

Figure 5-19: (a) Schematic of the modified Marchand Balun and (b) Lateral view of the strips coupled with the floating bar.

The coupled lines in Figure 5-19 (a) and (b) present a broadside coupling, which increase the coupling and also reduces the balun footprint. The bandwidth of this circuit is 57-67 GHz. It presents a phase error of 1° and an amplitude error of 0.5 dB. Insertion loss in is 1.5 dB and it has 18 dB of return loss.

An optimization technique called CLC (Capacitive Loading Compensation) was presented in [24]. As expected from the name: capacitances are added to the entry and to the output ports as illustrated in Figure 5-20.

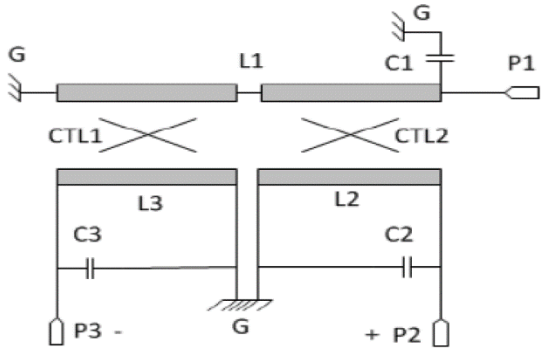

Figure 5-20: Schematic of the balun with the capacitive compensation [24].

The capacitances are used to improve the matching of the ports, as well as to reduce the length of the transmission lines. The balun exhibits a bandwidth between 40 GHz and 60 GHz. It presents an amplitude error of 0.2 dB and a phase error of 2.7°.

An alternative optimization technique was showed in [25]. This technique allows to compensate the phase error and amplitude error through the compensation of the phase velocity of each mode. This was achieved thanks to the introduction of a transmission line between the coupled lines. Also, the coupled lines in this case were folded (or spiral) thus less space was used to implement the balun (Figure 5-21).

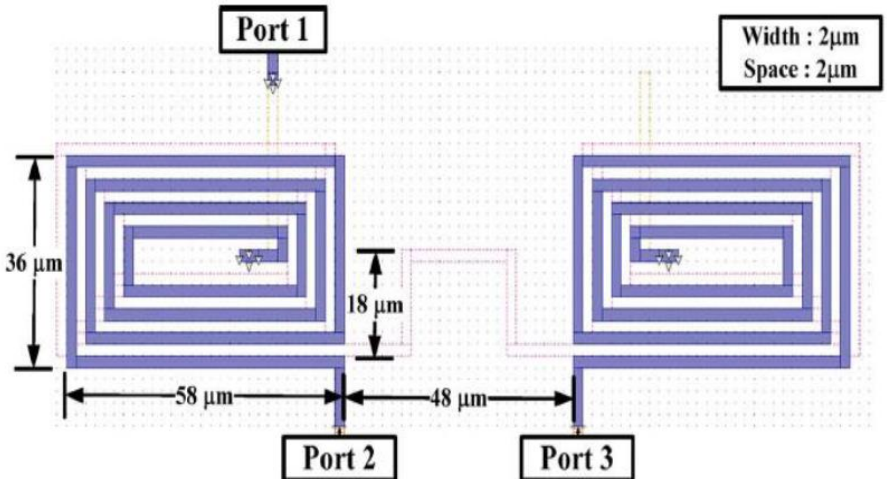

Figure 5-21: Layout of the spiral balun [25].

The circuit presents a bandwidth from 40 GHz to 80 GHz. The compensation technique presented in [25] was also used in the design of the CS-CPW-based balun.

Another solution for a balun was proposed in [26]. The technology used in this circuit allows the implementation of a full ground plane over the substrate. This principle shown in Figure 5-22 (a) and the corresponding layout in Figure 5-22 (b).

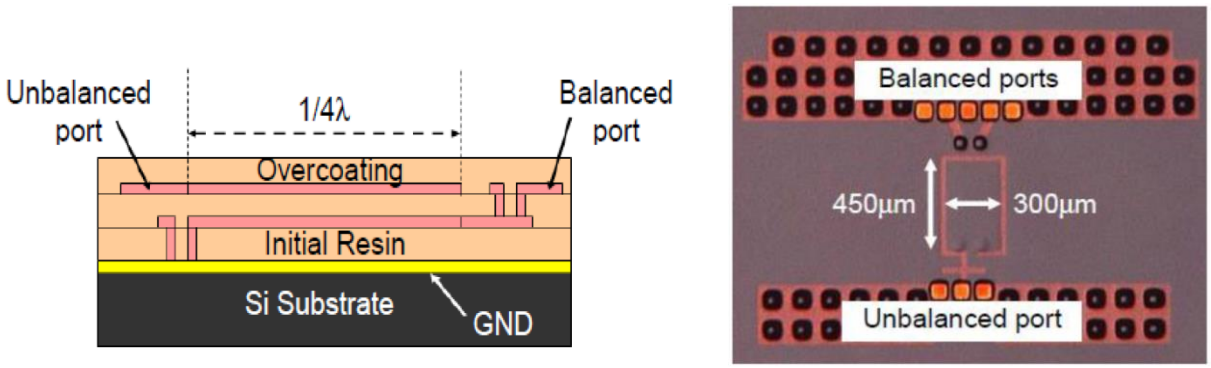

(a) (b)

Figure 5-22: (a) Schematic and (b) layout of the balun in SIP technology [26] .

The ground plane prevents from any loss due to the substrate. This circuit needs nevertheless, a certain ratio of even- and odd-mode characteristic impedances that are not possible to reach with CMOS technologies.

A brief summary of the performance of each reference previously introduced is done in Table 5-3.

TABLE 5-3 STATE-OF-THE-ART OF BALUN IN MM-WAVE

Ref	Area (mm^2)	Freq. (GHz)	IL (dB)	Phase and amplitude error $\Delta_{\alpha_{max}}/\Delta_{\varphi_{max}}$
[23]	0.01	57-67	1.5	<0.5 dB/1°
[24]	0.036	40-60	1.9	<0.2 dB/2.7°
[25]	0.2397	40-80	2	-
[26]	0.135	57-66	0.6	<0.35 dB/8°

5.4.2. Principle of the balun with CS-CPW

The balun developed during Ayssar's thesis is a Marchand balun type [21]. This kind of balun is composed of coupled lines, which are CS-CPWs in our design. The schematic of the Marchand balun is shown in Figure 5-23.

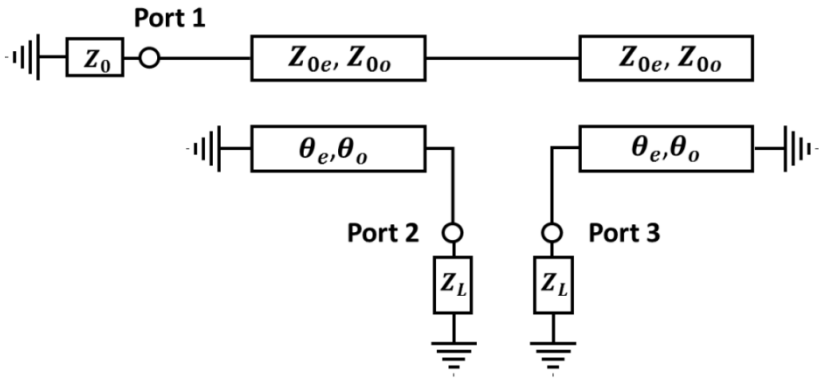

Figure 5-23: Conventional Marchand balun.

For the ideal case, the coupled lines in the Marchand balun must have the same phase velocity for both even- and odd-modes ($\theta_e = \theta_o = 90°$). The S-parameters of the Marchand balun when loaded by Z_0 on port 1 and by Z_l on ports 2 and 3, were developed in [22]:

$$[\mathrm{S}]_{\mathrm{balun}} = \begin{bmatrix} \dfrac{1-k^2\left(\frac{2Z_l}{Z_0}+1\right)}{1+k^2\left(\frac{2Z_l}{Z_0}-1\right)} & j\dfrac{2k\sqrt{1-k}\sqrt{\frac{Z_l}{Z_0}}}{1+k^2\left(\frac{2Z_l}{Z_0}-1\right)} & -j\dfrac{2k\sqrt{1-k^2}\sqrt{\frac{Z_l}{Z_0}}}{1+k^2\left(\frac{2Z_l}{Z_0}-1\right)} \\ j\dfrac{2k\sqrt{1-k^2}\sqrt{\frac{Z_l}{Z_0}}}{1+k^2\left(\frac{2Z_l}{Z_0}-1\right)} & \dfrac{1-k^2}{1+k^2\left(\frac{2Z_l}{Z_0}-1\right)} & \dfrac{2k^2\sqrt{\frac{Z_l}{Z_0}}}{1+k^2\left(\frac{2Z_l}{Z_0}-1\right)} \\ -j\dfrac{2k\sqrt{1-k^2}\sqrt{\frac{Z_l}{Z_0}}}{1+k^2\left(\frac{2Z_l}{Z_0}-1\right)} & \dfrac{2k^2\sqrt{\frac{Z_l}{Z_0}}}{1+k^2\left(\frac{2Z_l}{Z_0}-1\right)} & \dfrac{1-k^2}{1+k^2\left(\frac{2Z_l}{Z_0}-1\right)} \end{bmatrix} \quad (5\text{-}4)$$

where k is the total coupling coefficient resulting from $k = \sqrt{k_L k_C}$ which only makes sense when $k_L = k_C$.

In order to equally divide input power while maintaining a phase shift of 180° between ports 2 and 3, the initial condition applied to $[S]_{balun}$ is:

$$|S_{21}| = |-S_{31}| = \frac{1}{\sqrt{2}} \quad (5\text{-}5)$$

This condition allows to obtain the coupling coefficient k as a function of the ratio Z_l/Z_0. This ratio is known as the impedance transformation ratio (ITR) of the balun.

$$k = \frac{1}{\sqrt{\frac{2Z_l}{Z_0}+1}} \quad (5\text{-}6)$$

Finally the targeted even- and odd-modes characteristic impedances of the coupled lines can be calculated from the equations:

$$Z^{odd} = Z_0\sqrt{\frac{1-k}{1+k}} \quad (5\text{-}7)$$

$$Z^{even} = Z_0\sqrt{\frac{1+k}{1-k}} \quad (5\text{-}8)$$

Equations (5-7) and (5-8) are correct as long as even- and odd-modes have the same the phase velocity (which is equivalent of having $k_L = k_C = k$ as seen in Chapter 2). With these design rules, a balun centered at 80 GHz was implemented. In the next section, the performance of the CS-CPW directional coupler used in this balun are shown.

5.4.3. Results of the CS-CPW directional coupler for the balun

The signal and ground strips were stacked from metal M8 to metal M7 and floating ribbons were placed in Metal M5, leading to $h = 2.1$ µm. $SS = 0.64$ µm, $SL = 0.16$ µm, $W_g = 12$ µm, $S = 5$ µm, $G = 25$ µm, $W = 25$ µm with all fingers cut on the side CS. These parameters are chosen in order to present a 3-dB coupler. Figure 5-24 (a) and (b) show the resulting layout of the balun and the S-parameters of the coupler to be used in the balun, respectively.

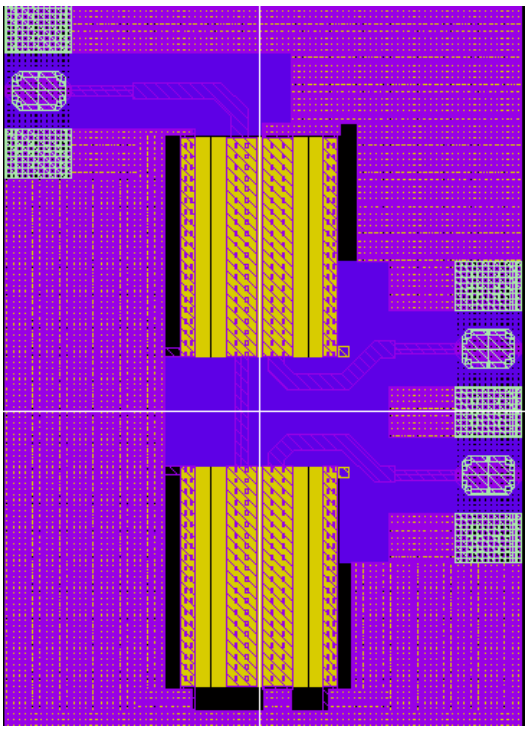

(a)

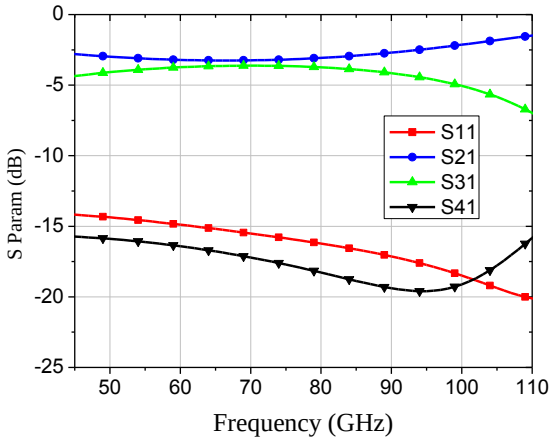

(b)

Figure 5-24: (a) Layout of the balun and (b) S-parameters of the CS-CPW directional coupler.

The simulation results of the coupler based on CS-CPW presented in Figure 5-24 show a directivity of 15 dB at the center frequency.As it is desired, 3-dB coupling is obtained. Good return loss is also reached.

5.4.4. Results of the balun using the 80 GHz, 3-dB, 50 Ω, CS-CPW directional coupler

Thanks to the theory presented in previous sections, a Marchand balun was integrated at 80 GHz. The central frequency was chosen in order to work in E-band. The simulation results of the balun are shown in Figure 5-25.

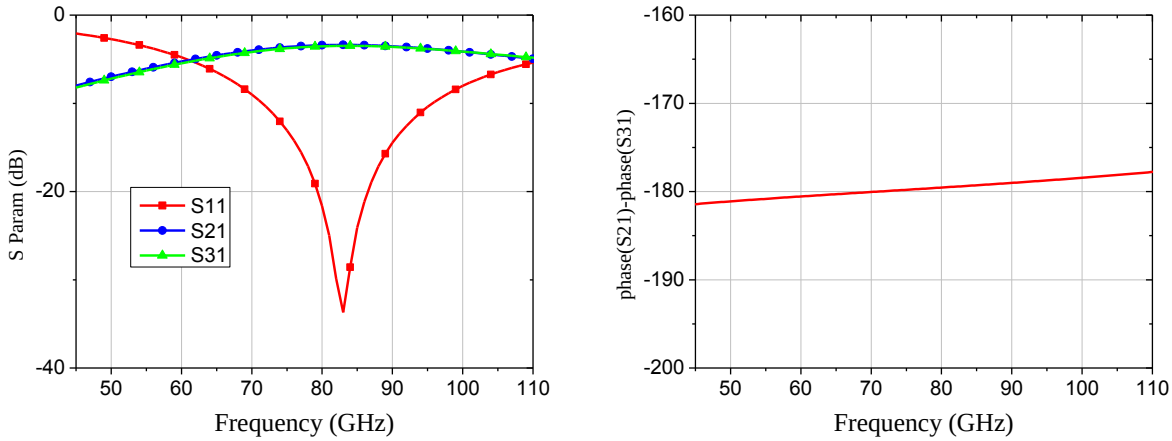

Figure 5-25: (a) S Parameters of the balun with CS-CPW and (b) phase difference between port 2 and port 3.

As expected the balun is well matched around its central frequency (83 GHz) with a parameter S_{11} of -33 dB (Figure 5-25 (a)). Also at ports 2 and 3, output signals have almost the same magnitude (Figure 5-25 (a)). Besides, the difference in phase between ports 2 and 3 is as desired 180° (Figure 5-25 (b)). The overall surface is 0.13 mm^2.

The simulation results show that baluns based on CS-CPWs are an interesting solution for high frequency baluns.

5.5.Conclusion

In Chapter 2, the basis for CS-CPW has been presented. Besides, in Chapter 3, the method to design a directional coupler with CS-CPW has been described. In this chapter we have discussed about the applications of such CS-CPW directional couplers.

Three applications that are being currently developed in our laboratory were developed. In first place a Reflection-Type Phase Shifter (RTPS) was presented with a 47-GHz working frequency. It was implemented with a CS-CPW coupler instead of a hybrid one. The RTPS presents insertion loss less than 1.9 GHz and a FoM of 41°/dB. Next, an isolator composed of a common-source amplifier and a CS-CPW coupler was designed. This isolator is centered at 77 GHz, it exhibits 1 dB of insertion loss and 23 dB of isolation. Finally a Marchan balun with CS-CPW coupler was described at 80 GHz, it presents a return loss of 33 dB and minimum phase and amplitude error.

All these applications present encouraging results, proving the interest of CS-CPW structures. Besides, each application is centered at a different frequency, proving the interest of CS-CPW lines at various frequencies. The three circuits have been already sent to fabrication in a BiCMOS 55 nm technology by ST Microelectronics.

5.6.References

[1] R. H. Hardin, E. J. Downey, and J. Munushian, “Electronically-variable phase shifters utilizing variable capacitance diodes,” in *Inst. Radio Eng. (IRE)*, vol. 48, no. 5, pp. 944-945, May 1960.

[2] F. Burdin, “Nouvelles topologies de diviseurs de puissance, baluns et déphaseurs en bandes RF et millimétriques, apport des lignes à ondes lentes,” Ph.D. dissertation, Université de Grenoble-Alpes, 16 July, 2013.

[3] Z. Iskandar, “Conception d’un RTPS en technologie BiCMOS 55nm. Application à l’orientation de faisceau en bande millimétrique,” in *Journée Nationales Microondes (JNM)*, Bordeaux, 2015.

[4] F. Burdin, Z. Iskandar, F. Podevin, P. Ferrari, "Design of Compact Reflection-Type Phase Shifters With High Figure-of-Merit," *IEEE Trans. Microw. Theory Techn*., vol. 63, no. 6, pp. 1883-1893, Jun. 2015.

[5] Miyaguchi, K.; Hieda, M.; Nakahara, K.; Kurusu, H.; Nii, M.; Kasahara, M.; Takagi, Tadashi; Urasaki, S., "An ultra-broad-band reflection-type phase shifter MMIC with series and parallel LC circuits," *IEEE Trans. Microw. Theory Techn*., vol. 49, no. 12, pp. 2446-2452, Dec. 2001.

[6] A. Natarajan, A. Komijani, X. Guan, A. Babakhani, and A. Hajimiri, “A 77-GHz phased-array transceiver with on-chip antennas in silicon: Transmitter and local LO-path phase shifting,” *IEEE J. Solid-State Circuits,* vol. 41, no. 12, pp. 2807-2819, Dec. 2006.

[7] K.-J. Koh and G.M. Rebeiz, “0.13-µm CMOS phase shifters for X-, Ku- and K-band phased arrays,” *IEEE J. Solid-State Circuits*, vol. 42, no. 11, pp. 2535-2546, Nov. 2007.

[8] J. Lugo-Alvarez, A. Bautista, F. Podevin, P. Ferrari, "High-directivity compact slow-wave CoPlanar waveguide couplers for millimeter-wave applications," in *European Microw. Conf.,* Rome, Italy 2014.

[9] M. Tsai and A. Natarajan, “60 GHz passive and active RF-path phase shifters in silicon,” in *Radio Freq. Integr. Circuits Symp.*, Jun. 2009.

[10] S. Gong, H. Shen, and N. S. Barker, “A 60-GHz 2-bit Switched-Line Phase Shifter Using SP4T RF-MEMS Switches,” *IEEE Trans. Microw. Theory Techn*., vol. 59, no. 4, pp. 894-900, Apr. 2011.

[11] Y.-C. Chiang, W.-T. Li, J.-H. Tsai, T.-W. Huang, "A 60GHz Digitally Controlled 4-bit Phase Shifter with 6-ps Group Delay Deviation," ," in *Int. Microw. Symp. Dig.*, pp. 1-3, Jun. 2012.

[12] H.-T. Kim, J.-H. Park, S. Lee, S. Kim, J.-M. Kim, Y.-K. Kim, and Y. Kwon, "V –Band 2-b and 4-b Low-Loss and Low-Voltage Distributed MEMS Digital Phase Shifter Using Metal–Air–Metal Capacitors," *IEEE Trans. Microw. Theory Techn*., vol. 50, no. 12, pp. 2918-2923, Dec. 2002.

[13] Y. Yu, P. Baltus, A. van Roermund, D. Jeurissen, A. de Graauw, E. van der Heijden, R. Pijper, "A 60 GHz digitally controlled phase shifter in CMOS," in *European Solid-State Circuits Conf.*, 2008.

[14] V. Dang, "Active isolator at 77-GHz," M.S. thesis in NENT, Université de Grenoble-Alpes, 2015.

[15] M.Muraguchi, *et al.*, "A new type of isolator for millimeter-wave integrated circuits using a non-reciprocal traveling wave resonator", *IEEE Trans. Microw. Theory Techn*., vol. 30, no. 11, pp. 1867-1873, Nov.1982.

[16] J. Lee, *et al.*, "A 5-6 GHz SiGe HBT monolithic active isolator for improving reverse isolation in wireless systems," *IEEE Microw. Compon. Lett.*, vol. 15, no. 4, pp. 220-222, Apr. 2005.

[17] T.Kodera, *et al.*, "Isolator utilizing artificial magnetic gyrotropy," in *Int. Microw. Symp. Dig.*, Jun. 2012.

[18] Cordoba, *et al.*, "A 1.4-GHz MMIC Active Isolator for Integrated Wireless Systems Applications", in *Wireless and Microw. Technol. Conf.*, Tampa, USA, Jun. 2014.

[19] Jen-Feng Chang, *et al.*, "A 24-GHz fully integrated isolator with high isolation in standard RF 180-nm CMOS technology", in *Int. Microw. Symp.,* Tampa, USA, Jun. 2014.

[20] A. Serhan, "Conception et réalisation de fonctiones millimétriques en technologie BiCMOS 55 nm," Ph.D. dissertation, Université de Grenoble-Alpes, 28 Sept., 2015.

[21] N. Marchand, "Transmission-Line Conversion Transformers, " Electronics, vol.17, pp. 142-146, Dec. 1994.

[22] J.S. Kim, "Broadband balun and phase noise measurement system design for RFIC testing", Ph.D. dissertation, University of Florida, 2009.

[23] L. Xu, *et al.*, "A Miniaturized Marchand Balun in CMOS With Improved Balance for Millimeter-Wave Applications," *IEEE Microw. Compon. Lett.*, vol. 24, no. 1, pp. 53-55, Jan. 2014.

[24] K. Ma, N. Yan, K.S. Yeo, W.M. Lim, "Miniaturized 40–60 GHz on-Chip Balun with Capacitive Loading Compensation", *IEEE Electron Device Lett.*, vol. 35, no. 4, pp. 434-436, Apr. 2014.

[25] P.H. Tsai, Y.H. Lin, J.L. Kuo, Z.M. Tsai, H. Wang, "Broadband Balanced Frequency Doublers with Fundamental Rejection Enhancement Using a Novel Compensated Marchand Balun", *IEEE Trans. Microw. Theory Techn*., vol. 61, no. 5, pp. 1913-1923, May 2013.

[26] Y. Uemichi, et al., "Low-loss and compact millimeter-wave balun on Si", in *Int. Microw. Symp.,* Baltimore, USA, 2011.

General Conclusions

The work in this thesis concerned the development of Coupled-Slow-wave CoPlanar Waveguide (CS-CPW) on CMOS advanced technology for mm-wave frequencies. Compared to traditional CPW or microstrip lines, this structure exhibits a high quality factor, miniaturization characteristic and the most important: a flexible choice in the coupling level. Thanks to the slow-wave effect the electric field is being dissociated from magnetic field, leaving to two main advantages: (i) increase of the capacitance, leading to miniaturized circuits, and (ii) extra degree of freedom thus electric and magnetic coupling coefficients can be determined independently. Based on this novel structure, integrated mm-wave passive devices were then designed: directional couplers, filters, baluns, RTPS phase shifter, and isolator.

First, in chapter 2, an electrical model based on even- and odd-modes was proposed for the coupled S-CPWs. The latter was validated through 3D EM simulations and an analytical model developed in the laboratory. In addition, an extraction method of the electrical parameters from EM simulations was introduced. Based on this extraction, the evolution of the main parameters of the CS-CPWs was plotted as a function of the dimensions. Next, a comparison with microstrip lines' solution was carried out. After that the concept of modifying the electric coupling coefficient by cutting the shielding was presented. A study of the coupling variation, versus the dimensions and the cuts of the shielding, was achieved. Practical issues as the effect of dummies or the dimensions limitations for CS-CPWs were also discussed.

Next, in chapter 2, a design method to implement CS-CPW-based directional couplers was fully detailed. Thanks to the extra degree of freedom in the design due to the slow-wave effect, any desired coupling can be achieved while always keeping a high directivity. This is how two directional couplers were designed with CS-CPWs, i.e. a 3-dB (at 50 GHz) and an 18-dB (at 150 GHz), respectively. Experimental results carried out on the 18-dB coupler presented a coupling coefficient of 18 dB, 20 dB return loss and 12 dB of directivity. Hence the agreement between simulation and measurement results was very good, with overall state-of-the-art performances for a first prototype at 150 GHz.

It is worth to mention that because of the VNA limitations, an alternative method was proposed in order to measure a 4-port device at 150 GHz. Instead of a 4-ports measurement, three 2-ports measurements were carried out; at every time the remaining ports not connected to the VNA were loaded by an active load developed by ST Microelectronics for this purpose.

Moreover, a multimode TRL method was implemented in order to de-embed the measurement of the directional coupler when doing a full 4-port measurement.

Then, in chapter 4, the CS-CPWs were used to implement pass band filters. The classical theory of parallel coupled-line filter was briefly presented. Filters theory is based on the characteristic impedance of even- and odd-modes of the coupled-lines; for this reason, previously discussed analytical model charts were used in order to have a starting point for the design. After optimization with circuits' tools, two filters were realized with a working frequency equal to 80 GHz. The first one is a resonator presenting 22% of relative bandwidth and 1.3 dB of insertion loss. The second one is a third-order filter with 11% of relative bandwidth and 4.1 dB of insertion loss, leading to an unloaded quality factor equal to 24.6.

Finally, in chapter 5, several prospects were drawn. Directional couplers being a fundamental element in numerous systems in the mm-wave field, the interesting outputs of this work, i.e. the development of miniaturized coupled-lines with equal electric and magnetic coupling coefficients, leaded to the development of new circuits. These circuits are part of two theses and an internship works. They are being currently developed by two laboratories (IMEP-LAHC and IEMN) and one company (ST Microelectronics). The first circuit is a new topology of reflection-type phase shifter (RTPS). The RTPS presents insertion loss less than 1.9 dB and a FoM of 41°/dB. The second circuit is an isolator composed of a common-source amplifier and a CS-CPW coupler. This isolator is centered at 77 GHz, it exhibits 1 dB of insertion loss and 23 dB of isolation. Finally a Marchand balun with CS-CPW coupler was designed at 80 GHz, it presents a return loss of 33 dB and minimum phase and amplitude error. All circuits are in the fabrication stage now.

Furthermore, the de-embedding method implemented in this work can be used not only for CS-CPWs measurements but for all kinds of 4-ports devices. Currently, this method is also used in the measurement of SIW-based directional couplers. Finally, the 18-dB coupler at 150 GHz previously discussed was optimized and shifted to 180 GHz. This circuit was sent to fabrication as an essential part of a system addressed to do on-wafer measurements.

Publications

During PhD:

- E. Pistono, A. Bautista, J. Lugo-Alvarez, E. Sharma, Z. Iskandar, F. Podevin, S. Bourdel, P. Ferrari, "Recent advances of CMOS/BiCMOS tunable circuits for mm-wave applications," en technologie BiCMOS 55nm. Application à l'orientation de faisceau en bande millimétrique," in *European Microwave Conference Workshop on Technologies Overview for mm-wave Tunable Circuits*, ***invited paper***, Paris, France, 2015.
- **Lugo-Alvarez, J.**; Bautista, A.; Podevin, F.; Ferrari, P., "Coupleurs directifs et filtres millimétriques utilisant des coupleurs innovants basés sur des lignes à ondes lentes couplées en technologie BiCMOS avancé," in *Journées Nationales des Micro-ondes (JNM)*, Bordeaux, June, 2015. ***Best student paper award***
- Z. Iskandar, F. Bautista, **J. Lugo-Alvarez**, E. Pistono, P. Ferrari, "Conception d'un « Reflection-Type Phase Shifter » en technologie BiCMOS 55nm. Application à l'orientation de faisceau en bande millimétrique," in *Journées Nationales des Micro-ondes (JNM)*, Bordeaux, June, 2015.
- **J. Lugo-Alvarez**, F. Bautista, F. Podevin, P. Ferrari, "High-directivity compact slow-wave CoPlanar waveguide couplers for millimeter-wave applications," in *European Microwave Conference*, Rome, Italy, Oct., 2014.
- **J. Lugo-Alvarez**, B. Blampey, F. Podevin, P. Ferrari, "Guides coplanaires couples à ondes lentes: application au couplage millimétrique," in *Journées Nationales des Micro-ondes (JNM)*, Paris, France, 2013.

Before PhD:

- **J. Lugo-Alvarez**, A. Louzir, C. Person, "Ultra compact electronically switchable beam superdirective antenna," EP Patent, 2013
- **J.M. Lugo**, J. de Almeida Goes, A. Louzir, P. Minard, D. Lo Hine Tong, C. Person, "Design, optimization and characterization of a superdirective antenna array," in *European Conference on Antennas and Propagation*, Gothenburg, Sweden, Apr., 2013.

Résumé

L'objectif de ce travail de thèse était le développement en technologie intégrée standard d'une structure de lignes de transmission couplée, optimisée en termes de pertes, d'encombrement, de facteur de qualité et surtout du choix du niveau de couplage aux fréquences millimétriques. Cette structure a été nommée CS-CPW (Coupled Slow-wave CoPlanar Waveguide). Dans un premier temps, la théorie ainsi que les modèles électriques des CS-CPW ont été présentés. Grâce aux modèles et aux simulations électromagnétiques, des coupleurs directionnels avec plusieurs valeurs de couplage (3 dB, 10 dB, 18 dB) ont été conçus en technologie BiCMOS 55 nm, puis mesurés à l'aide d'un analyseur de réseau. Ils présentent tous une très bonne directivité, toujours supérieure à 15 dB. Un premier prototype de coupleur a été mesuré à 150 GHz. Dans un deuxième temps, des filtres passe bande à base de lignes couplées ont été développés en utilisant des lignes CS-CPW, avec une fréquence de fonctionnement égale à 80 GHz. Les de simulation laissent entrevoir des résultats concurrentiels avec l'état de l'art : 11% de bande passante relative et un facteur de qualité à vide égal à 24.6 . Finalement, trois projets utilisant les lignes couplées développées ont débuté, dans le cadre de deux thèses et un stage au sein du laboratoire : déphaseur de type RTPS à 47 GHz, isolateur à 75 GHz, et balun à 80 GHz.

Mots-clés: Lignes couplées, ondes lentes, coupleurs, filtres, circuits CMOS en bande millimétrique, technologie BiCMOS avancée 55 nm.

Abstract

This work focuses on high-performances CS-CPW (Coupled Slow-wave CoPlanar Waveguide) transmission lines in classical CMOS integrated technologies for the millimiter-wave frequency band. First, the theory as well as the electrical models of the CS-CPW are presented. Thanks to the models and electromagnetic simulations, directional couplers with different coupling levels (3 dB, 10 dB, 18 dB) were designed in BiCMOS 55 nm technology. They have a good directivity, always better than 15 dB. A first prototype of a coupler was measured at 150 GHz presenting good agreement with the simulations. Next, coupled-line base filters were developed at 80 GHz using the CS-CPWs. Simulation present competitive results with the state-of-art: 11% of fractional bandwidth and a unload quality factor of 24.6. Finally, three projects started based on the CS-CPWs. The projects are currently used in two theses and one internship: a RTPS at 47 GHz, an isolator at 75 GHz and a balun at 80 GHz.

Key words: Coupled lines, slow-wave, couplers, filters, CMOS circuits in mm-wave, BiCMOS 55nmm technology.